ISBN 978-82-326-4556-5 (printed ver.)
ISBN 978-82-326-4557-2 (electronic ver.)
ISSN 1503-8181

NTNU
Norwegian University of
Science and Technology

Doctoral theses at NTNU, 2020:102

Eleonóra Parelius Jonášová

Doctoral thesis

NTNU
Norwegian University of Science and Technology
Thesis for the Degree of
Philosophiae Doctor
Faculty of Natural Sciences
Department of Physics

NTNU

Doctoral theses at NTNU, 2020:102

Eleonóra Parelius Jonášová

Doctoral thesis

NTNU
Norwegian University of
Science and Technology

Doctoral theses at NTNU, 2020:102

Eleonóra Parelius Jonášová

Spatiotemporal mapping of cascading processes in oligonucleotide-functionalized responsive hydrogels

Eleonóra Parelius Jonášová

Spatiotemporal mapping of cascading processes in oligonucleotide-functionalized responsive hydrogels

Thesis for the Degree of Philosophiae Doctor

Trondheim, March 2020

Norwegian University of Science and Technology
Faculty of Natural Sciences
Department of Physics

NTNU
Norwegian University of
Science and Technology

NTNU
Norwegian University of Science and Technology

Thesis for the Degree of Philosophiae Doctor

Faculty of Natural Sciences
Department of Physics

ISBN 978-82-326-4556-5 (printed ver.)
ISBN 978-82-326-4557-2 (electronic ver.)
ISSN 1503-8181

Doctoral theses at NTNU, 2020:102

Printed by NTNU Grafisk senter

Abstract

Responsive DNA hydrogels are a group of hydrogels which feature DNA as a structural and/or functional building block. The DNA and its unique properties provide a great degree of control over its higher order structure and interactions. The combination of programmability and control on the molecular level, afforded by DNA, and of the responsiveness and tissue-like properties of hydrogels on the micro- or macrolevel, allows for a multitude of different designs tailored for different purposes within biosensing, drug delivery, tissue engineering, cell culturing and as various nanodevices. A thorough understanding of the behavior and interactions of the DNA included in the hydrogel is crucial for efficient designing of DNA-based responsive hydrogels and their tuning to the needs of each application.

In this thesis, the response of dual-crosslinked hydrogels to single-stranded oligonucleotide targets is explored. The hydrogels of covalently crosslinked polyacrylamide with additional double-stranded oligonucleotide crosslinks, swell as a result of crosslinks being opened by the target oligonucleotide. The crosslink opening is a result of a toehold-mediated strand displacement – a mechanism often employed within the DNA hydrogel field.

The overall swelling of the hemispherical hydrogels attached to an optical fiber is detected using an interferometric setup. The focus of this thesis is on the interconnected processes of target diffusion, binding and crosslink opening which are the basis of the hydrogel response and which profoundly affect one another, influencing the kinetics of the overall response in a non-trivial manner.

To characterize these processes, confocal laser scanning microscopy using fluorescent dyes attached to molecules of interest was employed. A method to extract concentration profiles from the micrographs in the vicinity of the optical fiber was developed, as the glass fiber led to an optical aberration in the micrographs collected from the hydrogels. Hydrogels crosslinked with DNA as well as hydrogels crosslinked with Morpholino oligonucleotides (MOs) were prepared and exposed to DNA and MO targets, respectively. Hydrogels were prepared with different oligonucleotide concentrations, as well as different lengths of the blocking region, while targets were prepared with various toehold lengths. The spatiotemporal concentration profiles of the targets were obtained using CLSM and the developed correcting procedure.

The profiles were then analyzed in order to assess the effect of the varying molecular parameters on the swelling kinetics as well as on other processes involved in the hydrogel response. One of the parameters that was varied was the toehold length. An increase in the toehold length was shown to increase the overall swelling rate, but only moderately compared to what would be expected from the displacement rate constants, due to the stronger binding of the longer toehold leading to slower effective diffusion of the target into the hydrogel and thus swelling occurring in a limited, slowly increasing, region of the hydrogel. Shorter toeholds led to targets easily dissociating from their binding sites and thus penetrating quickly far into the hydrogel volume.

Comparison of MOs and DNA highlighted the effect of partitioning on the response kinetics. MOs had less partitioning related concentration depletion in the hydrogel relative to the immersing solution than DNA. This is due to their neutral backbone, while DNA was being pushed out of the hydrogel due to its negative charge. As a result, the response of MO hydrogels to MO targets was significantly faster than that of DNA hydrogels to DNA targets.

Fitting the measured spatiotemporal concentration profiles to a reaction-diffusion model allowed for estimation of various molecular and hydrogel parameters, notably the target diffusion coefficient and the binding, disso-

ciation and crosslink opening rate constants. In case of DNA, the fitted parameters were close to what would be expected from the known data on DNA diffusion and strand displacement, but in the case of MOs, the obtained parameters suggest that the strand displacement process of MOs has very different kinetics than that of DNA.

In summary, this thesis uses the effect of toehold length and that of the charged/uncharged oligonucleotide backbone to highlight the complexity of interactions leading to the response of DNA-based responsive hydrogels and the underlying reaction-diffusion character of these interactions. The characterization of these processes offers new insight into these systems and can be valuable when designing and tuning oligonucleotide-based responsive hydrogels.

Acknowledgement

The work in this thesis has been carried out from August 2014 to December 2019 at the Biophysics and Medical Technology Group of the Department of Physics, Norwegian University of Science and Technology (NTNU), Trondheim, Norway. I am grateful for the financial support for this work from NTNU and the Research Council of Norway (project number 240299/F20).

I would first want to thank my supervisor, Bjørn Torger Stokke, for giving me the opportunity to work on this fascinating and challenging project and for his guidance, support and wealth of knowledge that he is always willing to share. I would like to extend my thanks to my co-supervisors as well – Victorien Prot, and especially Rita Dias, who was always willing to offer her suggestions, inspiring questions and sympathies whenever I approached her with a scientific problem, even when not within her field.

I cannot forget to thank our engineers, Astrid Bjørkøy, Kristin Grendstad and Gjertrud Maurstad, without whom nothing would ever work. Astrid was the most involved in my project and was crucial to the first stages and to getting everything up and running, but also later, helping me dig deeper and deeper into this interesting topic. I will always be thankful for the enthusiasm with which she would suggest: ”Let’s try. Just for fun.” To Gjertrud I would like to thank for always being such a kind and wise presence in this group. You were more important to my success and well-being than you probably know.

At this point, I would like to express my gratitude to everyone at biophysics for creating such a friendly atmosphere. It was a pleasure working

here alongside you, even if not with you (since my project was a little solitary). Due to the nature of academia, people come and go quite fast, and I was here a bit longer than most, so I have seen many come and go. I would hate to forget to mention someone, so if you know me, if we have ever met in the corridor or talked in the lunchroom, I thank you for being awesome. And I would like to mention Nataša, with whom I actually got to collaborate some, although the result did not make it into this thesis.

I would like to thank my parents: Ďakujem, že ste ma vždy podporovali v tom, čo som sa rozhodla robiť a stáli pri mne. And my sister San for her always radical awesomeness.

And last but not least, I would like to express my eternal gratitude to my husband Thomas and my daughter Liv, without whom I really don't think I would have been able to do this. Thank you, Thomas, for standing by me during this sometimes trying period and for being my best friend and the love of my life. And thank you, Livuš, for giving my life perspective and bringing more and more joy into it.

Eleonora Parelius Jonášová
19.12.2019, Trondheim

And to any PhD student, postdoc or master student who is reading this because you are planning to work with hydrogels attached to optical fibers, I have one advice: Keep your fiber cutter sharp, or else nothing works. And good luck.

List of Papers

The following publications are included in this thesis:

(I): **Bioresponsive DNA-co-polymer hydrogels for fabrication of sensors**
Parelius Jonášová, E. and Stokke, B.T.
Current Opinion in Colloid & Interface Science, 2016, **26**, 1-8.
doi: 10.1013/j.cocis.2016.07.001
EPJ and BTS wrote and proofread the manuscript. EPJ prepared all the figures and tables. Both authors revised the manuscsript and approved the final version.

(II): **Recovering fluorophore concentration profiles from confocal images near lateral refractive index step changes**
Parelius Jonášová, E., Bjørkøy, A., Stokke, B.T.
Journal of Biomedical Optics, 2016, **21**(12), 126014-1 – 126014-6.
doi: 10.1117/IJBO.21.12.126014.
All authors designed the experiments. The experiments were performed by AB (imaging of PSF) and EPJ (the rest). EPJ performed data analysis and wrote the manuscript. All authors contributed to proofreading and revision of the manuscript and approved the final version.

(III): **Toehold length of target ssDNA affects its reaction-diffusion behavior in DNA-responsive DNA-co-acrylamide hydrogels**
Parelius Jonášová, E., Bjørkøy, A., Stokke, B.T.
As resubmitted after revision to *Biomacromolecules* on December 19th, 2019.
All authors designed the experiments. EPJ performed the experiments, the

data analysis and wrote the manuscript. All authors contributed to proofreading and revision of the manuscript.

(IV): **Cascading molecular processes in oligo-morpholino functionalized responsive hydrogels**
Parelius Jonášová, E. and Stokke, B.T.
As submitted to *Polymers* on December 19th, 2019.
EPJ and BTS designed the experiments. EPJ performed the experiments, the data analysis and wrote the manuscript. Both authors contributed to proofreading and revision of the manuscript.

Contents

Nomenclature

A	adenine
Aam	acrylamide
Bis	N,N'-methylenebisacrylamide
C	cytosine
CLSM	Confocal laser scanning microscopy
DNA	Deoxyribonucleic acid
dsDNA	double-stranded DNA
FRET	Förster resonance energy transfer
G	guanine
GNA	glycol nucleic acid
LNA	locked nucleic acid
MO	Morpholino oligomers
ODE	ordinary differential equation
PDE	partial differential equation
PNA	peptide nucleic acid
PSF	point spread function

RNA ribonucleic acid

ssDNA single-stranded deoxyribonucleic acid

T thymine

TNA threose nucleic acid

List of Figures

Chapter 1

Introduction

While most people might not be familiar with the term ”hydrogel”, it is quite likely they have used one at some point. The first hydrogel that was artificially synthesized was produced by Professors Wichterle and Lím[1] from Prague (Czech Republic) in 1950’s and was soon used for fabrication of soft contact lenses. Apart from contact lenses, hydrogels can be found in hygiene products, such as disposable diapers and sanitary napkins, capsules for prolonged watering of crops, medical electrodes for electroencephalography and electrocardiography, medical implants and some wound dressings (for burns especially).[2] These applications take advantage of the unique hydrogel properties. Hydrogels are crosslinked polymeric networks that can absorb very large amounts of water, which makes them similar to biological tissues. They possess properties of both solids and liquids, as they have elasticity and retain their shape, but allow for diffusion of molecules through them.

There is a category of hydrogels that have been gaining more and more interest over the last few decades, namely responsive hydrogels, sometimes referred to as ”smart” hydrogels. These hydrogels adjust their properties to their environment, and coupled with their unique tissue-like mechanical properties, this makes them good candidates for performing various roles both in and outside of the body. Their applications range from sensing,

through targeted drug delivery in cell cultures as well as in organisms, to serving as scaffolds for tissue growth or as nanodevices with complex behaviors.

A large portion of responsive hydrogels employ deoxyribonucleic acid (DNA) in their design. DNA is an important biological molecule, responsible for storing the genetic information of virtually every living organism. When Nadrian Seeman tried using it to create three-dimensional cages for his hard-to-crystallize molecules in 1980, a new era started for DNA - era of DNA nanotechnology.[3] The properties of DNA make it a unique structural and functional building block for many applications. Its structure and interactions are predictable and customizable, which allows for designing complex, multi-step reactions involving not only DNA, but other molecules as well, since DNA can be selected to act as an aptamer, i.e. specifically bind to a molecule of interest.

The inclusion of DNA within a hydrogel leads to a very useful union. DNA provides remarkable control over the structure and interactions on the molecular level, allowing it to detect and respond to changes in its environment (mostly molecular triggers), and the hydrogel serves to translate this change from the molecular level to an output at a larger scale, whether to amplify the signal for purposes of detection or to react to it in some way (release of molecules, change in hydrogel properties, etc.).

1.1 Aim of the thesis

A large number of different DNA hydrogels with a wide range of designs for various applications have been reported, but each necessitates the knowledge of the DNA's behavior within the hydrogel, to tune the response timing, rate and magnitude to the desired function. While DNA is a very well studied molecule, its incorporation inside a hydrogel affects its interactions.

Strand displacement reactions are among the most used mechanisms within the DNA hydrogel field. In this reaction, a free DNA strand displaces another DNA strand as it binds to a third strand that they are both comple-

mentary with. A large number of DNA hydrogel designs feature one or several strand displacement reactions, either involving only DNA or featuring other molecules as well, thanks to the inclusion of aptamer DNA strands.

The aim of the presented thesis was to explore a model DNA-hydrogel system with DNA crosslinks incorporated in a polyacrylamide network which could be opened by a target DNA strand in a toehold-mediated strand displacement process. The focus was on the interplay of the cascading processes of diffusion, binding, strand displacement and local swelling, which lead to the desired output – overall swelling, and which greatly affect each other.

An established method for monitoring the swelling was used, namely interferometric readout, but a method to monitor the interconnected processes needed to be established. Further, the effect of variations in toehold length of the target on the hydrogel response was to be explored. Finally, the use of a nucleic acid analogue – Morpholino oligonucleotides – instead of the DNA, allowed to investigate the effect of charges on the oligonucleotide backbone, or lack thereof, on the hydrogel response.

Chapter 2

Background

2.1 DNA-based responsive hydrogels

2.1.1 DNA as a building block

Structure of DNA

Deoxyribonucleotic acid (DNA) plays an important biological role encoding, storing, replicating and translating the genetic information of virtually every living organism. DNA's form supports its function. It is a polymeric molecule (see Figure 2.1) with a backbone composed of alternating sugar (deoxyribose) and phosphate groups. The deoxyribose carries a nitrogen-containing nucleobase (cytosine C, guanine G, adenine A or thymine T). It is the sequence of bases that encodes the genetic information. The deoxyribose, phosphate and base are covalently bound together and consitute a DNA monomer – a nucleotide. The nucleotides are in turn also covalently linked to create a single-stranded DNA polymer (ssDNA) . The phosphate end of the polymer is referred to as 5' end and the pentose end as 3' end.

DNA nucleobases have the ability to specifically bind with each other through hydrogen bonds, namely thymine to adenine and cytosine to guanine. The bond between C and G consists of 3 hydrogen bonds and is stronger

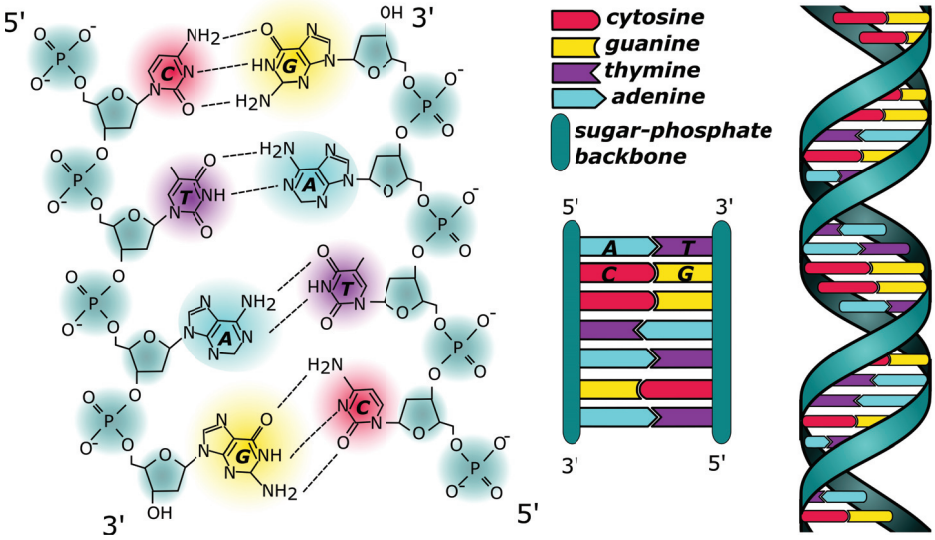

Figure 2.1: Molecular structure of DNA shown at various levels of detail. The backbone is formed by a phosphate-pentose (deoxyribose) polymer that carries the nucleobases attached to the pentose. Two anti-parallel strands can bind with each other and form a double helix if the bases are complementary, i.e. adenine binds to thymine (via two hydrogen bonds) and guanine to cytosine (via three hydrogen bonds).

than that between A and T, which consists of 2 hydrogen bonds. Bases, and subsequently nucleotides, that bind each other are called complementary and it is the complementarity that is the basis of a double helix formation (hybridization). Hybridization occurs between two anti-parallel complementary ssDNA strands, i.e. strands that are side by side, but run in opposite directions (5' to 3' and 3' to 5'). As a result of their complemetarity, the strands associate through hydrogen bonds to create the famous double-stranded DNA helix (dsDNA).

The DNA double helix has a width of about 2 nm a pitch of 3.4–3.6 nm (10 base pairs). dsDNA is fairly stiff and rigid on the nanometer scale, with a persistence length of 50 nm, which corresponds to about 150 base pairs, while ssDNA is flexible with persistence length of only about 1 nm.[4–6] (Persistence length reflects the stiffness of the polymer chain and is defined as the length over which all correlation in the direction of a tangent is lost).

Electrostatics of DNA

The dsDNA helix is among the most densely charged molecules in nature, due to the charge of the phosphates closely spaced together in its backbone. In the presence of counterions, some of this charge is neutralize by Manning condensation (Figure 2.2), when counterions associate with DNA. The criterion for when Manning (counterion) condensation can occur is based on the dimensionless Manning ratio ζ:[7]

$$\zeta = \frac{l_B}{b}, \tag{2.1}$$

where b is the average distance between the charged phosphate groups on the backbone and

$$l_B = \frac{e^2}{4\pi\epsilon_r\epsilon_0 k_B T} \tag{2.2}$$

is the so called Bjerrum length. (e is the charge of an electron, ϵ_r and ϵ_0 are the relative and vacuum permitivity, respectively, k_B is the Boltzmann constant and T is the absolute temperature). For two elementary charges separated by the Bjerrum length, the electric potential energy is the same

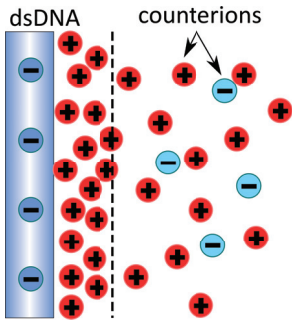

Figure 2.2: Manning condensation showing the counterions associated with the double-stranded DNA as a result of its high charge density.

as the thermal energy.

In aqueous solutions at room temperatures, the Bjerrum length is approximately $l_B \approx 0.715$ nm and the distance between the DNA charges is $b = 0.17$ nm. Their ratio – the Manning ratio $\zeta = 4.2$ is larger than 1, meaning that more than one charge is present within a Bjerrum length and as a result, counterions condense around the charged polymer. This condensation occurs for DNA and its charge is neutralized to the critical charge density given by the Bjerrum length (0.715 nm).

DNA hybridization and denaturation

The thermodynamics of DNA hybridization and denaturation will be discussed in more detail in a later section of this thesis (2.2.4), but some of the key elements will be introduced here.

DNA hybridization is the process of establishing a duplex from complementary anti-parallel single nucleic acid strands through hydrogen bonds and stacking attractions between the bases. Stacking in this case refers to stabilizing electrostatic and hydrophobic interactions between the adjacent bases. The duplex can undergo a reverse process – denaturation – separation into individual strands. It can be induced by chemicals, as well as by physical denaturation through, for example, heat, in which case it is also referred to as melting.

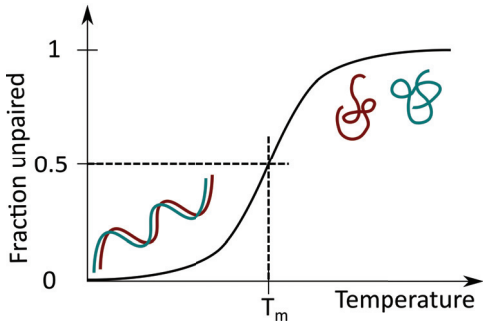

Figure 2.3: Illustration of the melting temperature which defines the point at which half of all the base pairs are dissociated.

The melting temperature (T_m) is defined as the temperature at which half of the DNA strands are denatured (Figure 2.3). It depends on the length of the DNA double helix as well as on its specific nucleotide sequence.

DNA in nanotechnology

The nucleotide sequence and its precise interactions with other nucleotides, governed by the rules of complementarity, allows DNA to fulfil its role of a biological blueprint. The sequence of bases encodes the genetic information, where a group of three bases forms a codon which signifies a single amino acid. The genetic information is then stored by DNA, replicated to be included in other cells and translated into ribonucleic acid (RNA) and further into protein. The higher order structure and the complementarity rules are at the basis of DNA's biological function.

The same properties that are at the basis of DNA's ability to perform its biological role, namely the dependence of its structure and interactions on the sequence of nucleobases, led to the exploration of DNA in nanotechnology. DNA nanotechnology uses DNA purely as a structural building block, not using the codon amino acid alphabet, but taking advantage of its structural properties and interactions.[5] The possibility to design and produce a custom nucleotide sequence (with precision at nanoscale) allows to control the molecule's higher order structure and its interactions with other molecules (DNA or other). This provides the structural blocks, con-

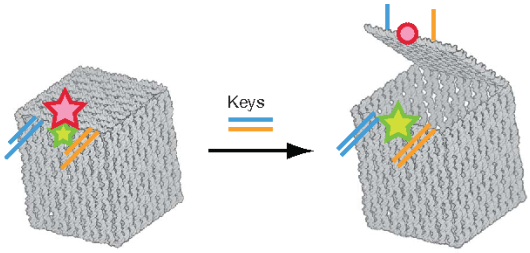

Figure 2.4: DNA origami box. A box with lid that can be opened made by self-assembly of DNA. The box can be unlocked using molecular ”keys” in a ”lock” (shown as orange and blue lines), In red and green are fluorescent dyes reporting when the box is opened. Reproduced with permission from Andersen et al.,[8]copyright (2009) Springer Nature.

nectivity and programmability suitable especially for bottom-up molecular self-assembly,[4] i.e. a process in which the higher-order structure is created spontaneously from the interactions of its components. DNA nanotechnology comprises design of DNA-based structures and objects in both two and three dimensions, such as lattices, nanotubes, polyhedra and other shapes,[8–11] structures that can serve as a scaffold for assembly of other structures,[12,13] as well as functional devices – nanomachines[14–17] and DNA computers.[18,19] One of the many examples is shown in Figure 2.4, namely a self-assembled DNA box that can be opened using molecular ”keys”.

DNA analogues

Nucleic acid analogues are artificially prepared polymers structurally similar to nucleic acids, but with one or several of the main nucleic acid components altered (phosphate, sugar - pentose and/or nucleobase). An altered nucleobase gives the polymer different base pairing properties than naturally occurring nucleic acids, while a change in the backbone will affect other properties, such as charges, hydrophobicity, stiffness, susceptibility to enzymes, etc.

Analogue nucleic acids with changes to the backbone include peptide nucleic acid (PNA),[20] Morpholino,[21] locked nucleic acid (LNA),[22] glycol nucleic acid (GNA)[23] and threose nucleic acid (TNA)(Figure 2.5).[24]

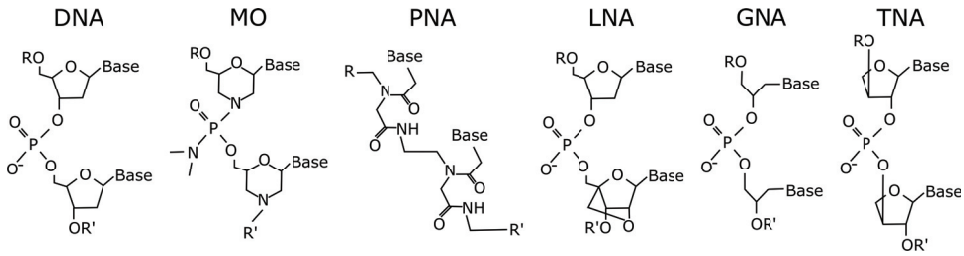

Figure 2.5: Comparison of backbones of DNA, and nucleic acid analogues: Morpholinos (MO), peptide nucleic acid (PNA), locked nucleic acid (LNA), glycol nucleic acid (GNA) and threose nucleic acid (TNA). R and R' denote the rest of the polymer.

PNA has its pentose-phosphate backbone replaced by N-(2-aminoethyl)-glycine monomers linked by peptide bonds. The backbone is free of charges and the binding with DNA through hybridization is stronger than that of DNA-DNA pairs, with PNA-PNA duplexes being even more stable. It is also resistant to degradation by nucleases and proteases, stable over a wide pH range and more hydrophobic than DNA.[25] Their applications are in gene expression modification, therapy,[25–27] and in nanotechnology and biosensing.[28–30]

Morpholino oligomers (MO) have a backbone of methylenemorpholine rings linked through phosphorodiamidate groups. Similar to PNA, their backbone is uncharged and they are resistant to nucleases and proteases, but they also have good solubility.[21] They are mainly used in molecular biology for gene expression modification by binding to ribonucleic acid (RNA) with a potential to be used in gene therapy.[31–33]

Locked nucleic acid is an RNA analogue with an extra bridge within the ribose molecule. This conformation enhances base stacking and stabilizes the duplexes.[34] Its uses are also within molecular biology, genomics and potentially therapy.[35]

Glycol nucleic acid is a nucleic acid analogue with a backbone consisting of glycol units linked by phosphodiester bonds, i.e. the pentose is substituted with a glycol, making it the simplest nucleic acid analogue. Its base pairing is stronger than that of natural nucleic acids, with a high melting

temperature.[36,37]

Threose nucleic acid contains a four-carbon threose sugar instead of the five-carbon pentose sugar found in DNA and RNA. It can base pair with both DNA and RNA, and similarly to other nucleic acid analogues, it is resistant to enzymatic degradation. TNA polymerases have been engineered, allowing transcription and translation between DNA and TNA,[38] which in turn led to preparation of TNA aptamers.[39,40]

2.1.2 DNA hydrogels and their applications

Hydrogels are three-dimensional polymer networks of both natural and man-made origin. They are created by crosslinking polymers through covalent bonds, non-covalent bonds, physical entanglements or a combination of these.[41,42] The cross-links are not disrupted by addition of water and as much as 99% of the weight of a swollen hydrogel can be water.[41] The elastic network along with the high water content gives hydrogels their unique properties of both solids (elasticity) and liquids (transport of materials, diffusion).[43] Their composition makes them similar to extra-cellular matrix, non-abrasive and often biocompatible.

Some hydrogels, often referred to as responsive hydrogels,[44,45] adjust their properties (such as swelling equilibrium, mechanical or optical properties[46]) to the changes in their environment, such as pH, temperature, ionic strength, light or a biomolecule (Figure 2.6).[45] Especially in the case of volume phase transitions, a large, even discontinuous, change in the hydrogel volume can be induced by a virtually infinitesimal change in one of the these stimuli, as the underlying hydrogel network changes its structure abruptly.[47,48]

Using DNA and/or DNA analogue within a hydrogel allows for its interactions on the molecular level to be translated to changes in the hydrogel's equilibrium state. DNA provides great control, specificity and sensitivity in its interactions with other DNA strands as well as various other molecules via aptamer reactions (given that the DNA sequence was chosen as an aptamer – a DNA molecule selected so that it specifically binds to another

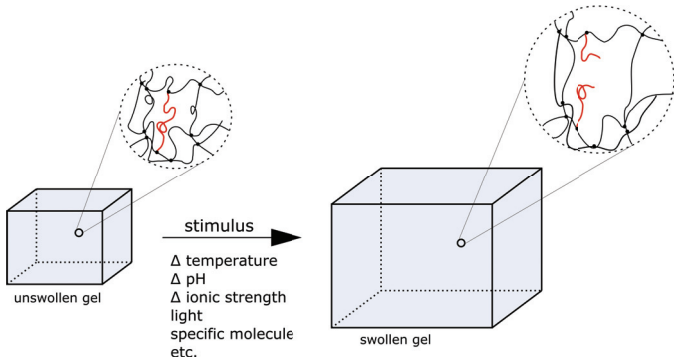

Figure 2.6: In responsive hydrogels, a change at the molecular level leads to a change in the hydrogel's equilibrium state.

non-DNA molecule). The hydrogel serves to amplify the signal detected at the nanoscale to a micro- or even macroscale that allows for monitoring of the molecular reaction in various sensor devices. Alternatively, the molecular input can be used to finely adjust the hydrogel properties, leading to applications in targeted drug delivery, cell culturing or various nanodevices.

The sensing oligonucleotide sequence can be incorporated into the hydrogel in a variety of ways and the binding of the target to the sensing strand commonly leads to shrinking, swelling or dissolution of the hydrogel. Hydrogels can be made of pure DNA, but designs incorporating DNA with other copolymers are more common. Most hydrogels employ aptamer sequences for target detection or as triggers for release.

A number of hydrogels intended for targeted drug release have been reported in the recent years. Lai and cowerkers[49] have prepared a DNA-polyethylene glycol based hydrogel for controlled sequential release of biologically relevant signaling molecules, which works as follows (see also Figure 2.7(a)): (i): a small signaling molecule (ex. adenosine) binds to its aptamer sequence within the core of the hydrogel, releasing a trigger DNA sequence originally hybridized with the aptamer; (ii): the trigger DNA sequence in turn binds to its complementary DNA in the shell of the hydrogel, displacing the biologically relevant protein cargo that was previously bound to the shell DNA.

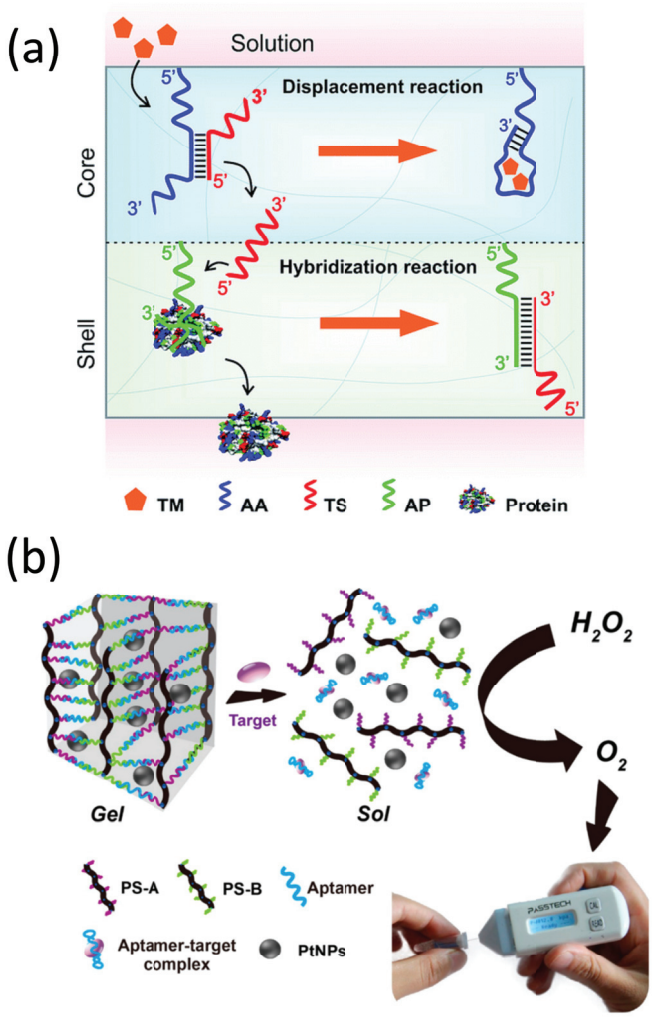

Figure 2.7: (a) Schematic illustration of the mechanism of action of the hydrogel prepared by Lai and coworkers. TM – triggering molecule, AA – aptamer sequence, TS – triggering DNA sequence, AP – aptamer sequence binding to the protein. Further description can be found in the text. Reprinted with permission from Lai et al.[49] Copyright (2017) The Royal Society of Chemistry. (b) Schematic illustration of the working principle of a hydrogel prepared by Liu and colleagues. PS-A and PS-B are polyacrylamide-DNA conjugates. Detailed description can be found in the text. Reprinted with permission from Liu et al.[50] Copyright (2017) American Chemical Society.

Chen et al.[51] used DNA-polyacrylamide hydrogel to functionalize the surface of nanoparticles loaded with a cancer drug. The DNA crosslink includes an anti-ATP (adenosine triphosphate) aptamer sequence that binds ATP (overexpressed in cancer cells), leading to crosslink opening, gel dissolution and release of the drug.

As another example, Singh et al.[13] combined DNA with carbon dots in a DNA-carbon dot hydrogels for sustained, pH-dependent drug release.

As an example of a pure DNA hydrogel for drug delivery, we can look at the work of Li and coworkers[52] who developed self-assembled pure DNA nanohydrogels with aptamers, disulfide links or therapeutic genes, for targeted and stimuli-responsive gene or drug delivery.

A unique hydrogel by Li et al.[7] has both sensing and drug delivery functionality: A DNA-polyacrylamide hydrogel consisting of two layers: the outer one with aptamer ssDNA for catching cancer cells, and the inner one with dsDNA for sequestering of cancer drug to kill the caught cells.

When it comes to hydrogels for sensing applications, a readout method becomes an important part of the design. One of the most common readout methods is the colorimetric readout using gold nanoparticles sequestered inside the hydrogel. The particles are released due to the reaction of the hydrogel with its target molecule and impart a typical red color to the solution, which can be detected with the naked eye. Huang et al.[53,54] used DNAzymes activated by the target ions (lead or uranium) to disrupt the DNA crosslinks in DNA-crosslinked polyacrylamide hydrogels, inducing hydrogel dissolution and subsequenct release of the nanoparticles. Same readout method was used by Ma et al. for the detection of glucose.[55] In this work, polyacrylamide chains crosslinked via dsDNA were used to prepare a hydrogel containing encapsulated gold nanoparticles. The DNA has an aptamer sequence for specific binding of glucose which leads to crosslink opening and release of nanoparticles.

A colorimetric readout not based on gold nanoparticles developed by Wei et al.[56] used a microfluidic device for visual detection of multiple targets (such as cocaine, adenosine, lead). In their setup, some of the channels

in the detection microfluidic device were blocked by aptamer-crosslinked hydrogels. The binding of the analyte to the aptamer triggered dissolution of the hydrogel, unblocking the flow within the device and allowing the color indicator to travel to the observation spot giving a positive readout.

An electrochemical readout method has also been reported and can offer better quantitative measurements (if desired) than visual colorimetric readout. For example, Liu et al.[57] designed a DNA-hybrid hydrogel with an electrode for readout of cancer-specific microRNA concentration. Mao et al.[58] combined both electrochemical and colorimetric readout for detection of bilirubin and hydrogen peroxide by using a surface-bound DNA hydrogel constructed on the surface of an electrode.

Diffraction gratings have also been used as readout methods, for example by Bai et al.[59] for virus detection, or Wang et al.[60] for thrombin detection in polyacrylamide hydrogels with DNA-aptamer crosslinks. In both cases, the hydrogel itself was prepared in the form of a grating using soft lithography and the position of the diffraction peaks obtained by laser light passing through the grating allows for monitoring of the hydrogel swelling and shrinking.

Liu et al.[50] and Yan et al.[61] prepared sensing systems that took advantage of other available readout instruments, namely pressure detector and glucometer, respectively. In the first case (see Figure 2.7(b)), polyacrylamide chains with attached ssDNA (PS-A, PS-B) are crosslinked by a third linker strand carrying an aptamer sequence specific to the analyte. The hydrogel also contains Pt nanoparticles (PtNPs). The binding of the analyte dissolves the hydrogel, releases the Pt particles, which then catalyse the reaction from H_2O_2 to O_2. The oxygen then leads to pressure increase in a sealed environment which can be measured by a pressure detector. In the second case, aptamer-crosslinked hydrogel with trapped glucoamylase dissolves after target binding and releases the enzyme which can hydrolyze amylose to produce a large amount of glucose. The glucose can then be measured by a glucometer.

Another readout method was used by Ye and coworkers,[62] namely a photonic crystal-based readout, using colloidal photonic crystal hydrogels pre-

pared with heavy metal ion-responsive aptamers as crosslinks. The binding of the heavy metal ion leads to the aptamers adopting a different structure (hairpins or G-quadruplexes), shortening the chains and leading to a deswelling of the hydrogel that can be detected as a change in the Bragg diffraction peak position, allowing quantitative concentration measurement.

Apart from sensing and targeted drug delivery, DNA-based hydrogels can be used as substrates for cell culturing and tissue engineering,[63] where the responsiveness adds unique options, such as the possibility to control the delivery of bioactive molecules to the cultured cells,[64] or the mechanical properties of the medium.[57,65–67] The mechanical properties of the substrate play an important role in modulating interactions between the cell and the matrix, and influence biological processes, such as proliferation, movement and differentiation of cells.

DNA hydrogels have also been used to prepare various nanodevices and logic gates.[19,68]

2.1.3 Model system: Oligonucleotide-co-acrylamide hydrogels

The hydrogels used in the work presented here are polyacrylamide hydrogels with additional crosslinks based on a nucleic acid (DNA) or a nucleic acid analogue (Morpholino) oligonucleotides. The particular molecular design of the hydrogels is based on that of Nagahara and Matsuda[69] and used in our group previously by Tierney and Gao.[70,71]

As depicted in Figure 2.8, the hydrogels consist of a polyacrylamide network crosslinked by two different types of crosslinks. N,N'-methylenebisacrylamide (Bis) forms covalent crosslinks between the polyacrylamide strands, and oligonucleotide strands present in the network form partially double-stranded physical crosslinks. The oligonucleotide strands are covalently attached to the polyacrylamide network at their 5' ends and have a complementary region at their 3' ends that leads to their hybridization via hydrogen bonds and formation of a reversible duplex.

Figure 2.8: Schematic illustration of one oligonucleotide crosslink within the hydrogel network of our model hydrogels.

The sensing strand (S) and blocking strand (B) are functionalized with acrydite groups at their 5' ends, allowing them to be covalently bound to the polyacrylamide during the free radical polymerization. S and B are mixed before polymerization so that the hybridization occurs while the strands are free in a solution and this ensures that they appear as duplexes in the hydrogel. The crosslink duplex can be opened by a target (T) oligonucleotide strand that is also complementary to S strand on the same region as B. Additionally, the complementarity region between T and S is longer than the region of complementarity between S and B (blocking region), so that the complementary sequence unblocked by B (the toehold) is immediately available for T to bind to. The inital binding is followed by branch migration – a back-and-forth migration of the junction point between the three strands, until the blocking strand is completely displaced. The presence of the toehold makes the binding of T to S more stable and thus thermodynamically more favourable than the SB duplex and the hydrogel relaxation that follows the crosslink opening increases the distance between ST and B strands so that the probability of a reverse reaction is reduced.

2.2 Properties and processes affecting the swelling

The dependence of the swelling equilibrium on a hydrogel's environment is one of its most useful and most used properties. It is generally easy to ob-

serve and quantify, and truly manifests the underlying molecular processes on a macroscopic level for sensing applications. On the other hand, the swelling can dramatically change many of the hydrogels properties, from its elasticity, through permeation to refractive index, making hydrogels good candidates for applications requiring tunability of various properties.

The overall change in the swelling equilibrium is the result of a complex cascade of processes. In the case of the model system studied in this work, these processes are the permeation of the target into the hydrogel, its initial binding followed by the branch migration (which together constitute a toehold-mediated strand displacement process), oligoncleotide-crosslink opening, relaxation of the network and swelling. These processes are sequential for each target, but happen simultaneously throughout the hydrogel and have profound effects on one another.

In the following, these processes will be discussed, as they are expected to take place in oligonucleotide-co-acrylamide hydrogels described in section 2.1.3.

2.2.1 Swelling

Swelling of nonionic hydrogels can be described by Flory-Rehner theory.[72] The equilibrium swelling is reached by balancing the osmotic pressure arising from the mixing of hydrogel with the solvent (Π_{mix}) and the osmotic pressure resulting from network elasticity (Π_{el}). The enthalpy of mixing can favour both swelling and deswelling, and the entropy of the elastic forces of the chains opposes the swelling. Osmotic pressure due to mixing is given as

$$\Pi_{\text{mix}} = -\frac{RT}{V_{\text{H}_2\text{O}}} \left(\ln\left(1-\varphi\right) + \varphi + \chi\varphi^2\right), \tag{2.3}$$

and the osmotic pressure due to the elasticity of the polymer chains is

$$\Pi_{\text{el}} = \frac{vRT}{V_0} \left(\frac{\varphi}{2\varphi_0} - \left(\frac{\varphi}{\varphi_0}\right)^{\frac{1}{3}}\right). \tag{2.4}$$

In the equations, R is the molar gas constant, T the absolute temperature, V_{H_2O} the molar volume of the solvent, V_0 the gel volume for the reference state (as prepared), φ the volume fraction of the polymers and φ_0 the reference volume fraction of the polymers, v is the molar number of elastic chains at reference volume fraction φ_0 and χ the Flory-Huggins polymer-solvent interaction parameter.

In case of ionic hydrogels a third term – Donnan term Π_{ion} – needs to be added, reflecting the requirement for electroneutrality both in the hydrogel and the immersing solution, and for equal chemical potential of ions across the boundary between them. Alterations to the charge of the hydrogel will lead to flux of ions and water either into or out of the hydrogel. It also needs to be said, that the presence of charges in the hydrogel has an effect on the mixing term as well, as this results from interactions between the hydrogel and the solvent.[73] The ionic Donnan term has the following form

$$\Pi_{\text{ion}} = RT \sum (C_{i,2} - C_{i,1}) \tag{2.5}$$

where $C_{i,1}$ and $C_{i,2}$ are the concentration of mobile ion i in the solvent and in the gel, respectively.

The total osmotic pressure Π is a sum of these contributions and defines the hydrogel's swelling equilibrium ($\Pi = 0$):

$$\Pi = \Pi_{\text{mix}} + \Pi_{\text{elastic}} + \Pi_{\text{ion}}, \tag{2.6}$$

In case of the model DNA hydrogels, the swelling response arises from a change to two of the osmotic pressure contributions – elastic and ionic. The opening of the DNA crosslink leads to a reduction in the number of the elastic network chains, affecting the v term, while the accumulation of the negatively charged DNA target strands in the hydrogel network leads to influx of counterions (and the solvent). Morpholino-hydrogels, on the other hand, are electrically neutral, and their swelling is a result of crosslink opening only.

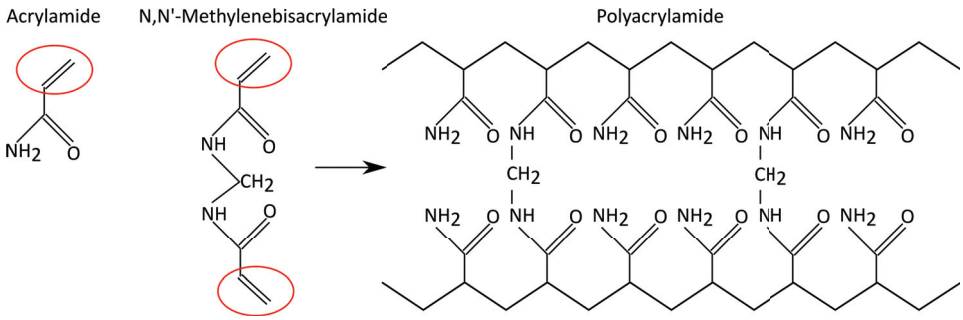

Figure 2.9: Chemical formulas of acrylamide monomer and N,N'-Methylenebisacrylamide (Bis) crosslinker, as well as the structure of the resultant polyacrylamide network. Reactive groups are highlited in red.

2.2.2 Properties of polyacrylamide hydrogel networks

Polyacrylamide hydrogels, which are the basis of oligonucleotide-co-acrylamide hydrogels, are polymerized by free radical polymerization of the monomer – acrylamide (Aam) and crosslinker – N,N'-methylenebisacrylamide (Bis) (Figure 2.9). They are neutral and generally do not bind to water soluble macromolecules. They consist of a chemically crosslinked network of single chains,[74] which possess a large degree of mobility.[75] The radius of a polyacrylamide fiber has been experimentally determined by Williams et al. to be $a_f = 0.8$ nm.[76] Polyacrylamide hydrogels are among other applications used in gel electrophoresis and thus many of their properties relevant for this work have been well studied.

Traditionally, the concentrations of the Aam and Bis in a polyacrylamide hydrogel are expressed using two parameters: total monomer concentration (%T, in g/100 ml) and weight percentage of crosslinker (%C):

$$\%\mathrm{T} = \frac{m_{\mathrm{Aam}}[\mathrm{g}] + m_{\mathrm{Bis}}[\mathrm{g}]}{V_{\mathrm{total}}[\mathrm{mL}]} \times 100, \tag{2.7a}$$

$$\%\mathrm{C} = \frac{m_{\mathrm{Bis}}[\mathrm{g}]}{m_{\mathrm{Aam}}[\mathrm{g}] + m_{\mathrm{Bis}}[\mathrm{g}]} \times 100. \tag{2.7b}$$

In the work presented here a different notation is used. The concentration

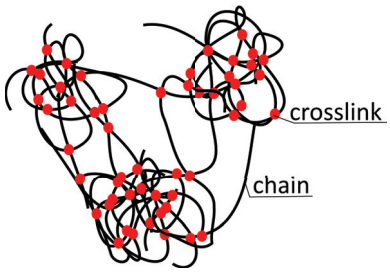

Figure 2.10: Inhomogenous hydrogel network, with areas of higher and lower crosslink density.

of acrylamide is given directly in g/100 mL, and the concentration of Bis is expressed as a molar percentage of the acrylamide concentration. The concentration of double-stranded oligonucleotide crosslinks is also given as a molar percentage of acrylamide and this allows to easily add the crosslinker concentrations (since both Bis and oligonucleotides serve as crosslinkers).

Hydrogels in general, and free radical-crosslinked hydrogels in particular, inherently exhibit a significant level of heterogeneity in their structure. This is due to defects, such as loops, crosslinker-crosslinker shortcuts, and dangling ends, as well as ”freezing-in” of the thermal concentration fluctuations at the gelation moment (so called ”frozen inhomogeneities). More importantly, hydrogel imhomogeneities arise also due to inhomogeneities in crosslink density (Figure 2.10).[77–80] During the gelation process, the formation of a crosslink leads to the creation of a domain with higher density, favouring further crosslinking in this region and the formation of a densely crosslinked nanogel with a size in the order of 1 – 10 nm. Eventually these nanogels become crosslinked through areas of sparser crosslink density and form a macrogel. The distance between the individual nanogels can be in the order of 10 – 100 nm.[79] Upon swelling, these heterogeneities become even more pronounced as areas of higher crosslink density swell less than those with lower crosslink density.[81,82] In the case of polyacrylamide hydrogels, heterogeneities have even been observed at length scales of hundreds of μm.[74]

Inhomogeneities in the hydrogel network affect its phase transition, me-

chanical properties,[83] volume changes (swelling and deswelling)[77] as well as optical clarity and permeability of the hydrogel.[78] Inhomogeneities also lead to a broad distribution of strand lengths and consequently a broad distribution of pore sizes.

The pore size of polyacrylamide hydrogels has been measured repeatedly using various techniques, with a wide range of results,[84–88] due to their broad distribution.[89–91]

For example, according to Stellwagen et al, the effective pore radius of a polyacrylamide hydrogel is:[91]

$$r_p = 290\ (\%\mathrm{T})^{-0.38}\ \mathrm{nm},\ \text{for 1\%C hydrogels}, \tag{2.8a}$$

$$r_p = 290\ (\%\mathrm{T})^{-0.55}\ \mathrm{nm},\ \text{for 2\%C hydrogels}. \tag{2.8b}$$

2.2.3 Permeation through hydrogels

Thanks to their high water content, hydrogels allow small molecules to permeate through their aqueous phase. The concentration of the solute in the hydrogel depends on the hydrogel's permeability, which is a characteristic that depends both on the properties of the hydrogel and those of the permeating molecule. Permeability P can be defined as the product of the diffusion coefficient D, which is a transport property, and a partition coefficient K, which is a thermodynamic property:[92]

$$P = KD. \tag{2.9}$$

This comes from a definition of steady state flux $|\vec{J}|$ of solute across a membrane from a donor phase to a receptor phase:

$$|\vec{J}| = \frac{KD}{L}\Delta C, \tag{2.10}$$

where L is the thickness of the membrane and ΔC is the concentration difference of the solute in the donor and receptor phase.

Partitioning

Partitioning refers to the equilibrium distribution of the solute between the hydrogel and the immersing solution, as given by the partition coefficient K:

$$K = \frac{C_{\text{gel}}}{C_0}, \tag{2.11}$$

where C_{gel} is the equilibrium concentration of the solute in the hydrogel and C_0 its concentration in the immersing solution. The partitioning depends on the chemical and physical properties of the solute and the hydrogel, as well as on their interactions. Assuming these contributions to be independent, the overall partition coefficient can be written as[92]

$$\ln(K) = \ln(K_{\text{size}}) + \ln(K_{\text{conf}}) + \ln(K_{\text{el}}) + \tag{2.12}$$

$$+ \ln(K_{\text{hphob}}) + \ln(K_{\text{biosp}}) + \ln(K_{\text{other}}), \tag{2.13}$$

where $size$, $conf$, el, $hphob$, $biosp$ and $other$ refer to effects based on size of the solute and network strands, their conformation, as well as based on electric, hydrophobic and biospecific interactions and other effects, respectively. While size and conformational effects will lead to the solute preferring the immersing solution over the hydrogel and subsequently leading to K_{size} and $K_{\text{conf}} < 1$, other interactions, such as electrostatic, biospecific and hydrophobic, can lead to potential accumulation of the solute inside the hydrogel with the corresponding partition coefficients being larger than 1.

The contribution of the size effect to the partitioning can be estimated by a model developed by Ogston. In the model, the solute molecules are assumed to behave as spheres of radius a in a hydrogel matrix composed of infinitely long randomly-placed fibers of radius a_f, with interactions being purely hard-sphere in nature[93]

$$K_{\text{size,conf}} = \exp\left[-\varphi\left(1 + \frac{a}{a_f}\right)^2\right]. \tag{2.14}$$

The Ogston model was previously found to provide an adequate fit for partitioning data of dextran[76] and polyethylene glycol, bovine serum albumin

and RNase[74] in neutral polyacrylamide hydrogels. Hydrogel crosslinking inhomogeneities discussed earlier can have a profound effect on the partitioning.[74,92]

Diffusion

Diffusion is a net movement of molecules along a concentration gradient, i.e. from areas of high concentration c to areas of low concentration c. A flux vector $\vec{J}$ represents both the quantity and the direction of the transfer per unit time per area unit. This is captured by Fick's first law which defines a diffusion coefficient D as the proportionality constant between the flux J and the concentration gradient in a spatial direction x_i:

$$\vec{J} = -D\frac{\partial c}{\partial x_i}. \tag{2.15}$$

The diffusion reaction itself is given by Fick's second law and it is a parabolic partial differential equation which for a constant diffusion coefficient has the following form:

$$\frac{\partial c(x,t)}{\partial t} = D\nabla^2 c(x,t), \tag{2.16}$$

where t is time and ∇^2 is the Laplace operator:

$$\nabla^2 n(x,t) = \sum_i \frac{\partial^2 n(x,t)}{\partial x_i^2}. \tag{2.17}$$

In the following, the diffusion data are usually referring to standardized conditions of $20°$C. The diffusion coefficient of ssDNA with 10 or more bases in aqueous solutions has been estimated to:[94]

$$D_{\text{ssDNA}} = 7.38 \times 10^{-6} \times N^{-0.539}\ \text{cm}^2\text{s}^{-1}, \tag{2.18}$$

where N is the number of nucleotides.

For solutes in water, the diffusion coefficient mainly depends on their

molecular weight. However, D is not a property of the solute itself, but reflects the properties of both the solute and the environment in which it is diffusing. Inside hydrogels, solutes can diffuse through the aqueous phase, in the spaces between the polymer chains. In the following, the discussion will be limited to the diffusion of spherical solutes in hydrophilic networks without interactions between the solute and the polymer other than the excluded volume effects. The diffusion coefficient in this case depends mainly on factors that influence the size of the spaces not occupied by the polymer chains, such as the relative size of the solute compared to the pore size of the network or polymer chain mobility. In general, solute diffusivity will decrease with an increasing crosslinking density, size of the solute and a decreasing volume fraction of the polymer in the hydrogel.[95]

A variety of models have been proposed to describe the reduction in diffusivity of solutes in hydrogels compared to that of free diffusion in aqueous solutions. They can be sorted into several categories: free volume theory,[96] based on a solute diffusing by jumping into adjacent available voids within the solvent; hydrodynamic theory,[97–99] based on Stokes-Einstein equation for solute diffusivity, where the solute is affected by a frictional drag; obstruction theory,[93,100–103] which assumes the polymer chains to be obstacles that increase the path length of the diffusing solute and act as a sieve; and lastly a combined obstruction and hydrodynamic model.[104] Amsden[75] identified the hydrodynamic model by Cukier[97] to provide the best fit for hydrogels, where the polymer chains have a high level of mobility (ex. polyacrylamide, polyethelene oxide, polyvinyl alcohol) and the Amsden obstruction model[102] to be the best fit for hydrogels with chains of low mobility at molecular level (ex. alginate, agarose).

The Cukier hydrodynamic model[97] estimates the decrease in diffusion coefficient inside the gel D_g compared to that in solution D_0 as:

$$\left(\frac{D_g}{D_0}\right)_{\text{Cukier}} = exp\left(-k_c\, a\, \varphi^{0.75}\right), \tag{2.19}$$

where k_c is an undefined constant for a given polymer-solvent system, a is the radius of the solute and φ is the volume fraction of the polymer inside

the hydrogel. By comparing this model to experimental data, Amsden[75] suggests that the dependence on the solute radius r_s seems to be a weak power function, rather than the linear dependence suggested by the model. While application of the Cukier model requires the knowledge of the k_c constant for the polymer-solvent system, an empirical equation of a similar form was derived by Park and coworkers for the diffusion of benzospiropyran dye and bovine serum albumin in polyacrylamide gels:[105]

$$\left(\frac{D_g}{D_0}\right)_{\text{Park}} = exp\left(-3.03\, r_h^{0.59}\, c^{0.94}\right), \tag{2.20}$$

where r_h is hydrodynamic radius in ångström and c the acrylamide concentration in g/mL. This equation was also validated by measuring the diffusion of D_2O, urea, and sucrose in polyacrylamide hydrogels. The radius of the molecule appears here as a power function, not linear, as suggested by Amsden for the Cukier model as well.[101]

Williams et al[76] found another hydrodynamic model, the Brinkman effective-medium model to provide the best fit for diffusion of dextran in polyacrylamide hydrogels, if the radius of the solute was determined from partitioning data. Tong and Anderson,[74] also found this model suitable for the diffusion of proteins (bovine serum albumin and RNase) in polyacrylamide, but not for linear polymers (polyethylene glycol). The Brinkman model has the form:

$$\left(\frac{D_g}{D_0}\right)_{\text{Brinkman}} = \left(1 + \frac{r_s}{\sqrt{\kappa}} + \frac{1}{3}\left(\frac{r_s}{\sqrt{\kappa}}\right)^2\right)^{-1}, \tag{2.21}$$

where κ is the Darcy permeability of the matrix, a measurable property of the hydrogel, which can also be estimated from a geometric model of the network.

2.2.4 Strand displacement through toehold exchange

Strand displacement refers to a reaction in which one strand (target strand T) displaces another strand (blocking strand B) in binding to a third strand (sensing strand S) which is at least partially complementary to both. If T and B are complementary to S on the exact same region, the initial bind-

ing region for T is provided by the spontaneous pairing and unpairing of the end basepairs in S-B duplex (i.e. fraying). Reactions relying on fraying have small reaction rate constants, on the order of $0.5\ \mathrm{M}^{-1}\mathrm{s}^{-1}$. The reaction rate can be increased by providing a so-called toehold to target T, i.e. an overhang region on S that is complementary to T, but not blocked by B. This region provides an initial binding site for the target.

Strand displacement

Strand displacement can follow two pathways: dissociative and sequential.[106,107] The dissociative pathway is of importance only at temperatures close to the duplex's melting temperature, as it involves an initial complete dissociation of the DNA duplex, before the target strand binds to the sensing strand. At lower temperatures, the fraction of completely denatured dsDNA duplexes in a solution is low, while at the melting temperature, it is 50 %. At lower temperature, the sequential pathway dominates and is undoubtedly the more interesting case. It starts by the binding of the target T to the sensing strand S, whether initiated by fraying or mediated by binding to a toehold, forming a three-strand complex. The process is then continued by a back-and-forth branch migration mechanism.[107]

Initial binding – hybridization

The toehold-mediated strand displacement is initiated by hybridization of the toehold regions of T with the complementary regions of S. Hybridization – the process of formation of the DNA double-helix from two complementary ssDNA strands – has been briefly described in section 2.1.

The thermodynamics of DNA hybridization is often treated as a two-state process, with the strands being either separate, or hybridized, neglecting the possibility of any intermediate states with partial binding of the two ssDNA:

$$\mathrm{dsDNA} \underset{Keq}{\overset{K_{eq}}{\rightleftharpoons}} \mathrm{ssDNA}_1 + \mathrm{ssDNA}_2$$

The equilibrium constant K_{eq} of this reaction is

$$K_{eq} = \frac{[\text{ssDNA}_1][\text{ssDNA}_2]}{[\text{dsDNA}]}. \tag{2.22}$$

The free energy of the hybridization ΔG depends on K_{eq}:

$$\Delta G^\circ = -RT \ln K_{eq} = -RT \ln \frac{[\text{ssDNA1}][\text{ssDNA2}]}{[\text{dsDNA}]}, \tag{2.23}$$

where R is the ideal gas law constant and T absolute temperature in kelvins. The melting temperature T_m occurs, by definition, when half of the duplexes are denatured, which leads to concentrations of all present DNA entities being equal, and equal to the initial concentration of the duplex (Figure 2.3). Thus the melting temperature is

$$T_m = \frac{\Delta G^\circ}{R \ln \frac{[\text{dsDNA}]_{\text{initial}}}{2}}. \tag{2.24}$$

Through the free energy, the melting temperature T_m is also related to other thermodynamic parameters, enthalpy ΔH° and entropy ΔS°, as $\Delta G^\circ = \Delta H^\circ - T\Delta S^\circ$. The hybridization of the two ssDNAs that behave virtually as random coils into a much stiffer dsDNA duplex comes with an entropic penalty that needs to be paid and the effect of which depends also on the temperature.

The dependence of the melting temperature on the thermodynamic parameters means that the knowledge of the melting temperature of a given sequence can be used to determine its thermodynamic parameters, but also that the knowledge of the thermodynamic parameters allows for estimation of the melting temperature. Since interactions between complementary base pairs depend to some extent on their neighbouring nucleotides, the DNA duplex can not be treated as a sequence of independent interacting base pairs. This is reflected in the nearest-neighbour model, which treats the DNA duplex as a sequence of interactions between two consecutive base

pairs.[108] For example, in a sequence:

$$5' \text{ G} - \text{T} - \text{T} - \text{A} - \text{C } 3' \tag{2.25}$$

$$3' \text{ C} - \text{A} - \text{A} - \text{T} - \text{G } 5', \tag{2.26}$$

The free energies of pairs GT/CA, TT/AA, TA/AT and AC/TG would be used, as well as initiation energies for the first and last base pair (GC and CG). While the nearest-neighbour model provides reasonably good results in most cases, its accuracy is limited among other things by its assumption that the DNA hybridization and melting is an all-or-nothing process, thus ignoring the possibility of intermediate, partially hybridized states, which can be more or less likely to occur, depending on the sequence in question.[109]

The nearest-neighbour model was developed for hybridization of free molecules in solution, but the tethering of DNA to a hydrogel network is likely to have an effect on the process. As there are few studies on hydrogel-bound DNA hybridization, some insight into the effect of immobilization can be obtained by looking at hybridization of DNA bound to hard surfaces. It has been found that the nearest-neighbours model does not always satisfactorily describe hybridization of surface-bound DNA[110,111] and that the rates of hybridization are affected by the length of the attached DNA,[110,112] the position of the complementary sequence (close or far from the attachment point),[113] the temperature,[110] the density of the immobilized DNA and inhomogeneities in this density.[111,114,115] The underlying mechanism for most of these effects is the shielding of the binding sites, which reduces the hybridization rate and lowers the melting temperature of the duplexes. The shielding can be mechanical in nature, when the binding sites are surrounded by other strands, or in close proximity to the surface which limits access to them; or due to electrostatic shielding, in cases of higher density of the surface-bound DNA, which repels the target DNA.

Unlike hard surfaces, polyacrylamide hydrogels are three-dimensional structures with polymer chains that have a high degree of mobility. Some of the effects observed for surface-bound DNA, such as the position of the complementary sequence affecting the hybridization rate, might not be as pronounced for hydrogels. One of the very few studies investigating DNA

hybridization inside gels was done by Fotin et al.,[116] in which they investigated the hybridization thermodynamics of DNA 8-mers bound to a polyacrylamide network. The observed melting curves had a similar shape to the ones for hybridization in solution, but the hybridization free energy ΔG° and the melting temperature T_m were decreased:

$$\Delta G^\circ(\text{gel}) = a\Delta G^\circ(\text{solution}) + g, \tag{2.27}$$

$$T_m(\text{gel}) = 1.2 \times T_m(\text{solution}) - 27.8^\circ\text{C}, \tag{2.28}$$

where $a = 1.1 \pm 0.2$ and $g = -3.2 \pm 0.4$ kcal/mol.

Toehold-mediated DNA strand displacement

The presence of the toehold on the target and on the sensing strand provides a region for initial attachment and greatly increases the forward reaction rate. Using toeholds allows to favour strand replacement in artificially designed system *in vitro* without the use of enzymes and has led to a construction of a variety of DNA devices, such as logic gates,[19,117–120] motors,[121,122] timer circuits,[123] devices for signal amplification[124,125] and neural network computations.[126]

Toehold-mediated strand displacement is a subcategory of toehold exchange reactions. The mechanism of toehold exchange is shown in Figure 2.11 and can be described by a three-step model developed by Zhang and Winfree:[127]

$$\text{SB} + \text{T(m, n)} \underset{k_{r(\gamma^n)}}{\overset{k_{f1}}{\rightleftharpoons}} \text{I}(m, n) \underset{k_b}{\overset{k_b}{\rightleftharpoons}} \text{J}(m, n) \underset{k_{f2}}{\overset{k_{r(\beta^m)}}{\rightleftharpoons}} \text{B} + \text{ST}(m, n) \cdot$$

In the presentation of their model, some of their notation will be used. Greek letters signify domains – particular regions on the DNA strand – and subscripts and superscripts define parts of these domains. As an example, domain β is formed by two subdomains: β^m describes the m bases at the 5' end, while β_m denotes all the other bases except for the m bases at the 5' end. The kinetic constants of association, dissociation and branch migration are also specified in the reaction equation.

As depicted in Figure 2.11, during toehold exchange, the target strand binds to the complex SB, as it has a unique toehold region γ^n, which is complementary to the $\bar{\gamma^n}$ domain of the S strand. The resulting intermediate complex I(m,n) is one where B binds more bases of S than T does. The branch migration process then can lead to T binding more bases of S than B does, and this complex is denoted J(m,n). Domain β^m then spontaneously dissociates releasing strand B and complex ST. The difference between general toehold exchange and the particular case of toehold-mediated strand displacement lies in the fact that in the generalized toehold exchange both T and B possess unique toeholds with S, while in the case of toehold-mediated strand displacement, only T has a toehold with S. The lack of toehold for B increases the likelihood that B is replaced by the target, which (including the toehold) has a longer complementary region to S, making the ST duplex thermodynamically more favourable than SB duplex. The reverse reaction is also suppressed as the likelihood of the displaced strands binding to the duplex again without a toehold is low.

The branch migration was previously described as a random-walk process,[106] but this behaviour was in disagreement with experimental data. Srinivas et al.[128] have investigated the thermodynamics of the toehold exchange in depth and found two phenomena that explain the strong dependence of the kinetics on the toehold length. A thermodynamic barrier results from the presence of the single-stranded DNA overhangs, crowding the junction point and forcing the strands to bend away from each other. To initiate the branch migration, this barrier has to be overcome. The branch migration was also found to occur significantly slower than the fraying of the individual bonds. This can be explained by greater structural rearrangement taking place during branch migration.

The dependence of kinetics of the DNA toehold exchange in general, and toehold-mediated strand displacement in particular, has been described by Zhang and Winfree.[127]

The kinetic constants of strands binding to their toeholds in a hybridization reaction are denoted k_{f1} and k_{f2} for binding of T to S and of B to S respectively. They assume these constants to be identical k_f. The constant

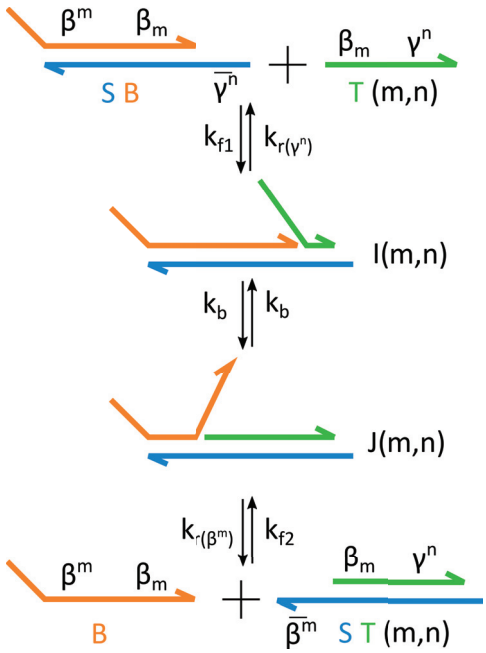

Figure 2.11: The mechanism of toehold exchange reaction. Invading strand T binds to the S strand through its toehold domain γ^n as the S strand possess a complementary domain $\bar{\gamma^n}$. The intermediate complex I(m,n) represents all the states in which B binds to more bases on $\bar{\beta_m}$ than T. As the branch migration continues, T eventually binds to more bases than B and this is represented by the complex J(m,n). Domain β^m, which represents the toehold of strand B, spontaneously dissociates, releasing the products of the reaction: strand B and complex ST. This reaction is reversible as B can bind to ST through its own toehold. The kinetic constants for each reaction are shown in the scheme. The arrows on the strands denote the 3' end. Adapted from Zhang and Winfree.[127]

k_f is difficult to estimate from first principles and probably reflects the kinetics of hybridization.[127] It strongly depends on the nucleobase sequence in the toehold region (i.e. strong toeholds with only GC bases have k_f twice as large as toeholds with GC:AT = 50:50, and 20 times as large as weak toeholds with only AT bases). The best-fit values provided for the association constants are:[127]

$$k_f = 3 \times 10^6 \text{ M}^{-1}\text{s}^{-1}, \text{ for intermediate strength toeholds,} \tag{2.29a}$$

$$k_f(\text{strong}) = 6 \times 10^6 \text{ M}^{-1}\text{s}^{-1}, \text{ for strong toeholds,} \tag{2.29b}$$

$$k_f(\text{weak}) = 4 \times 10^5 \text{ M}^{-1}\text{s}^{-1}, \text{ for weak toeholds.} \tag{2.29c}$$

Dissociation constants for the dissociation of T from S and of B from S are denoted $k_{r(\gamma^n)}$ and $k_{r(\beta^m)}$, respectively. The dissociation constant $k_{r(\gamma^n)}$ can be calculated from the corresponding association constant k_f, the binding energy between γ^n and its complement $\bar{\gamma_n}$: $\Delta G^\circ(\gamma^n) < 0$, and the length of the β_m domain ($b - m$ where b is the length of the full β domain):[127]

$$k_{r(\gamma^n)} = k_f \times \frac{2}{b-m} \times e^{\Delta G^\circ(\gamma^n)/RT}. \tag{2.30}$$

The dissociation constant $k_{r(\beta^m)}$ is calculated accordingly.

The toehold binding energy $\Delta G^\circ(\gamma^n)$ and subsequently the dissociation constant depends on the length of toehold as well as its strength, i.e. its GC content. Zhang and Winfree[127] used toehold binding energy values from works by Santa Lucia et al.,[129] Bommarito et al.[130] and Protozanova et al.[131] which can be found summarized in a table[127] in their article. They range from $\Delta G^\circ(\gamma^0) = +1.9$ kcal/mol to $\Delta G^\circ(\gamma^1 0)$ strong $= -21.2$ kcal/mol.

The constant for the branch migration is:[127]

$$k_b = 1.0 \times \left(\frac{b}{b-m}\right)^2 \text{ s}^{-1}, \text{ or} \tag{2.31}$$

$$k_b = \frac{400}{(b-m)^2} \text{ s}^{-1}. \tag{2.32}$$

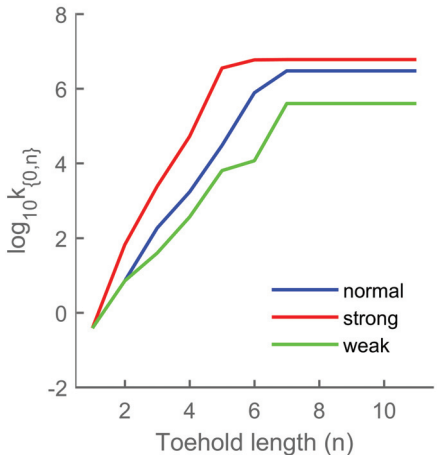

Figure 2.12: Forward rate constant of toehold-mediated strand displacement ($m = 0$) as a function of the toehold length n, as determined by the model of Zhang and Winfree.[127] The rate constant is calculated for intermediate, strong and weak toeholds and for a blocking region β of length $b = 20$. The value of b has minimal effect on the curves.

This three-step model is then used by Zhang and Winfree[127] to develop a bimolecular toehold exchange reaction model of the form:

$$\text{SB} + \text{T(m, n)} \underset{k_{(\gamma^n,\beta_m,\beta^m)}}{\overset{k_{(\beta^m,\beta_m,\gamma^n)}}{\rightleftharpoons}} \text{B} + \text{ST(m, n)},$$

and express the forward rate constant $k_{(\beta^m,\beta_m,\gamma^n)} \equiv k_{\{m,n\}}$ as

$$k_{\{m,n\}} \equiv \frac{k_{r(\beta^m)} k_f k_b}{k_{r(\gamma^n)} k_{r(\beta^m)} + k_{r(\gamma^n)} k_b + k_{r(\beta^m)} k_b}. \tag{2.33}$$

This bimolecular model simplifies the equations and allows for easier comparison with experimental data, but comes with some limitations. It is only valid for small concentrations of SB and T below a critical concentration.

In case of toehold-mediated strand displacement, $m = 0$, meaning B has no unique toehold with S strand. This means that $k_{r(\beta^0)} >> k_b$ and the forward rate constant $k_{\{0,n\}}$ in Equation (2.33) can be simplified.

As can be seen from Figure 2.12 the forward reaction rate constant $k_{\{0,n\}}$ in solution increases exponentially with toehold length until reaching a plateau at around a toehold length of 7 bases.

There is no data for how this is affected by the covalent linkage to the hydrogel network, but we know that the hybridization itself is somewhat slower inside a hydrogel than in solution, as discussed in section 2.2.4. This would affect the k_f constant, but whether there is an effect on the dissociation and branch migration constants is unknown.

Toehold-mediated strand displacement has been shown to take place with Morpholino oligonucleotides,[132] but its kinetics has not been studied. The differences between DNA and MOs of identical sequence suggest that the kinetics of strand displacement could differ for the two oligonucleotides. The higher melting temperature of Morpholinos could be expected to decrease the dissociation constant, while their lack of charge could lead to less destabilization by the dangling ends during the branch migration process. Furthermore, base stacking plays an important role in the thermodynamics of the branch migration[133] and MOs were reported to differ from DNA in this regard.

2.3 Size monitoring via interferometry

In the work described in this thesis, one of the methods to monitor the overall swelling of hydrogels was an interferometric readout setup. For this purpose, each hydrogel was prepared at the end face of an optical fiber, which was in turn connected to a light source and a detector. The nearly hemispherical hydrogel constitutes a Fabry-Perot cavity for measurement of the optical path length by using the interference of the light reflected at the fiber/hydrogel and hydrogel/solution interface.

The optical length l_{opt} of the hydrogel is a product of the physical length l of the hydrogel and its refractive index n and can be calculated from the frequency difference Δf between two neighbouring frequency peaks in the

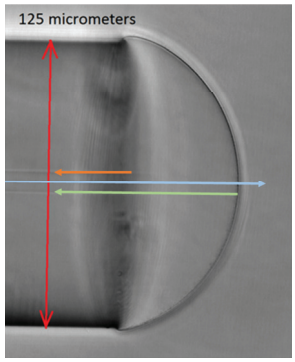

Figure 2.13: A hydrogel attached to the end face of an optical fiber as seen in a transmitted light microscopy image. The interferometer sends out a light wave (blue) which is then reflected at the fiber/hydrogel interface (orange) and at the hydrogel/solution interface (green). The interference wave of the two reflected waves is detected by the interferometer and used to calculate the optical length and the change in the optical length of the hydrogel cavity.

measured interference signal spectrum:

$$l_{opt} = l\,n = \frac{c}{2\Delta f}, \tag{2.34}$$

where c is the speed of light.

The change in the optical length Δl_{opt} can be measured using the change in phase $\Delta\varphi$ of the interference signal wave:

$$\Delta l_{opt} = \frac{\Delta\varphi\lambda_0}{4\pi}, \tag{2.35}$$

where λ_0 is the center wavelength of the light source, which has wavelengths in the range $\lambda \in [1530 - 1560]$ nm.

The parameter Δl_{opt} is the average change to the optical length, resulting from the change to the physical length l of the hydrogel, as well as change to the refractive index of the hydrogel n_{gel}, both brought on by the swelling:

$$\Delta l_{opt} = \int_0^{l_2} n_2(l)dl - \int_0^{l_1} n_1(l)dl, \tag{2.36}$$

where $n_i(l)$ is the optical index of the hydrogel at position l at times step i. By defining the average refractive index along the optical path as

$$\langle n_i \rangle = l_i^{-1} \int_0^{l_i} n_i(l) dl, \tag{2.37}$$

we can rewrite Equation (2.36) as

$$\Delta l_{opt} = \langle n_2 \rangle l_2 - \langle n_1 \rangle l_i \approx \langle n_1 \rangle \Delta l + l_1 \, \Delta n. \tag{2.38}$$

If Δn is sufficiently small, the change in the physical length is proportional to the change in the optical length.

2.4 Confocal laser scanning microscopy and fluorescent dyes

In order to determine the dynamics of the processes taking place in the hydrogel, a method to visualise them is necessary. Laser scanning microscopy taking advantage of fluorescent dyes was chosen as a tool to monitor the behavior of oligonucleotides within the hydrogels.

2.4.1 Fluorescence

Fluorescence is a process of light emission from certain substances after absorption of electromagnetic radiation (either visible light or ultraviolet). Molecules capable of fluorescence can be both natural and man-made, and are usually referred to as fluorophores, or fluorescent dyes in case of fluorophores that are added to other molecules.

The principle of fluorescence can be summarized by a Jablonski diagram (Figure 2.14). In the first step, an electron absorbs a photon and the molecule is excited from a ground state S_0 to its first excited singlet state S_1. The molecule then undergoes non-radiative vibrational relaxation, where some of the energy is dissipated as heat. Eventually, the molecule returns to its ground state via fluorescence, i.e. emission of a photon. The emit-

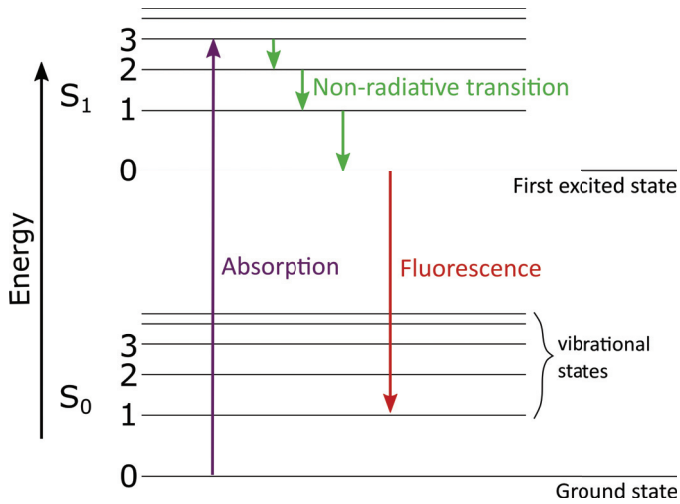

Figure 2.14: Jablonski diagram showing the generation of fluorescence emission.

ted photon can have energy up to that of the excitation photon, but usually lower. This means its wavelength is longer than that of the absorbed photon.

Molecules excited through absorption of photons can return to their ground state via other processes as well, which are not depicted in the Figure. If another fluorescent molecule is present, with excitation energy similar to the emission energy of the excited fluorophore and in sufficient proximity (up to $\approx$ 10 nm), the energy can be transferred non-radiatively to this second fluorophore, which then can undergo fluorescence. This phenomenon is called Förster resonance energy transfer (FRET).

The fluorophore can also relax to ground state through collisional quenching or intersystem crossing, so not all of the absorbed excitation light results in fluorescence.

A parameter called fluorescence quantum yield Φ quantifies the efficiency of the fluorescence:

$$\Phi = \frac{\#\text{ photons emitted}}{\#\text{ photons absorbed}}. \tag{2.39}$$

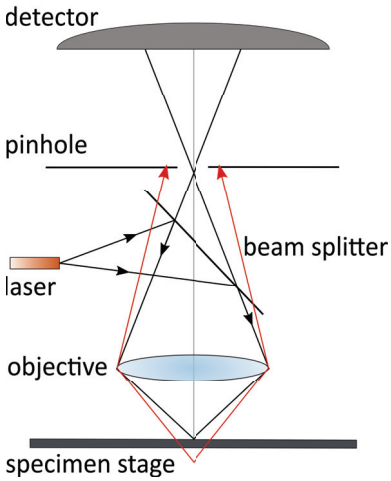

Figure 2.15: Principle of confocal microscopy. The specimen is illuminated via a laser, which leads to excitation of fluorophores in it. The fluorophores from the entire sample emit fluorescence, but only the light originating in the focal point passes the pinhole and is able to reach the detector.

2.4.2 Confocal laser scanning microscopy

Confocal laser scanning microscopy (CLSM) is an optical imaging technique, which uses a spatial pinhole to remove out-of-focus light. This improves image quality by reducing signal-to-noise ratio, compared to bright field microscopy and allows for optical sectioning, i.e. taking 2D images at different depths, to then be able to reconstruct the 3D image.[134]

In standard (fluorescence) microscopy the whole specimen is illuminated, so the whole specimen can (and does) emit fluorescence, which reaches the detector (or the ocular), if emitted in the right direction. The area that is within the focal point appears sharp in the image, but the rest of the specimen will be seen as a blurry background and add to the noise in the image. In CLSM (Figure 2.15), the excitation laser is focused onto a small area around the focal point by a lens, limiting the exposure of the rest of the sample to excitation. More importantly, the emitted fluorescence light has to pass through a pinhole – an aperture in a screen – that is placed in such a way that only light from the focus passes through, eliminating any

unfocused light, improving signal to noise ratio and leading to high spatial resolution both in the lateral (x-y) and axial (z) planes. It also allows for imaging deeper into the specimen than conventional microscopy. Each point in the specimen is imaged individually and the whole image is created by scanning over a regular raster pattern. This improves the image quality, allows for imaging at greater depths and for 3D reconstructed images of the sample.

2.4.3 Quantitative fluorescence microscopy

While ”seeing is believing”, just the existence of optical illusions should inspire us to be careful in interpreting what we are seeing. The work presented in this thesis required quantitative information on the fluorescently labelled target oligonucleotides within the hydrogels. Several aspects of CLSM need to be considered in order to extract quantitative data.

Optical aberrations are phenomena that lead to the distortion of the image. Most commonly, it is due to properties of the system itself (such as the lenses), that lead to blurring, defocusing or other distortion of the image. They affect the point spread function of the system (PSF), which is the image the system produces of a point source. Of interest to the work presented in this thesis is one aberration that has been well studied and that results from a mismatch in the refractive index along the axis of the objective, between the immersing solution and the sample.[135–141] The specimen appears to be at a different depth than it is and is distorted in the axial direction. There is also an associated loss of detected fluorescence with increasing depth.

Fluorescent molecules are crucial to the use of confocal laser scanning microscopy. The images, however, need to be interpreted by taking into account their properties as well as their effect on the properties of other molecules around them.

2.5 Reaction-diffusion model

One of the main goals in this thesis was to disentangle the coupled processes that were described in a previous section 2.2, in order to better understand how changing the different factors affects the resulting swelling equilibrium and swelling kinetics. The complex and interconnected nature of these underlying processes makes systematic investigation of the system challenging. However, the main steps leading to the swelling fall into the category of reaction-diffusion processes.

In general, reaction-diffusion refers to systems in which a diffusing species is also reacting with another species (usually immobilized, but not necessarily). The reactions can range from production, to catalysis, reversible or irreversible binding, degradation, etc. The overall net transport of the diffusing species through the system is a result of the reaction-diffusion process and can differ significantly from pure diffusion of the species in question. The diffusing molecule can exhibit a sharp advancing boundary between areas of high and low concentration and diffusional broadening can be completely suppressed. This has been observed in a variety of systems where (even transient) interactions occur between an invading molecule and a matrix with a limited number of interaction sites. This diffusion retardation has been reported for diffusing antibiotic in an alginate biofilm,[142] DNA hybridization in polyacrylamide gels,[143] autocatalysis of poly(D,L-lactic-co-glycolic acid) polymer microspheres,[144] antigen binding to an antibody immobilized in a nanofluidic channel,[145] DNA strand displacement reactions with all DNA strands being free in agarose gels,[146] or diffusion of small molecules into glassy polymers.[147]

2.5.1 Mathematical formulation of the model

In the case of oligonucleotide-polyacrylamide hydrogels which are the focus of the thesis, the target strand is diffusing within the aqueous phase of the hydrogel and simultaneously attaching to the network, more precisely to the toehold region of the sensing strands (with a reaction rate constant k^+). The

binding is followed by a branch point migration of the toehold-mediated strand displacement, which can be finished by an opening of the crosslink (k_b), or the target strand can be released back into the solvent and diffuse further (k^-):

$$\mathrm{SB} + \mathrm{T} \underset{k^-}{\overset{k^+}{\rightleftharpoons}} \mathrm{SBT} \xrightarrow{\mathrm{k}_b} \mathrm{ST} + \mathrm{B}$$

This process can be described by a two-step reaction-diffusion model. Some assumptions are made first to simplify the situation as a first approximation:

1. **The hydrogel does not swell.** This model describes the net transport of the target only and does not account for the swelling. This has several implications:

   (a) **The diffusion coefficient is constant.** In reality, the diffusion coefficient changes depending on the volume fraction of the hydrogel, so it would be larger in more swollen areas of the hydrogel.

   (b) **Hydrogel size does not change.** Due to swelling, the diffusing molecules travelling through the swollen part of the hydrogel have a longer path than those passing through unswollen parts. This difference is not taken into account.

   (c) **The binding site concentration is constant.** The swelling leads to a decrease in the concentration of the binding sites, i.e. SB duplexes attached to the network, which is not taken into account here.

2. **The partition coefficient is constant.** The partition coefficient changes both with the volume fraction, i.e. swelling, and due to solute interactions with the solvent. In this approximation, we assume that the swelling and the increased charge on the hydrogel due to binding of the target do not affect the partition coefficient.

3. **The presence of the fiber has no effect.** It is assumed that the nearly hemispherical hydrogel attached to the end face of an optical fiber behaves identically to a half of a free hydrogel sphere. Diffusing

molecules reaching the end face of the fiber and bouncing back would be equivalent to molecules diffusing from the other half of the (hypothetical) sphere. The presence of the fiber is assumed not to affect the strand displacement, diffusion and permeation constants.

The diffusion following Fick's second law (equation (2.16)) can be written for a radially symmetric sphere for a relative radial position $\hat{r} = r/R$ (r being the radial position and R the radius of the sphere)[144] as:

$$\frac{\partial c}{\partial t} = \frac{1}{\hat{r}^2}\frac{\partial}{\partial \hat{r}}\left(\hat{r}^2 \frac{D}{R^2}\frac{\partial c}{\partial \hat{r}}\right), \tag{2.40}$$

By introducing $\alpha = \frac{D}{R^2} > 0$ equation (2.40) can be rewritten as:

$$\frac{\partial c}{\partial t} = \frac{\alpha}{\hat{r}^2}\frac{\partial}{\partial \hat{r}}\left(\hat{r}^2 \frac{\partial c}{\partial \hat{r}}\right). \tag{2.41}$$

The reaction part is modeled as a two step process comprising of association/dissociation of T to S-B with rate constants k^+ and k^- and a subsequent dissociation of B from the complex (rate constant k_b): SB + T $\underset{k^-}{\overset{k^+}{\rightleftharpoons}}$ SBT $\xrightarrow{\mathrm{k}_b}$ ST + B

The spatio-temporal evolution of the target concentration can then be described by the following partial differential equations (PDEs):

$$\frac{\partial c}{\partial t} = \frac{\alpha}{\hat{r}^2}\frac{\partial}{\partial \hat{r}}\left(\hat{r}^2 \frac{\partial c}{\partial \hat{r}}\right) - k^+ c m_f + k^- m_c, \tag{2.42}$$

$$\frac{\partial m_c}{\partial t} = k^+ c m_f - k^- m_c - k_b m_c, \tag{2.43}$$

$$\frac{\partial m_o}{\partial t} = k_b m_c, \tag{2.44}$$

$$m_t = m_f + m_c + m_o, \tag{2.45}$$

where m_t is the total molar concentration of binding cites, m_f is the molar concentration of free binding sites, m_c the molar concentration of three-strand complexes and m_o of the open crosslinks. Equation (2.45) is a conservation equation for the total molar concentration of sites m_t.

By expressing m_f as a function of m_c, m_o and m_t in equations (2.42), (2.43) and (2.44) (using equation (2.45)) a set of three equations (for c and m_c and m_o) with their corresponding boundary and initial conditions is obtained:

$$\frac{\partial c}{\partial t} = \frac{\alpha}{\hat{r}^2}\frac{\partial}{\partial \hat{r}}\left(\hat{r}^2\frac{\partial c}{\partial \hat{r}}\right) - k^+cm_t + k^+cm_c + k^+cm_o + k^-m_c \tag{2.46a}$$

$$B.C.: \frac{\partial c(0,t)}{\partial \hat{r}} = 0, \quad t \geq 0 \tag{2.46b}$$

$$c(1,t) = c_{out}, \quad t \geq 0 \tag{2.46c}$$

$$I.C.: c(\hat{r},0) = \begin{cases} 0, & 0 \leq \hat{r} < 1 \\ c_{out}, & \hat{r} = 1 \end{cases} \tag{2.46d}$$

$$\frac{\partial m_c}{\partial t} = k^+cm_t - k^+cm_c - k^+cm_o - k^-m_c - k_bm_c \tag{2.47a}$$

$$B.C.: \frac{\partial m_c(0,t)}{\partial t} = 0 \tag{2.47b}$$

$$m_c(1,t) = 0 \tag{2.47c}$$

$$I.C.: m_c(\hat{r},0) = 0, \quad 0 \leq \hat{r} \leq 1 \tag{2.47d}$$

$$\frac{\partial m_o}{\partial t} = k_bm_c \tag{2.48a}$$

$$B.C.: \frac{\partial m_o(0,t)}{\partial t} = 0 \tag{2.48b}$$

$$m_o(1,t) = 0 \tag{2.48c}$$

$$I.C.: m_o(\hat{r},0) = 0, \quad 0 \leq \hat{r} \leq 1 \tag{2.48d}$$

where c_{out} is the concentration in the outside solution.

2.5.2 Numerical solution using Method of Lines

A possible numerical solution to this system of equations is by applying the Method of Lines. It relies discretizing one of the dimensions, in this case the spatial dimension $\hat{r}$ onto a finite equaly spaced grid and expressing the PDE as a set of ordinary differential equations (ODEs) for each of the spatial points.

The radial dimension is discretized as $\hat{r}_i = i\Delta\hat{r}$ for i=0,1,...,N, where $\Delta\hat{r}$ is the spacial step; and the concentrations c, m_c, m_o are discretized accordingly (c_i, m_{ci}, m_{oi}). The spatial derivatives are approximated by their second order centered finite difference in spherical coordinates[148] giving rise to a system of three ODEs for each spatial point i:

$$\frac{dc_i}{dt} = \begin{cases} \frac{6\alpha}{\Delta\hat{r}^2}(c_1 - c_0) - k^+c_0m_t + k^+c_0m_{c0} + k^+c_0m_{o0} + k^-m_{c0}, & \text{if } i = 0; \\ 0, & \text{if } i = N; \\ \frac{\alpha}{i\Delta\hat{r}^2}[(i+1)c_{i+1} - 2ic_i + (i-1)c_{i-1}] - \\ \qquad -k^+c_im_t + k^+c_im_{ci} + k^+c_im_{oi} + k^-m_{ci}, & \text{otherwise.} \end{cases} \tag{2.49a}$$

$$\frac{dc_{bi}}{dt} = k^+c_im_t - k^+c_im_{ci} - k^+c_im_{oi} - k^-m_{ci} - k_bm_{ci} \tag{2.49b}$$

$$\frac{dc_{oi}}{dt} = k_bm_{ci} \tag{2.49c}$$

This set of equations can be solved using MATLAB built in functions, such as *ode15s*.

Chapter 3

Summary and overall discussion

3.1 Summaries of papers

3.1.1 Paper I

Paper I is a review on the topic of DNA-hybrid hydrogels with sensing capability. The focus is solely on hydrogels that employ DNA in combination with another co-polymer and that have been suggested for use as sensors or have a sensing step in their application (such as environmentally-triggered release of loaded molecules).

The swelling theory of hydrogels is outlined, detailing the possible role of DNA in it, as well as how DNA's properties and higher order structure and the changes to it can be used to induce swelling changes in the hydrogel. The main mechanisms of recognition are hybridization (or binding), stem-loop changes and strand displacement reactions. A change from single to double-stranded DNA increases both the stiffness of the DNA structure and its charge. Both of these changes can induce swelling in the hydrogel. Similarly, displacement reactions lead to a change in charges attached to the hydrogel and a crosslink opening, facilitating swelling or even dissolu-

tion of the hydrogel. Stem-loop formation or opening can lead to a change in the length, stiffness and charge of the crosslink. In all of these cases, the DNA structure can form a crosslink (single or double-stranded), or can only be attached to the network by one end. Changes to DNA complexes forming a crosslink have generally bigger potential to affect the network. Among the possible targets are DNA and RNA strands, but also ions, small molecules, biomolecules and parts of bigger entities, such as viruses or bacteria. Aptamer-based recognition is widely used.

In case of sensors, which are the topic of this review, a readout method is integral to the system. Optically based principles are the most common, many using visual recognition for qualitative sensing purposes, but colloidal crystal arrays, surface plasmon resonance, diffraction gratings and interferometry have also been reported. Other methods include the use of quartz crystal microbalance, suspended micro-channel resonator and pedestal resonator.

In Paper I, a number of reported DNA-hybrid hydrogels with sensing capabilities is discussed, detailing their recognition mechanisms, readout methods, analytes, and sensitivity.

3.1.2 Paper II

In Paper II, the focus was on finding a method to extract concentration data from fluorescence intensity measured by CLSM in samples with abrupt lateral refractive index change. This unique challenge was due to the presence of the optical fiber to which our model hydrogels were attached and which is integral to the interferometric size readout. However, this problem is not limited to the case of optical fibers being present in the sample, but also affects microscopy within microfluidic channels or in the vicinity of glass walls and beads.

The presence of objects with refractive index significantly differing from that of the sample of interest leads to diffraction of both the excitation and emission light and distortion of the point spread function of the imaging system. This is then manifested in the image as a loss of fluorescence intensity that gives the impression of lower fluorophore concentration in the vicinity of the disruptive element (fiber, PDMS wall, etc). The effect is more pronounce the closer to the object and the deeper into the solution the imaging is performed, as larger and larger fractions of the light are being refracted. At depth $60\ \mu$m in an aqueous solution in the proximity of a glass cuboid, the aberration in the form of reduced detected fluorescence intensity reaches $\approx 70\ \mu$m from the cuboid solution interface and the intensity close to this interface is reduced to one-third of the not aberrant intensity.

In the Paper, the origin of this phenomenon was discussed, as well as a simple method of estimating the extent of the intensity loss (both in terms of how far from the object it reaches and how much intensity is lost) from ray optics-based calculation of the unaffected light cone fraction. The point spread function is also imaged for beads far and close to a fiber, showing large distortions and loss of intensity in the fiber proximity. Intensity profiles for glass and PDMS cuboids and glass fibers are recorded at various depths and compared, showing dependence on the imaging depth, object geometry and refractive index. Lastly, a correction method is suggested and tested, using a reference profile obtained by imaging the refractive object in a solution of homogeneous fluorophore concentration and either smoothing the curve or fitting it to a Gaussian. The sample intensity profiles then

can be scaled by dividing with the reference profile, to provide the corrected concentration profiles.

Some limitations of the procedure arise from the necessity to accurately align the sample and reference profiles, as small shifts can result in large changes, especially at the edge of the refractive object. In the ideal case, the same object is used for its own reference, limiting the effect of small differences in the shape of different objects, but a satisfactory correction can be achieved even by using a different reference object of the same general shape and same refractive index as the sample.

3.1.3 Paper III

In Paper III, we have explored the effect of the toehold length on the reaction-diffusion of target DNA within DNA-responsive hydrogels. The hydrogels in question are dual-crosslinked DNA-co-polyacrylamide hydrogels with added dsDNA crosslinks which can be opened by a target DNA strand complementary to one of the crosslink strands. The binding of the target to the sensing strand is facilitated by the presence of a toehold – a complementary region on target and sensing strand not blocked by the other crosslink strand – the blocking strand.

The aim of this study was to gain more understanding about the processes that take place in the hydrogel, from the diffusion of the target through the network, its initial binding, which is followed by a branch migration process of the toehold-mediated strand displacement and finally the crosslink opening.

Quasi-hemispherical hydrogels were prepared at the end of optical fibers to support the interferometric size monitoring which is the basis of their potential sensor application. The interferometer provides highly accurate information on the changes to the overall optical length brought on by the swelling, but does not provide any insight into the underlying mechanisms. For this reason, we have employed fluorescent labelling and confocal laser scanning microscopy to observe the individual processes. We have also designed three different target sequences, a target T3 with a toehold of 3 bases and a target T7 with a toehold of 7 bases, in order to explore the effect of the length of the toehold on the hydrogel response, as well as a target T0, that does not bind to the network and serves as a control. The targets were fluorescently labelled, in order to monitor their concentration throughout the hydrogel. This concentration would correspond to that of the free targets, together with the targets bound to the network DNA. We have developed a method to extract fluorescence intensity profiles along the hydrogel axis from the CLSM micrographs and turn them into concentration profiles, accounting for the optical aberration caused by the presence of the fiber.

Concentration profiles of non-binding target T0 revealed strong depen-

dence of the equilibrium partitioning of the target on the presence of DNA within the hydrogel. Most likely due to the high charge density of DNA molecules, the target T0 was being excluded from the hydrogel to a larger degree than from a pure polyacrylamide hydrogel of the same crosslink density. The presence of fluorescent dyes on the DNA or the acrylamide also led to further reduction in partitioning, whether through effects on electrostatic, hydrophobic or size-related interactions.

The swelling kinetics was measured via interferometry and showed a toehold-dependent difference in the initial swelling rate. This difference, however, was dependent on the presence or absence of fluorescent dyes attached to the hydrogel-DNA. The swelling rate for T7 was generally faster than that for T3 (up to 5 times faster), but large inter-hydrogel variability was observed. The swelling rate difference between the two toeholds (5-fold) also did not reflect the difference in their rate of toehold-mediated strand displacement in solution (T7 being $\approx 10^4$ times faster).

The reason for the large difference in the strand displacement rate not being manifested in the hydrogel was revealed by spatiotemporal concentration profiles of the binding targets acquired by CLSM. Targets T7, due to their low dissociation constant would bind at the edge of the hydrogel to the point of saturation, before they would penetrate further into the hydrogel, exhibiting a steep moving concentration front. On the other hand, targets T3 which have a high binding rate, but also a high dissociation rate would quickly diffuse far into the hydrogel in a series of binding and unbinding events and saturation was reached more evenly throughout the hydrogel. The limited volume available for binding to the target T7 makes up for its high strand displacement rate.

Finally, the data was fitted to a reaction-diffusion model assuming two steps in the strand-displacement process: binding and dissociation of the target to and from the toehold (rate constants k^+ and k^-, respectively) and branch migration ending with crosslink opening (k_b). Parameters obtained by fitting were diffusion coefficient, the rate constants and the concentration of the available targets, which were then compared to the estimates from literature.

3.1.4 Paper IV

In Paper IV, we used the same design of hydrogels as in Paper III, but exchanged DNA for Morpholino oligonucleotides, preparing polyacrylamide hydrogels with additional MO crosslinks. We explored the effect of the toehold length of the target MO (toeholds 2 and 10) on the swelling kinetics and on the transport of the target within the hydrogel. The Morpholino hydrogels were also compared to DNA hydrogels and DNA targets prepared using sequences identical to those of Morpholinos. The main difference between DNA and MOs in this context is the lack of charges to the Morpholino backbone.

The swelling rate of the hydrogels attached to optical fibers was measured by interferometric readout and the diffusion and binding of the targets was observed by CLSM. The partitioning of non-binding control targets T0 was also studied.

DNA non-binding targets DNA-T0 were excluded from the hydrogels to a larger extent than partitioning models based on pure size exclusion would suggest, primarily due to their highly charged nature. Electrostatic interactions between the hydrogel-bound and target DNA lower the targets partition coefficient. We also observed changes to the partitioning depending on the fluorescent dye attached to the target, suggesting that the interactions between the dye and the components of the hydrogel also play a role.

On the other hand, MO-T0 were seen to penetrate into MO hydrogels to a larger extent than expected from size exclusion models, with a partition coefficient of approximately 0.8 . Their uncharged backbone eliminates the possibility of electrostatic interactions, but introduces the potential for hydrophobic ones. It is plausible that hydrophobic interactions between MOs and polyacrylamide could lead to their higher concentrations within the hydrogels.

The equilibrium partitioning is expected to affect the kinetics of the target transport for binding targets. We observed faster kinetics for MOs than for DNA (in their respective hydrogels), but a reduced overall response, i.e. DNA hydrogels were swelling to a larger extent than corresponding MO hy-

drogels, albeit slower.

The swelling rate was dependent on the toehold length both for MOs and DNA, with T10 targets swelling faster and to a larger degree than T2 targets. The effective diffusion of the MO targets in MO hydrogels exhibited differences depending on the toehold, with T2 concentration increasing throughout the whole hydrogel, with minimal slope in the concentration profile, while T10 concentration profiles featured a sharp transition between a region of high concentration and low concentration, which was moving towards the center of the hydrogel virtually unchanged. This was again due to the strong binding of T10 to the network, as they are unlikely to detach after their first binding event and are thus captured by the network very quickly and fill up the available binding sites by saturating each consecutive layer of the hydrogel. T2 targets on the other hand move quickly into the hydrogel in a series of binding and unbinding events.

In case of DNA hydrogels, the concentration profiles showed unexpected increases in the concentration within parts that were expected to be saturated with the targets already, suggesting another mechanism taking place.

Lastly, we have used the MO-T10 concentration profiles to fit a reaction-diffusion model of the the target diffusion and binding, where binding consisted of two steps: binding-unbinding and irreversible crosslink opening. The fitting yielded results for the diffusion coefficient, reaction rate constants of the targets and the available binding sites concentration. The diffusion coefficient was reasonably close to the estimated one, but the reaction rate constants differed significantly from estimates valid for DNA, suggesting that toehold exchange kinetics of Morpholinos differs from that of DNA.

Morpholinos offer a possibility to exploit the base pairing properties of DNA while changing its other properties, such as charge density or stiffness, profoundly affecting the hydrogel response.

3.2 General discussion

The use of DNA as a recognition element within hydrogels has great potential not only for biosensing, but for other applications that have a sensing component as well, such as target drug delivery and release (whether in the body or in cell cultures), responsive tissue scaffolds, DNA machines and devices, etc. In recent years, the interest in DNA hydrogels have grown, as can also be seen from the large number of reported designs featured in Paper I and in the Background chapter of this thesis (2.1.2).

The response of the hydrogels, be it their swelling, deswelling, dissolution or a change in other mechanical or optical properties, depends strongly on the higher order structure of the embedded DNA and its interactions with target molecules. The DNA properties in turn can be designed through the sequence of the bases. Each application requires a unique response from the hydrogel, in terms of the response magnitude, timing and rate. While the DNA interactions are well studied in solution, less is known about how they are influenced by embedding DNA in a hydrogel and how each of the sequential processes that lead to the overall response is affected by the other ones. Furthermore, the existence of nucleic acid analogues, such as Morpholino oligonucleotides, provides means for further customization of the oligonucleotide properties beyond what can be achieved with DNA.

The aim of this thesis was to develop a method to monitor the coupled processes leading to the swelling of the model system of oligonucleotide-responsive oligonucleotide-co-polyacrylamide hydrogels and study these processes and their effect on each other.

Confocal laser scanning microscopy was chosen to monitor the target transport. Several challenges to using this for quantitative concentration measurements of target in hydrogel were encountered. The main one of these was the aberration that arises from the presence of the optical fiber to which the hydrogel is attached. Before we could gain quantitative concentration data from the CLSM micrographs, this aberration had to be accounted for. Paper II describes and quantifies this phenomenon and features a correcting procedure, which we have later used in Papers III and IV

to turn the recorded fluorescent intensity profiles into concentration profiles. The correcting procedure relies on using reference profiles acquired by imaging the refractive object in a homogeneous fluorescent solution and dividing the sample profiles by a normalized reference profile. In case of the hydrogels, the reference images were those of a fiber with a hydrogel imaged in a non-binding target T0. The correcting procedure was successfully used for all of the hydrogels in Papers III and IV.

With the ability to extract target concentration profiles from the micrographs, it was possible to observe its binding and accumulation within the hydrogel. Using DNA and Morpholino oligonucleotides (binding targets as well as non-binding controls) and varying the toehold, allowed for exploration of the effect of charges on the backbone – through DNA-MO comparison; and the effect of binding and unbinding kinetics through the length of the toehold.

3.2.1 Comparison of estimated and measured hydrogel and target parameters

For further discussion, the properties of the different hydrogels are summarized in table 3.1, both estimated and measured. Many of these are derived based on theory and equations introduced in secion 2.2. Hydrogels DNA III are hydrogels featured in Paper III. These hydrogels contained DNA crosslinks and were exposed to DNA targets. They differ in their oligonucleotide concentration, length of the blocking region, target length and toehold lengths from DNA hydrogels used in Paper IV (DNA IV), which were also exposed to DNA targets. In Paper IV, we have also reported on Morpholino hydrogels (MO IV), which were exposed to MO targets and which have otherwise the same concentrations and oligonucleotide sequences as DNA IV hydrogels.

All hydrogels were prepared with a constant pregel concentration of Aam and Bis: $c_{\text{Aam}} = 10$ wt% and $c_{\text{Bis}} = 0.6$ mol%. Oligonucleotides were added at $c_{\text{oligo}} = 0.2$ mol% or $c_{\text{oligo}} = 0.4$ mol%, adding to total crosslinker concentration of $c_{\text{cross}} = 0.8$ mol% or $c_{\text{cross}} = 1.0$ mol%. In terms of %T and

Table 3.1: Comparison of properties of hydrogels and corresponding target oligonucleotides from all papers. Both theoretical estimates and measured properties are given

	DNA III	DNA IV	MO IV
c_{Aam} (wt%)	10	10	10
c_{Bis} (mol%)	0.6	0.6	0.6
c_{oligo} (mol%)	0.2	0.4	0.4
c_{cross} (mol%)	0.8	1.0	1.0
%T equiv	10.2	10.2	10.2
%C equiv	1.7	2.1	2.1
blocking length (#bases)	10	14	14
target length (#bases)	18	25	25
φ_0	0.07	0.07	0.07
φ	0.06	0.06	0.06
pore radius (nm) (Stellwagen[91])	81	81	81
a_f (nm) (Williams[76])	0.8	0.8	0.8
a (nm) (Williams[76])	2	3	$3^?$
K_{size} (Ogston[93])	0.48	0.26	$<0.26^?$
D_0 (μm^{2}s^{-1}) (Stellwagen[94])	155	130	$<130^?$
D_g (μm^{2}s^{-1}) (Park[105])	36	21	$<21^?$
D_g (μm^{2}s^{-1}) (Brinkman[76])	39	21	$<21^?$
D_g (μm^{2}s^{-1}) (exp)	17 ± 8	-	10 ± 2
k^+ ($M^{-1}s^{-1}$) (Zhang & Winfree[127])	T3: $10^{6.8}$ T7: $10^{6.8}$	T2: $10^{6.5}$ T10: $10^{6.5}$	- -
k^+ ($M^{-1}s^{-1}$) (exp)	T3: $10^{(4.7\pm0.4)}$ T7: $10^{(4.5\pm0.1)}$	- -	- T10: $10^{(3.2\pm0.2)}$
k^- (s^{-1}) (Zhang & Winfree[127])	T3: $10^{2.3}$ T7: $10^{-5.2}$	T2: $10^{4.4}$ T10: $10^{-5.4}$	- -
k^- (s^{-1}) (exp)	T3: $10^{(2.1\pm0.3)}$ T7: $10^{(-5\pm1)}$	- -	- T10: 0.947 ± 0.06
k_b (s^{-1}) (Zhang & Winfree[127])	4	2	-
k_b (s^{-1}) (exp)	T3: 3.0 ± 0.7 T7: 1.5 ± 0.5	- -	- T10: 3.1 ± 0.4
binding site density (mM) (theor)	2	4	4
binding site density (mM) (exp)	0.2 ± 0.07	-	0.18 ± 0.03

$^?$ Signifies the estimates for Morpholino oligonucleotides based on DNA oligonucleotides of the same sequence.

%C equivalent to the total crosslinker fraction, this would be 10.2%T and 1.7%C for DNA III and 10.2%T and 2.1%C for DNA IV and MO IV, where %C expresses the total crosslinker (Bis + oligo) weight percentage.

To estimate the effective pore size of the hydrogels, we use the formula given by Stellwagen et al[91] (equation : (2.8)) for 2%C which is close for all of the hydrogels in question. With the value 10.2%T, the estimated apparent pore radius will then be 81 nm. Naturally, the actual distribution of the sizes will be much broader, with the existence of substantially larger as well as smaller pores.

The size contribution to the partitioning was calculated using the Ogston formula (2.14). Estimates of target strand radius, polyacrylamide chain radius and volume fraction of the hydrogel are needed. The target strand radius can be approximated by the radius of gyration of ssDNA[149] $a = 2$ nm for DNA III targets of 18 bases, and $a = 3$ nm for DNA IV targets of 25 bases. The size of MO IV targets (25 bases) can be expected to be slightly larger than that of corresponding DNA, since MOs are claimed to be stiffer than DNA.[132] The radius of the polyacrylamide chains has been previously reported as $a_f = 0.8$ nm.[76] The volume fraction of the hydrogels with 10 wt% Aam, where 0.7 ml of Aam weights 1 g,[74] is $\varphi_0 = 0.07$ in the pregel solution and $\varphi = 0.06$ after equilibration in buffer before the addition of the target. The calculation is based on the measured average size of the hydrogel as upon preparation, and after reached swelling equilibrium in buffer.

Taking these values into the Ogston formula suggest a partitioning contribution of: $K_{\text{size,conf}} = 0.48$, for DNA III and $K_{\text{size,conf}} = 0.26$ for DNA IV and possibly slightly less than 0.26 for MO IV.

In the presented hydrogels, size and conformation are not the only effects contributing to the target partitioning, but other interactions are present as well. In case of DNA, electrostatic interactions are likely to dominate and favour target exclusion from the hydrogel and for Morpholinos possible hydrophobic interactions are likely to increase their concentration in the hydrogel. In both cases, target strands complementary to the hydrogel-bound strands introduce biospecific interactions, which are of interest for the realization of sensing applications, as they lead to accumulation of the targets

in the hydrogel far beyond their concentration in the immersing solution.

The diffusion coefficients for the ssDNA targets of 18 and 25 nucleotides in solution according to Stellwagen et al.[94] (equation (2.18)) are:

$$D_{18} = 1.55 \times 10^{-6}\ \mathrm{cm^2 s^{-1}} = 155\ \mu\mathrm{m^2 s^{-1}} \tag{3.1}$$

and

$$D_{25} = 1.30 \times 10^{-6}\ \mathrm{cm^2 s^{-1}} = 130\ \mu\mathrm{m^2 s^{-1}}. \tag{3.2}$$

There is no known reference for diffusion coefficient of Morpholino oligonucleotides, but MO IV targets have the same length as DNA IV targets, and can be expected to behave similarly, although their larger stiffness is likely to make them larger and thus diffuse slower.

The diffusion coefficient in a gel D_g will be reduced compared to that in solution and several models predicting this reduction have been introduced in section 2.2.3.

The formula by Park[105] (equation (2.20)) requires the acrylamide concentration in g/mL which for our hydrogels swelling by 145% from 0.1 g/mL would be $C = 0.07$ g/mL. The diffusion coefficient is expected to be reduced to:

$$\left(\frac{D_g}{D_0}\right)_{\text{Park}} = 0.23, \text{ for } a = 2 \text{ nm}, \text{ for 18 bases long target in DNA III}, \tag{3.3a}$$

$$\left(\frac{D_g}{D_0}\right)_{\text{Park}} = 0.16, \text{ for } a = 3 \text{ nm}, \text{ for 25 bases long target in DNA IV}. \tag{3.3b}$$

Another model for reduction of diffusion coefficient in hydrogels – the Brinkman model (equation (2.21)) has been found to provide a good fit for polyacrylamide hydrogels.[76] This model requires the knowledge of the Darcy permeability of the matrix κ. It can be calculated using a formula obtained by Tong and Anderson[74] using the data of Tokita and Tanaka:[150] $\kappa = 2.64\,(\varphi_0)^{-1.42}$ Å^2, where φ_0 is the volume fraction of the monomer and the crosslinker in the pregel solution. Using 0.7 ml/g for acrylamide,[74] we find a value of $\kappa = 115$ Å^2.

The Brinkman model thus yields

$$\left(\frac{D_g}{D_0}\right)_{\text{Brinkman}} = 0.25, \text{ for } a = 2 \text{ nm}, \text{ for 18 bases long target in DNA III}, \tag{3.4a}$$

$$\left(\frac{D_g}{D_0}\right)_{\text{Brinkman}} = 0.16, \text{ for } a = 3 \text{ nm for 25 bases long target in DNA IV}. \tag{3.4b}$$

The diffusion coefficient of the single stranded DNA target can thus be expected to be reduced in the DNA III hydrogels to 23 – 25% of its value in solution, and to approximately 16% of the value in solution for DNA IV hydrogels. For Morpholinos, the reduction could be even larger due to their higher stiffness. It should also be noted that the crosslinking density does not enter either of the presented formulas in any other way then through the volume fraction of the hydrogel, which in the presented estimate was the same for all three types of the hydrogels.

Finally, the estimates of the rate constants k^+, k^- and k_b are from Zhang and Winfree[127] (see section 2.2.4), who provide rate constants for toehold exchange of DNA in solution. Targets T2 and T10 had toeholds with equal number of strong and weak base pairs and their binding energies were thus $\Delta G^\circ(\gamma^2) = -1.7$ kcal/mol and $\Delta G^\circ(\gamma^1 0) = -14.8$ kcal/mol, while targets T3 and T7 had strong toeholds with almost exclusively GC bonds and so their binding energies were $\Delta G^\circ(\gamma^3) = -5.0$ kcal/mol and $\Delta G^\circ(\gamma^7) = -15.1$ kcal/mol. The strength of the toehold affects the binding constant k^+, which is twice as large for T3 and T7 as for T2 and T10, as well as the dissociation constant k^- (equation (2.30)).

3.2.2 Insight into the coupled processes leading to hydrogel swelling

One of the main observations from Papers III and IV is the effect of the toehold length on the hydrogel swelling and the net transport of the target within. The swelling rate was seen to be higher for longer toeholds, but the difference was much less than the difference in the rate constants would suggest. This was due to the changes to the effective diffusion that resulted

from increased binding of the targets with long toeholds. While they were accumulating within the hydrogel much faster than the short toehold targets, the volume available to them for binding was increasing slowly, while short toeholds were binding throughout the hydrogel. The apparent diffusion was then a complex result dependent more on the reaction kinetics than on the diffusion coefficient of the targets.

Notably, the difference in swelling rates between the short and long toehold was significantly more pronounced for hydrogels in Paper IV, both DNA IV and MO IV, than DNA III. One of the reasons for this could be the fact that for DNA III the difference between toehold lengths was only 4 bases (T3 and T7), compared to the difference of 8 bases (T2 and T10) for MO IV and DNA IV. However, due to the toehold T7 being strong (in the sense used in section 2.2.4, as in predominantly composed of GC bases, in this case GC/AT=6/1), while T10 was of intermediate strength (GC/AT = 50/50), the associated constants for these toeholds were similar. As was also discussed previously (section 2.2.4), from toeholds of 7 bases and longer, the overall strand displacement rate reaches a plateau. On the other hand, the difference is much larger between T3 and T2, where the expected dissociation constant for T2 is larger by two orders of magnitude than that of T3. It is this difference that makes T2 hydrogels swell significantly slower than T3 hydrogels and accounts for the swelling rate differing more for DNA IV and MO IV than for DNA III.

Additionally, the oligonucleotide crosslink density for DNA IV and MO IV is twice that as for DNA III, but we have observed both MO IV and DNA III to reach similar maximum concentrations within the hydrogel, which corresponded to approximately 10% for DNA III and 5% for MO IV of the oligonucleotide duplex concentrations known from the hydrogel preparation. This would suggest that only a very limited number of oligonucleotide crosslinks is available for actual binding. DNA IV was seen to accumulate to similar levels as MO IV, but the experiments were not concluded until equilibrium and a steady rise in the maximum concentration within the hydrogel was observed, hinting to the possibility that more and more binding sites were being made available as the hydrogel was swelling. This phenomenon did not occur for DNA III, which could mean that there is

a threshold concentration of hydrogel-bound oligonucleotides above which any added crosslinks will be unavailable, whether due to physical or electrostatic constraints. In such a case, swelling would reduce the oligo-crosslink concentration and allow targets to bind to them.

The development of the two-step reaction diffusion model and its optimization with experimental data allowed us to extract some valuable parameters from the concentration profiles. It also highlighted the presence of other phenomena, which were less expected and which the model does not account for, such as the aberrant profiles of T7b in Paper III or what seems to be a gradual uncovering of binding sites in DNA IV. Nonetheless, the fitted values for DNA III correspond well with those predicted by literature for DNA strand displacement in solution, with the exception of the association constant which is two orders of magnitude lower than the prediction. The association constant k^+ reflects the kinetics of the hybridization process, and hybridization has been shown to be affected by the immobilization of DNA, whether on a hard surface or in a hydrogel (section 2.2.4). Within a hydrogel, a reduction in the melting temperature of the DNA duplex has been reported, which could be manifested here by a lower association constant. In any case, the available model for DNA strand displacement in solution was in good overall agreement with our measured values, especially when taking into account the possible effect of oligonucleotide immobilization. On the other hand, the rate constants predicted for DNA in solution (DNA IV) did not describe the behavior of Morpholinos of identical sequences within a hydrogel (MO IV), suggesting that the strand displacement kinetics and potentially its mechanism is significantly different between Morpholinos and DNA.

The diffusion coefficient of the targets extracted from the data was in both cases (DNA III and MO IV) about half of that estimated from literature. Since the data from CLSM actually reflect the behavior of only the labeled targets, it is possible that the fluorescent dye led to alteration of the target oligonucleotide properties. Fluorescent dyes attached to molecules of interest have been previously reported to affect both their adsorption kinetics and diffusion.[151]

We have observed the fluorescent dyes (ones attached to the network, namely coumarin and fluorescein) to affect the transport of the targets mostly through their effect on the partitioning (Paper III). Many have also been shown to stabilize DNA duplexes and affect their hybridization kinetics.[152] Some dyes can also change their properties depending on their surroundings, for example the quantum yield of fluorescein being dependent on whether it is bound to a single- or double-strand DNA.[153] All of these effects need to be carefully considered when planning and interpreting quantitative measurements relying on fluorescent labelling.

Both in Paper III and in Paper IV, taking into account the permeation, and more specifically partitioning of the non-binding target in the hydrogel, was found to be of importance. The equilibrium partitioning of the non-binding target reflects the ability of the targets (both binding and not) to penetrate into the hydrogel and as a consequence the rate of the effective target diffusion. In our model, this came into play in the boundary conditions, namely the concentration of the target on the boundary. With targets exhibiting low partitioning, their effective concentration as experienced by the hydrogel can be significantly lowered compared to that in the surrounding solution and this has a similar effect on the reaction-diffusion kinetics as a lower diffusion coefficient would.[154] In sensing applications, this can potentially lead to an increase in the minimum target concentration necessary for detection.

The use of MOs allowed for further exploration of the partitioning effect on the spatiotemporal target concentration distribution. Due to their uncharged backbone and probably due to hydrophobic interactions, the partitioning coefficient of Morpholinos was much higher at 0.8 than that of DNA (0.1 – 0.3). As a result, the kinetics of the net target transport was much faster for MO IV than DNA IV. But while the Morpholinos reached their equilibrium faster and had similar maximum concentrations of targets inside the hydrogels as DNA IV, their swelling response was less pronounced. This can be again explained by their uncharged backbone. While the action of DNA targets in DNA IV leads to hydrogel swelling through two mechanisms: changes to the elastic term of the osmotic pressure through crosslink opening, and changes to the ionic term through the influx of charged targets

into the network; MO targets only affect the elastic contribution and thus lead to less total swelling. Despite Morpholino oligonucleotides possessing the same nucleobases as DNA, their behavior in this model system differs significantly, due to their different backbone. This allows for further customization of the hydrogel properties. However, for MOs to be used to the same degree as DNA, progress would have to be made towards preparation of MO aptamers.

Another important aspect of the hydrogels, which was manifested in both papers, were the (at times very large) differences between the individual hydrogels. Parallel preparations of hydrogels, often prepared from the same solution on the same day, exhibited different target saturation levels, different swelling rates and different relative swelling equilibrium volumes. A likely cause of these differences between the hydrogels is the underlying heterogeneity of polyacrylamide networks (as discussed in 2.2.2) and by extension DNA-polyacrylamide networks. Inhomogeneities in the form of dense nanogels linked by sparse network can be expected at the order of tens to hundreds of nanometers, but inhomogeneities at a larger scale, hundreds of micrometers, have also been experimentally observed. Since our hydrogels have a radius of approximately 100 μm, such differences would be manifested as differences between individual hydrogels. Notably, even with these differences, when fitted to the model, these experimental data led to fairly consistent estimates of diffusion coefficient, as well as reaction rate constants, as long as the concentration of the binding sites was treated as a variable parameter.

3.2.3 Implications beyond our model system

The system investigated here presents only one of many possible oligonucleotide-based hydrogel designs. A large variety of hydrogels have been reported, many of which can be categorized in one of the categories depicted in Figure 3.1. The response can be based on ds hybridization (a, b), stem-loop changes (c, d) or strand displacement (g, h). Variations of strand displacement (l, m, n) and stem-loop changes (e, f) can also be realised with an aptamer-biomolecule pair. Another possibility is presented by employing

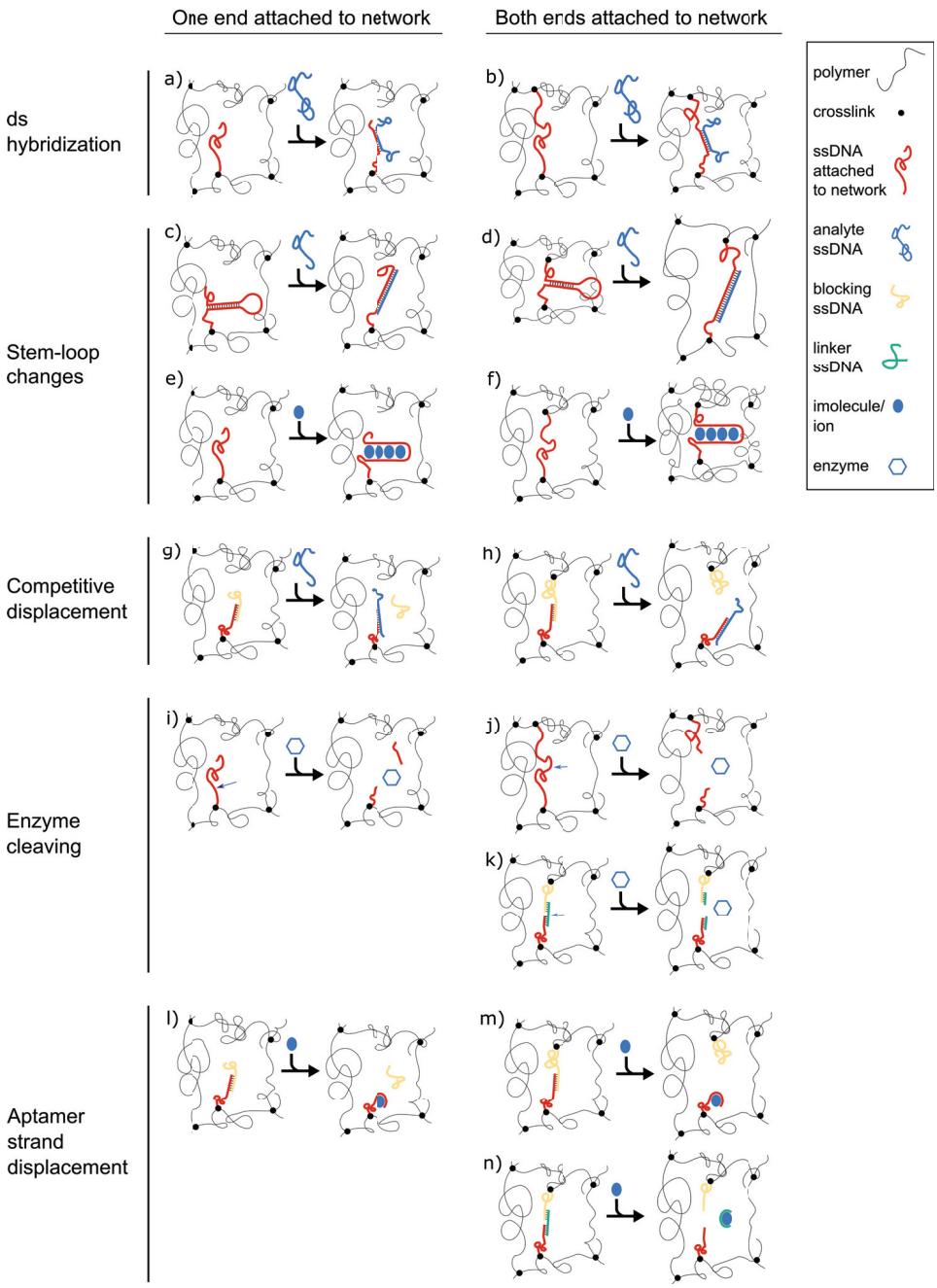

Figure 3.1: Schematic depiction of some of the most common hydrogel designs. Adapted and extended from Paper I.[155]

an enzyme catalysing a reaction within the hydrogel (i, j, k). Such hydrogels were recently reported by English and colleagues:[156] a CRISPR-Cas12a enzyme cuts the hydrogel-bound DNA, which leads to various hydrogel responses from release of biomolecules to hydrogel dissolution, depending on the underlying molecular design. The hydrogel's mode of action can also be based on a series of any of these mechanism, such as hydrogels by Cangialosi and colleagues[157] that swell through a series of DNA hairpin monomers attaching to one another and to a dsDNA crosslink in a hydrogel, thus extending the crosslink to several times its original length, or the hydrogels prepared by Lai et al.,[49] in which binding of a biomolecule releases a DNA trigger strands which then binds elsewhere in the hydrogel to release the molecular cargo.

Strand displacement is a commonly exploited mechanism in many of the reported hydrogels and as we have seen throughout this thesis, the inclusion of oligonucleotides within a hydrogel has profound, non-trivial effects on the kinetics of the process. While the kinetics of toehold exchange is well studied in solution, little to no data is available for the case of hydrogel-integrated DNA. While this work is far from comprehensive, it offers a case-study employing one of the simplest possible designs featuring a strand displacement reaction. This system can also serve as a model system for other reaction-diffusion based systems, which all of the hydrogel designs presented in Figure 3.1 could be considered as, but can also be extended to other reaction-(advection)-diffusion situations, such as adsorption of diffusing species in nanochannels. In one such system, similar moving concentration wavefronts and a slowing of effective diffusion of antigens in antibody-covered nanochannels was reported.[145] In this regard, hydrogels involving strand displacement can serve as model systems with highly customizable parameters, from diffusion (controlled through hydrogel volume fraction) to reaction kinetics (controlled through toehold length).

The application of reaction-diffusion modelling was also shown as a valuable tool to gain more quantitative understanding of the system and its underlying processes as well as revealing situations when mechanisms beyond pure diffusion and reaction are involved.

Chapter 4

Conclusions and outlook

The aim of this thesis was to disentangle the coupled processes leading to swelling of oligonucleotide-based hydrogels that were chosen as a model system. Such an endeavour is rarely reported in the literature, as most DNA hydrogels are introduced as proof-of-concept. However, the knowledge of the underlying mechanisms and the ability to predict the behavior of these hydrogels could be the missing link that is preventing more of the hydrogels being used commercially.

As we have shown in this thesis, even in a relatively simple DNA hydrogel, the cascade of the underlying processes and their interactions are complex. Their study is further complicated by our inability to directly observe the events at the molecular level. Microscopy using fluorescent dyes is a powerful and valuable tool, but as we have seen, it poses its own challenges. In our case, it was the presence of the fiber and the resulting aberration, but also the fact that the attachment of fluorescent dyes to molecules of interest alters their behavior. In an almost quantum-mechanical way, we cannot see without affecting the system.

The reaction-diffusion modeling proved to be a powerful tool in this case, as it allowed us to extract valuable molecular and hydrogel parameters from the concentration profiles, which were shown to be more consistent than the inter-hydrogel variability would suggest. This suggests that

the model can be useful in the reverse situation as well: to use it to predict the behavior of a hydrogel based on its known properties and the known properties of featured oligonucleotides.

Most commercially available hydrogels nowadays are not of the responsive kind, but simply hydrogels deriving their function from their structural properties and the ability to hold water. The number of reported responsive hydrogel systems, and especially those DNA-based, has been increasing in the recent years, but most could be classified as proof-of-concept. While it is difficult to predict the future of the responsive hydrogels, I can voice my thoughts on some of the challenges I believe this field faces. One of them lies in the inhomogeneity of many polymer networks (such as polyacrylamide) and the resulting large inter-hydrogel variability of the response. A possible way to address this issue would be through use of more regular networks, such as regular polyethylene glycol molecules with several reactive arms,[158,159] or materials made purely of DNA, which provides more control over the hydrogel structure than most co-polymers.[160–162]

Furthermore, the high cost of custom DNA can make many of the applications unprofitable, although this cost has been decreasing. Another challenge, especially for sensing applications, lies in the need for reliable, high-precision, low-threshold readout methods allowing for quantitative concentration measurements of the target. This is again complicated by high variability, as it requires each sensor to be calibrated, increasing their cost.

Lastly, we need a better understanding of the mechanisms taking place within responsive hydrogels, to be able to efficiently design them, tune them to the desired application and correctly evaluate their response behavior.

Bibliography

[1] Otto Wichterle and Drahoslav Lím. Hydrophilic Gels for Biological Use. *Nature*, 185:117–118, 1960.

[2] Enrica Caló and Vitaliy V. Khutoryanskiy. Biomedical applications of hydrogels: A review of patents and commercial products. *European Polymer Journal*, 65:252–267, 2015.

[3] John A. Pelesko. *Self-assembly: the science of things that put themselves together*. Chapman & Hall/CRC, New York, 2007.

[4] Faisal A. Aldaye, Alison L. Palmer, and Hanadi F. Sleiman. Assembling materials with DNA as the guide. *Science*, 321(5897):1795–1799, 2008.

[5] Nadrian C. Seeman. DNA in a material world. *Nature*, 421:427–431, 2003.

[6] Young Hoon Roh, Roanna C.H. Ruiz, Songming Peng, Jong Bum Lee, and Dan Luo. Engineering DNA-based functional materials. *Chem. Soc. Rev.*, 40(12):5730–5744, 2011.

[7] Shihui H Li, Niancao A C Chen, Erin R. Gaddes, Xiaolong L Zhang, Cheng Dong, and Yong Wang. A Drosera-bioinspired hydrogel for catching and killing cancer cells. *Scientific Reports*, 5(12):1–12, 2015.

[8] Ebbe S. Andersen, Mingdong Dong, Morten M. Nielsen, Kasper Jahn, Ramesh Subramani, Wael Mamdouh, Monika M. Golas, Bjo-

ern Sander, Holger Stark, Cristiano L. P. Oliveira, Jan Skov Pedersen, Victoria Birkedal, Flemming Besenbacher, Kurt V. Gothelf, and Jørgen Kjems. Self-assembly of a nanoscale DNA box with a controllable lid. *Nature*, 459:73–76, 2009.

[9] Abdul M. Mohammed, Petr Šulc, John Zenk, and Rebecca Schulman. Self-assembling DNA nanotubes to connect molecular landmarks. *Nature Nanotechnology*, 12(4):312–316, 2017.

[10] Fei Zhang, Jeanette Nangreave, Yan Liu, and Hao Yan. Structural DNA nanotechnology: State of the art and future perspective. *Journal of the American Chemical Society*, 136(32):11198–11211, 8 2014.

[11] Paul W. K. Rothemund. Folding DNA to create nanoscale shapes and patterns. *Nature*, 440:297–302, 2006.

[12] A. Paul Alivisatos, Kai P. Johnsson, Xiaogang Peng, Troy E. Wilson, Colin J. Loweth, Marcel P. Bruchez, and Peter G. Schultz. Organization of 'nanocrystal molecules' using DNA. *Nature*, 382:609–611, 1996.

[13] Seema Singh, Anshul Mishra, Rina Kumari, Kislay K. Sinha, Manoj K. Singh, and Prolay Das. Carbon dots assisted formation of DNA hydrogel for sustained release of drug. *Carbon*, 114:169–176, 2017.

[14] Bernard Yurke, Andrew J. Turberfield, Allen P. Mills, Friedrich C. Simmel, and Jennifer L. Neumann. A DNA-fuelled molecular machine made of DNA. *Nature*, 406:605–608, 2000.

[15] Yukiko Kamiya and Hiroyuki Asanuma. Light-Driven DNA Nanomachine with a Photoresponsive Molecular Engine. *Accounts of Chemical Research*, 47(6):1663–1672, 2014.

[16] Hao Yan, Xiaoping Zhang, Zhiyong Shen, and Nadrian C Seeman. A robust DNA mechanical device controlled by hybridization topology. *Nature*, 415:62–65, 2002.

[17] Joshua Fern, Dominic Scalise, Angelo Cangialosi, Dylan Howie, Leo Potters, and Rebecca Schulman. DNA Strand-Displacement Timer Circuits. *ACS Synthetic Biology*, 6(2):190–193, 2017.

[18] Ravinderjit S. Braich, Cliff Johnson, Paul W. K. Rothemund, Darryl Hwang, Nickolas Chelyapov, and Leonard M. Adleman. Solution of a satisfiability problem on a gel-based DNA computer. In Anne Condon and Grzegorz Rozenberg, editors, *DNA Computing. DNA 2000*, pages 27–42, Berlin, Heidelberg, 2001. Springer.

[19] Giovanna Sicilia, Christine Grainger-Boultby, Nora Francini, Johannes P. Magnusson, Aram O. Saeed, Francisco Fernández-Trillo, Sebastian G. Spain, Cameron Alexander, Francisco Fernandez-Trillo, Sebastian G. Spain, and Cameron Alexander. Programmable polymer-DNA hydrogels with dual input and multiscale responses. *Biomaterials Science*, 2:203–211, 2014.

[20] P. E. Nielsen, M. Egholm, R. H. Berg, and O. Buchardt. Sequence-selective recognition of DNA by strand displacement with a thymine-substituted polyamide. *Science*, 254(5037):1497–1500, 1991.

[21] James Summerton and Dwight Weller. Morpholino antisense oligomers: Design, preparation, and properties. *Antisense and Nucleic Acid Drug Development*, 7(3):187–195, 1997.

[22] Satoshi Obika, Daishu Nanbu, Yoshiyuki Hari, Ken-ichiro Morio, Yasuko In, Toshimasa Ishida, and Takeshi Imanishi. Synthesis of 2'-O,4'-C-methyleneuridine and -cytidine. Novel bicyclic nucleosides having a fixed C3, -endo sugar puckering. *Tetrahedron Letters*, 38(50):8735–8738, 1997.

[23] Nasuo Ueda, Toshio Kawabata, and Kiichi Takemoto. Synthesis of N-(2,3-dihydroxypropyl) derivatives of nucleic bases. *Journal of Heterocyclic Chemistry*, 8(5):827–829, 1971.

[24] A. Eschenmoser. Chemical etiology of nucleic acid structure. *Science (New York, N.Y.)*, 284(5423):2118–2124, 1999.

[25] Elias Quijano, Raman Bahal, Adele Ricciardi, W. Mark Saltzman, and Peter M. Glazer. Therapeutic Peptide Nucleic Acids: Principles, Limitations, and Opportunities. *The Yale journal of biology and medicine*, 90(4):583–598, 2017.

[26] Nadia Zaffaroni, Raffaella Villa, and Marco Folini. Therapeutic Uses of Peptide Nucleic Acids (PNA) in Oncology. In *Peptide Nucleic Acids, Morpholinos and Related Antisense Biomolecules*, pages 171–180. Springer US, Boston, MA, 2006.

[27] Virendra N. Pandey, Alok Upadhyay, and Binay Chaubey. Prospects for antisense peptide nucleic acid (PNA) therapies for HIV. *Expert opinion on biological therapy*, 9(8):975–989, 2009.

[28] Alicia D. D'Souza, Boris P. Belotserkovskii, and Philip C. Hanawalt. A novel mode for transcription inhibition mediated by PNA- induced R-loops with a model in vitro system. *Biochimica et Biophysica Acta*, 1861(2):158–166, 2018.

[29] Derek S. Lundberg, Scott Yourstone, Piotr Mieczkowski, Corbin D. Jones, and Jeffery L. Dangl. Practical innovations for high-throughput amplicon sequencing. *Nature Methods*, 10(10):999–1002, 2013.

[30] Arghya Ray and Bengt Norden. Peptide nucleic acid (PNA): its medical and biotechnical applications and promise for the future. *FASEB journal*, 14(9):1041–1060, 2000.

[31] David R. Corey and John M. Abrams. Morpholino antisense oligonucleotides: tools for investigating vertebrate development. *Genome biology*, 2(5):1–1015, 2001.

[32] Waldemar Popik, Atanu Khatua, James E K Hildreth, Benjamin Lee, and Donald J Alcendor. Phosphorodiamidate morpholino targeting the 5' untranslated region of the ZIKV RNA inhibits virus replication. *Virology*, 519:77–85, 2018.

[33] Jason K. H. Lai, Kristina K. Gagalova, Carsten Kuenne, Mohamed A. El-Brolosy, and Didier Y. R. Stainier. Induction of interferon-stimulated genes and cellular stress pathways by morpholinos in zebrafish. *Developmental Biology*, 454(1):21–28, 2019.

[34] Richard Owczarzy, Yong You, Christopher L Groth, and Andrey V Tataurov. Stability and mismatch discrimination of locked nucleic acid-DNA duplexes. *Biochemistry*, 50(43):9352–9367, 2011.

[35] Michael Petersen and Jesper Wengel. LNA: a versatile tool for therapeutics and genomics. *Trends in Biotechnology*, 21(2):74–81, 2003.

[36] Lilu Zhang, Adam Peritz, and Eric Meggers. A Simple Glycol Nucleic Acid. *Journal of the American Chemical Society*, 127(12):4174–4175, 2005.

[37] Eric Meggers and Lilu Zhang. Synthesis and Properties of the Simplified Nucleic Acid Glycol Nucleic Acid. *Accounts of Chemical Research*, 43(8):1092–1102, 2010.

[38] Andrew C. Larsen, Matthew R. Dunn, Andrew Hatch, Sujay P. Sau, Cody Youngbull, and John C. Chaput. A general strategy for expanding polymerase function by droplet microfluidics. *Nature Communications*, 7(1):11235, 2016.

[39] Hui Mei, Jen-Yu Liao, Randi M. Jimenez, Yajun Wang, Saikat Bala, Cailen McCloskey, Christopher Switzer, and John C. Chaput. Synthesis and Evolution of a Threose Nucleic Acid Aptamer Bearing 7-Deaza-7-Substituted Guanosine Residues. *Journal of the American Chemical Society*, 140(17):5706–5713, 2018.

[40] Alexandra E. Rangel, Zhe Chen, Tewoderos M. Ayele, and Jennifer M. Heemstra. In vitro selection of an XNA aptamer capable of small-molecule recognition. *Nucleic Acids Research*, 46(16):8057–8068, 2018.

[41] Nikolaos A. Peppas, J. Zach Hilt, Ali Khademhosseini, and Robert Langer. Hydrogels in Biology and Medicine: From Molecular Principles to Bionanotechnology. *Advanced Materials*, 18(11):1345–1360, 2006.

[42] Shuguang Zhang. Fabrication of novel biomaterials through molecular self-assembly. *Nature Biotechnology*, 21(10):156–1087, 2003.

[43] Miriam V. Flores-Merino, Somyot Chirasatitsin, Caterina LoPresti, Gwendolen C. Reilly, Giuseppe Battaglia, and Adam J. Engler. Nanoscopic mechanical anisotropy in hydrogel surfaces. *Soft Matter*, 6:4466–4470, 2010.

[44] Rein V. Ulijn, Nurguse Bibi, Vineetha Jayawarna, Paul D. Thornton, Simon J. Todd, Robert J. Mart, Andrew M. Smith, and Julie E. Gough. Bioresponsive hydrogels We highlight recent developments in hydrogel materials with biological. *Materials Today*, 10(4):40–48, 2007.

[45] Heiko J. Van Der Linden, Sebastiaan Herber, Wouter Olthuis, and Piet Bergveld. Stimulus-sensitive hydrogels and their applications in chemical (micro)analysis. *Analyst*, 128(4):325–331, 2003.

[46] Grant R. Hendrickson and L. Andrew Lyon. Bioresponsive hydrogels for sensing applications. *Soft Matter*, 5(1):29–35, 2009.

[47] Axel Habicht, Willi Schmolke, Frank Lange, Kay Saalwächter, and Sebastian Seiffert. The non-effect of polymer-network inhomogeneities in microgel volume phase transitions: Support for the mean-field perspective. *Macromolecular Chemistry and Physics*, 215(11):1116–1133, 2014.

[48] Mitsuhiro Shibayama and Toyoichi Tanaka. Volume phase transition and related phenomena of polymer gels. *Advances in Polymer Science*, 109, 1993.

[49] Jinping Lai, Shihui Li, Xuechen Shi, James Coyne, Nan Zhao, Fengping Dong, Yingwei Mao, and Yong Wang. Displacement and hybridization reactions in aptamer-functionalized hydrogels for biomimetic protein release and signal transduction. *Chemical Science*, 8(11):7306–7311, 2017.

[50] Dan Liu, Shasha Jia, Huimin Zhang, Yanli Ma, Zhichao Guan, Jiuxing Li, Zhi Zhu, Tianhai Ji, and Chaoyong James Yang. Integrating Target-Responsive Hydrogel with Pressuremeter Readout Enables

Simple, Sensitive, User-Friendly, Quantitative Point-of-Care Testing. *ACS Applied Materials and Interfaces*, 9(27):22252–22258, 2017.

[51] Wei Hai Chen, Wei Ching Liao, Yang Sung Sohn, Michael Fadeev, Alessandro Cecconello, Rachel Nechushtai, and Itamar Willner. Stimuli-Responsive Nucleic Acid-Based Polyacrylamide Hydrogel-Coated Metal–Organic Framework Nanoparticles for Controlled Drug Release. *Advanced Functional Materials*, 28:1–1705137, 2018.

[52] Juan Li, Cheng Zheng, Sena Cansiz, Cuichen Wu, Jiehua Xu, Cheng Cui, Yuan Liu, Weijia Hou, Yanyue Wang, Liqin Zhang, I. Ting Teng, Huang Hao Yang, and Weihong Tan. Self-assembly of DNA Nanohydrogels with Controllable Size and Stimuli-Responsive Property for Targeted Gene Regulation Therapy. *Journal of the American Chemical Society*, 137(4), 2015.

[53] Yishun Huang, Yanli Ma, Yahong Chen, Xuemeng Wu, Luting Fang, Zhi Zhu, and Chaoyong James Yang. Target-responsive DNAzyme cross-linked hydrogel for visual quantitative detection of lead. *Analytical Chemistry*, 86(22):11434–11439, 2014.

[54] Yishun Huang, Luting Fang, Zhi Zhu, Yanli Ma, Leiji Zhou, Xi Chen, Dunming Xu, and Chaoyong Yang. Design and synthesis of target-responsive hydrogel for portable visual quantitative detection of uranium with a microfluidic distance-based readout device. *Biosensors and Bioelectronics*, 85:496–502, 2016.

[55] Yanli Ma, Yu Mao, Yuan An, Tian Tian, Huimin Zhang, Jinmao Yan, Zhi Zhu, and Chaoyong James Yang. Target-responsive DNA hydrogel for non-enzymatic and visual detection of glucose. *Analyst*, 143:1679–1684, 2018.

[56] Xiaofeng Wei, Tian Tian, Shasha Jia, Zhi Zhu, Yanli Ma, Jianjun Sun, Zhenyu Lin, and Chaoyong James Yang. Target-responsive DNA hydrogel mediated stop-flow microfluidic paper-based analytic device for rapid, portable and visual detection of multiple targets. *Analytical Chemistry*, 87(8):4275–4282, 2015.

[57] Shuopeng Liu, Wenqiong Su, Yulong Li, Lulu Zhang, and Xianting Ding. Manufacturing of an electrochemical biosensing platform based on hybrid DNA hydrogel: Taking lung cancer-specific miR-21 as an example. *Biosensors and Bioelectronics*, 103:1–5, 2018.

[58] Xiaoxia Mao, Guifang Chen, Zihan Wang, Yuanguang Zhang, Xiaoli Zhu, and Genxi Li. Surface-immobilized and self-shaped DNA hydrogels and their application in biosensing. *Chemical Science*, 9(4):811–818, 2018.

[59] Wei Bai and David A Spivak. A Double-Imprinted Diffraction-Grating Sensor Based on a Virus-Responsive Super-Aptamer Hydrogel Derived from an Impure Extract. *Angewandte Chemie International Edition*, 53(8):2095–2098, 2014.

[60] Xiaoqi Wang and Xiaogong Wang. Aptamer-functionalized hydrogel diffraction gratings for the human thrombin detection. *Chemical Communications*, 49(53):5957–5959, 2013.

[61] Ling Yan, Zhi Zhu, Yuan Zou, Yishun Huang, Dewen Liu, Shasha Jia, Dunming Xu, Min Wu, Yu Zhou, Shuang Zhou, and Chaoyong James Yang. Target-Responsive "Sweet" Hydrogel with Glucometer Readout for Portable and Quantitative Detection of Non-Glucose Targets. *Journal of the American Chemical Society*, 135(10):3748–3751, 2013.

[62] Bao-Fen Ye, Yuan-Jin Zhao, Yao Cheng, Ting-Ting Li, Zhuo-Ying Xie, Xiang-Wei Zhao, and Zhong-Ze Gu. Colorimetric photonic hydrogel aptasensor for the screening of heavy metal ions. *Nanoscale*, 4(19):5998–6003, 2012.

[63] Yijie Wang, Yu Shao, Xiaozhou Ma, Bini Zhou, Alan Faulkner-Jones, Wenmiao Shu, and Dongsheng Liu. Constructing Tissuelike Complex Structures Using Cell-Laden DNA Hydrogel Bricks. *ACS Applied Materials and Interfaces*, 9(14):12311–12315, 2017.

[64] Zheng Zhang, Jie Du, Yuli Li, Jincai Wu, Feng Yu, and Yong Chen. An aptamer-patterned hydrogel for the controlled capture and release of

proteins: Via biorthogonal click chemistry and DNA hybridization. *Journal of Materials Chemistry B*, 5(30):5974–5982, 2017.

[65] Bernard Yurke, David C Lin, and Noshir A Langrana. Use of DNA Nanodevices in Modulating the Mechanical Properties of Polyacrylamide Gels. In Alessandra Carbone and NilesA Pierce, editors, *DNA Computing*, volume 3892 of *Lecture Notes in Computer Science*, pages 417–426. Springer Berlin Heidelberg, 2006.

[66] FrankXue Xue Jiang, Bernard Yurke, BonnieL L. Firestein, and NoshirA A. Langrana. Neurite Outgrowth on a DNA Crosslinked Hydrogel with Tunable Stiffnesses. *Annals of Biomedical Engineering*, 36(9):1565–1579, 2008.

[67] Michelle L. Previtera, Uday Chippada, Rene S. Schloss, Bernard Yurke, and Noshir A. Langrana. Mechanical Properties of DNA-Crosslinked Polyacrylamide Hydrogels with Increasing Crosslinker Density. *BioResearch Open Access*, 1(5):256–259, 2012.

[68] Bin-Cheng Yin, Bang-Ce Ye, Hui Wang, Zhi Zhu, and Weihong Tan. Colorimetric logic gates based on aptamer-crosslinked hydrogels. *Chemical Communications*, 48(9):1248–1250, 2012.

[69] Shunji Nagahara and Takehisa Matsuda. Hydrogel formation via hybridization of oligonucleotides derivatized in water-soluble vinyl polymers. *Polymer Gels and Networks*, 4(2):111–127, 1996.

[70] Sven Tierney, Sondre Volden, and Bjørn Torger Stokke. Glucose sensors based on a responsive gel incorporated as a Fabry-Perot cavity on a fiber-optic readout platform. *Biosensors and Bioelectronics*, 24(7):2034–2039, 2009.

[71] Ming Gao, Kamila Gawel, and Bjørn Torger Stokke. Toehold of ds-DNA exchange affects the hydrogel swelling kinetics of a polymer-dsDNA hybrid hydrogel. *Soft Matter*, 7(5):1741–1746, 2011.

[72] Paul J. Flory and John Rehner. Statistical mechanics of cross-linked polymer networks I. Rubberlike elasticity. *The Journal of Chemical Physics*, 11:512–520, 1943.

[73] Michael C. Koetting, Jonathan T. Peters, Stephanie D. Steichen, and Nicholas A. Peppas. Stimulus-responsive hydrogels: Theory, modern advances, and applications. *Materials Science and Engineering R*, 93:1–49, 2015.

[74] J Tong and J L Anderson. Partitioning and diffusion of proteins and linear polymers in polyacrylamide gels. *Biophysical Journal*, 70(3):1505–1513, 1996.

[75] Brian Amsden. Solute Diffusion within Hydrogels. Mechanisms and Models. *Macromolecules*, 31(23):8382–8395, 1998.

[76] James C. Williams Jr, Lawrence A. Mark, Susan Eichholtz, James C. Williams, Lawrence A. Mark, and Susan Eichholtz. Partition and Permeation of Dextran in Polyacrylamide Gel. *Biophysical Journal*, 75(1):493–502, 1998.

[77] Mitsuhiro Shibayama. Universality and specificity of polymer gels viewed by scattering methods. *Bulletin of the Chemical Society of Japan*, 79(12):1799–1819, 2006.

[78] Sebastian Seiffert. Scattering perspectives on nanostructural inhomogeneity in polymer network gels. *Progress in Polymer Science*, 66:1–21, 2017.

[79] Fany Di Lorenzo and Sebastian Seiffert. Nanostructural heterogeneity in polymer networks and gels. *Polymer Chemistry*, 6(31):5515–5528, 2015.

[80] A. Silberberg. Gel Structural Heterogeneity, Gel Permeability, and Mechanical Response. In Ronald S. Harland and Prud'homme Robert K., editors, *Polyelectrolyte Gels*, chapter 9, pages 146–158. American Chemical Society, 12 1992.

[81] Walter Chassé, Sandra Schlögl, Gisbert Riess, and Kay Saalwächter. Inhomogeneities and local chain stretching in partially swollen networks. *Soft Matter*, 9(29):6943–6954, 2013.

[82] Jacques Bastide and Ludwik Leibler. Large-Scale Heterogeneities in Randomly Cross-Linked Networks. *Macromolecules*, 21(8):2647–2649, 1988.

[83] Fany Di Lorenzo, Johannes Hellwig, Regine Von Klitzing, and Sebastian Seiffert. Macroscopic and Microscopic Elasticity of Heterogeneous Polymer Gels. *ACS Macro Letters*, 4(7):698–703, 2015.

[84] Reinhard Rüchel and Myles D. Brager. Scanning electron microscopic observations of polyacrylamide gels. *Analytical Biochemistry*, 68(2):415–428, 1975.

[85] Martin M. Chui, Ronald J. Phillips, and Michael J. McCarthy. Measurement of the porous microstructure of hydrogels by nuclear magnetic resonance. *Journal of Colloid And Interface Science*, 174(2):336–344, 1995.

[86] Anne-Marie Hecht, Robert Duplessix, and Erik Geissler. Structural Inhomogeneities in the Range 2.5-2500 Å in Polyacrylamide Gels. *Macromolecules*, 18(11):2167–2173, 1985.

[87] J. S. Fawcett and C. J.O.R. Morris. Molecular-Sieve Chromatography of Proteins on Granulated Polyacrylamide Gels. *Separation Science*, 1(1):9–26, 1966.

[88] Diana L. Holmes and Nancy C. Stellwagen. Estimation of polyacrylamide gel pore size from Ferguson plots of linear DNA fragments. II. Comparison of gels with different crosslinker concentrations, added agarose and added linear polyacrylamide. *Electrophoresis*, 12(9):612–619, 1991.

[89] Jacques G.H. Joosten, Erik T.F. Geladé, and Peter N Pusey. Dynamic light scattering by nonergodic media: Brownian particles trapped in polyacrylamide gels. *Physical Review A*, 42(4):2161–2175, 1990.

[90] Nancy C. Stellwagen. DNA mobility anomalies are determined primarily by polyacrylamide gel concentration, not gel pore size. *Electrophoresis*, 18(1):34–44, 1997.

[91] Nancy C. Stellwagen. Apparent pore size of polyacrylamide gels: Comparison of gels cast and run in Tris-acetate-EDTA and Tris-borate-EDTA buffers. *Electrophoresis*, 19(10):1542–1547, 1998.

[92] Stevin H. Gehrke, John P. Fisher, Maria Palasis, and Meghan E. Lund. Factors Determining Hydrogel Permeability. *Annals of the New York Academy of Sciences*, 831(1):179–184, 2006.

[93] Alexander G. Ogston. The spaces in a uniform random suspension of fibres. *Transactions of the Faraday Society*, 54(0):1754–1757, 1958.

[94] Earle Stellwagen, Yongjun Lu, and Nancy C. Stellwagen. Unified Description of Electrophoresis and Diffusion for DNA and Other Polyions. *Biochemistry*, 42(40):11745–11750, 2003.

[95] H. Yasuda, C. E. Lamaze, and L. D. Ikenberry. Permeability of solutes through hydrated polymer membranes. Part I. Diffusion of sodium chloride. *Die Makromolekulare Chemie*, 118(1):19–35, 1968.

[96] Steven R Lustig and Nikolaos A Peppas. Solute diffusion in swollen membranes. IX. Scaling laws for solute diffusion in gels. *Journal of Applied Polymer Science*, 36(4):735–747, 1988.

[97] R. I. Cukier. Diffusion of Brownian spheres in semidilute polymer solutions. *Macromolecules*, 17(2):252–255, 1984.

[98] R. J. Phillips, W. M. Deen, and J. F. Brady. Hindered transport of spherical macromolecules in fibrous membranes and gels. *AIChE Journal*, 35(11):1761–1769, 1989.

[99] Lennart Johansson and Jan-Erik Löfroth. Diffusion and interaction in gels and solutions. 4. Hard sphere Brownian dynamics simulations. *The Journal of Chemical Physics*, 98(9):7471–7479, 1993.

[100] D. A. H. Shyang Tsai and William Strieder. Effective conductivities of random fiber beds. *Chemical Engineering Communications*, 40(1-6):207–218, 1986.

[101] Brian Amsden. Solute diffusion in hydrogels. An examination of the retardation effect. *Polymer Gels and Networks*, 6(1):13–43, 1998.

[102] Brian Amsden. An Obstruction-Scaling Model for Diffusion in Homogeneous Hydrogels. *Macromolecules*, 32(3):874–879, 2 1999.

[103] Yuhang Zhou, Junjie Li, Ying Zhang, Dianyu Dong, Ershuai Zhang, Feng Ji, Zhihui Qin, Jun Yang, and Fanglian Yao. Establishment of a Physical Model for Solute Diffusion in Hydrogel: Understanding the Diffusion of Proteins in Poly(sulfobetaine methacrylate) Hydrogel. *The Journal of Physical Chemistry B*, 121(4):800–814, 2017.

[104] E. M. Johnson, D. A. Berk, R. K. Jain, and W. M. Deen. Hindered diffusion in agarose gels: test of effective medium model. *Biophysical journal*, 70(2):1017–1023, 1996.

[105] Il Hyun Park, Charles S. Jr. Johnson, and Don A Gabriel. Probe Diffusion in Polyacrylamide Gels As Observed by Means of Holographic Relaxation Methods: Search for a Universal Equation. *Macromolecules*, 21:1548–1553, 1990.

[106] Bryan A. Baker, Gita Mahmoudabadi, and Valeria Tohver Milam. Strand displacement in DNA-based materials systems. *Soft Matter*, 9:11160–11172, 2013.

[107] Luis P. Reynaldo, Alexander V. Vologodskii, Bruce P. Neri, and Victor I. Lyamichev. The kinetics of oligonucleotide replacements. *Journal of Molecular Biology*, 297(2):511–520, 2000.

[108] Philip N. Borer, Barbara Dengler, Ignacio Tinoco, and Olke C. Uhlenbeck. Stability of ribonucleic acid double-stranded helices. *Journal of Molecular Biology*, 86(4):843–853, 7 1974.

[109] J. C. Araque and M. A. Robert. Lattice model of oligonucleotide hybridization in solution. II. Specificity and cooperativity. *Journal of Chemical Physics*, 144(12):1–13, 2016.

[110] Moritz Julian Hoefert, Edward John Sambriski, and Juan José de Pablo. Molecular pathways in DNA-DNA hybridization of surface-bound oligonucleotides. *Soft Matter*, 7:560–566, 2011.

[111] Ian Y. Wong and Nicholas A. Melosh. An Electrostatic Model for DNA Surface Hybridization. *Biophysical Journal*, 98(12):2954–2963, 2010.

[112] Michael F. Hagan and Arup K. Chakraborty. Hybridization dynamics of surface immobilized DNA. *The Journal of Chemical Physics*, 120(10):4958–4968, 2004.

[113] Alexander W. Peterson, Richard J. Heaton, and Rosina M. Georgiadis. The effect of surface probe density on DNA hybridization. *Nucleic Acids Research*, 29(24):5163–5168, 2001.

[114] David Erickson, Dongqing Li, and Ulrich J. Krull. Modeling of DNA hybridization kinetics for spatially resolved biochips. *Analytical Biochemistry*, 317(2):186–200, 2003.

[115] Arnold Vainrub and B. Montgomery Pettitt. Accurate Prediction of Binding Thermodynamics for DNA on Surfaces. *The Journal of Physical Chemistry B*, 115(45):13300–13303, 2011.

[116] Alexander V. Fotin, Aleksei L. Drobyshev, Dmitri Y. Proudnikov, Alexander N. Perov, and Andrei D. Mirzabekov. Parallel thermodynamic analysis of duplexes on oligodeoxyribonucleotide microchips. *Nucleic Acids Research*, 26(6):1515–1521, 1998.

[117] Brian M. Frezza, Scott L. Cockroft, and M. Reza Ghadiri. Modular Multi-Level Circuits from Immobilized DNA-Based Logic Gates. *Journal of the American Chemical Society*, 129(48):14875–14879, 2007.

[118] Robert Penchovsky and Ronald R. Breaker. Computational design and experimental validation of oligonucleotide-sensing allosteric ribozymes. *Nature Biotechnology*, 23(11):1424–1433, 2005.

[119] Georg Seelig, David Soloveichik, David Yu Zhang, and Erik Winfree. Enzyme-free nucleic acid logic circuits. *Science*, 314(5805):1585–1588, 2006.

[120] Cheng Zhang, Jing Yang, and Jin Xu. Circular DNA Logic Gates with Strand Displacement. *Langmuir*, 26(3):1416–1419, 2010.

[121] S. J. Green, J. Bath, and A. J. Turberfield. Coordinated chemomechanical cycles: A mechanism for autonomous molecular motion. *Physical Review Letters*, 101(23):238101–1, 2008.

[122] Peng Yin, Harry M.T. Choi, Colby R. Calvert, and Niles A. Pierce. Programming biomolecular self-assembly pathways. *Nature*, 451(17):318–322, 2008.

[123] Joshua Fern and Rebecca Schulman. Design and Characterization of DNA Strand-Displacement Circuits in Serum-Supplemented Cell Medium. *ACS Synthetic Biology*, 6(9):1774–1783, 2017.

[124] David Yu Zhang, Andrew J. Turberfield, Bernard Yurke, and Erik Winfree. Engineering entropy-driven reactions and networks catalyzed by DNA. *Science*, 318(5853):1121–1125, 2007.

[125] Enjun Cheng, Yongzheng Xing, Ping Chen, Yang Yang, Yawei Sun, Dejian Zhou, Lijin Xu, Qinghua Fan, and Dongsheng Liu. A pH-Triggered, Fast-Responding DNA Hydrogel. *Angewandte Chemie*, 121(41):7796–7799, 2009.

[126] Lulu Qian, Erik Winfree, and Jehoshua Bruck. Neural network computation with DNA strand displacement cascades. *Nature*, 475(7356):368–372, 2011.

[127] David Yu Zhang and Erik Winfree. Control of DNA Strand Displacement Kinetics Using Toehold Exchange. *Journal of the American Chemical Society*, 131(47):17303–17314, 2009.

[128] Niranjan Srinivas, Thomas E. Ouldridge, Petr Šulc, Joseph M. Schaeffer, Bernard Yurke, Ard A. Louis, Jonathan P.K. Doye, and Erik Winfree. On the biophysics and kinetics of toehold-mediated DNA strand displacement. *Nucleic Acids Research*, 41(22):10641–10658, 2013.

[129] John SantaLucia and Donald Hicks. The thermodynamics of DNA structural motifs. *Annual Review of Biophysics and Biomolecular Structure*, 33:415–440, 2004.

[130] Salvatore Bommarito, Nicolas Peyret, and John Jr. SantaLucia. Thermodynamic parameters for DNA sequences with dangling ends. *Nucleic Acids Research*, 28(9):1929–1934, 2000.

[131] Ekaterina Protozanova, Peter Yakovchuk, and Maxim D. Frank-Kamenetskii. Stacked-unstacked equilibrium at the nick site of DNA. *Journal of Molecular Biology*, 342(3):775–785, 2004.

[132] Geraint J. Langford, Jaclyn Raeburn, David C. Ferrier, Philip J.W. Hands, and Michael P. Shaver. Morpholino Oligonucleotide Cross-Linked Hydrogels as Portable Optical Oligonucleotide Biosensors. *ACS Sensors*, 4(1):185–191, 2019.

[133] Rathi L Srinivas, Stephen C Chapin, and Patrick S Doyle. Aptamer-Functionalized Microgel Particles for Protein Detection. *Analytical Chemistry*, 83(23):9138–9145, 2011.

[134] James B. Pawley. *Handbook of biological confocal microscopy: Third edition*. Springer US, 2006.

[135] Alexander Egner and Stefan W Hell. Aberrations in Confocal and Multi-Photon Fluorescence Microscopy Induced by Refractive Index Mismatch. In James B Pawley, editor, *Handbook of Biological Confocal Microscopy*, chapter 20. Springer US, New York, third edit edition, 2006.

[136] S Hell, G Reiner, C Cremer, and E H K Stelzer. Aberrations in confocal fluorescence microscopy induced by mismatches in refractive index. *Journal of Microscopy*, 169(3):391–405, 1993.

[137] Ernst H. Keller. Objective Lenses for Confocal Microscopy. In James B Pawley, editor, *Handbook of Biological Confocal Microscopy*, chapter 7, pages 145–161. Springer US, New York, third edit edition, 2006.

[138] Michael J. Nasse and Jörg C. Woehl. Realistic modeling of the illumination point spread function in confocal scanning optical microscopy. *Journal of the Optical Society of America A*, 27(2):295–302, 2010.

[139] Alberto Diaspro, Federico Federici, and Mauro Robello. Influence of refractive-index mismatch in high-resolution three-dimensional confocal microscopy. *Applied Optics*, 41(4):685–690, 2002.

[140] H. W. Yoo, M. E. Van Royen, W. A. Van Cappellen, A. B. Houtsmuller, M. Verhaegen, and G. Schitter. Automated spherical aberration correction in scanning confocal microscopy. *Review of Scientific Instruments*, 85(12):1–123706, 2014.

[141] M. J. Booth, M. A. Neil, and T. Wilson. Aberration correction for confocal imaging in refractive-index- mismatched media. *Journal of Microscopy*, 192(2):90–98, 1998.

[142] Bao Cao, Lars Christophersen, Mette Kolpen, Peter Østrup Jensen, Kim Sneppen, Niels Høiby, Claus Moser, and Thomas Sams. Diffusion Retardation by Binding of Tobramycin in an Alginate Biofilm Model. *PLoS ONE*, 11(4):e0153616.1–e0153616.11, 2016.

[143] Mikhail A. Livshits and Andrei D. Mirzabekov. Theoretical analysis of the kinetics of DNA hybridization with gel- immobilized oligonucleotides. *Biophysical Journal*, 71(5):2795–2801, 1996.

[144] Ashlee N. Ford Versypt, Paul D. Arendt, Daniel W. Pack, and Richard D. Braatz. Derivation of an analytical solution to a reaction-diffusion model for autocatalytic degradation and erosion in polymer microspheres. *PLoS ONE*, 10(8):e0135506.1–e0135506.14, 2015.

[145] Casey J. Galvin, Kentaro Shirai, Ali Rahmani, Kakuta Masaya, and Amy Q. Shen. Total Capture, Convection-Limited Nanofluidic Immunoassays Exhibiting Nanoconfinement Effects. *Analytical Chemistry*, 90(5):3211–3219, 2018.

[146] John Zenk, Dominic Scalise, Kaiyuan Wang, Phillip Dorsey, Joshua Fern, Ariana Cruz, and Rebecca Schulman. Stable DNA-based

reaction-diffusion patterns. *RSC Advances*, 7(29):18032–18040, 2017.

[147] Marat O. Gallyamov. Sharp diffusion front in diffusion problem with change of state. *European Physical Journal E*, 36(8), 2013.

[148] John Crank. The Mathematics of Diffusion. In *Clarendon Press*, pages 148–149. Oxford University Press, Oxford, second edition, 1975.

[149] Adelene Y. L. Sim, Jan Lipfert, Daniel Herschlag, and Sebastian Doniach. Salt dependence of the radius of gyration and flexibility of single-stranded DNA in solution probed by small-angle x-ray scattering. *Physical Review E*, 86:1–021901, 2012.

[150] Masayuki Tokita and Toyoichi Tanaka. Friction coefficient of polymer networks of gels. *The Journal of Chemical Physics*, 95(6):4613–4619, 1991.

[151] Arivalagan Gajraj and Robert Y. Ofoli. Effect of extrinsic fluorescent labels on diffusion and adsorption kinetics of proteins at the liquid-liquid interface. *Langmuir*, 16(21):8085–8094, 2000.

[152] Bernardo G. Moreira, Yong You, Mark A. Behlke, and Richard Owczarzy. Effects of fluorescent dyes, quenchers, and dangling ends on DNA duplex stability. *Biochemical and Biophysical Research Communications*, 327(2):473–484, 2005.

[153] Robert Sjöback, Jan Nygren, and Mikael Kubista. Characterization of Fluorescein – Oligonucleotide Conjugates and Measurement of Local Electrostatic Potential. *Biopolymers*, 46:445–453, 1998.

[154] Peter Schuck. Kinetics of ligand binding to receptor immobilized in a polymer matrix, as detected with an evanescent wave biosensor. I. A computer simulation of the influence of mass transport. *Biophysical Journal*, 70(3):1230–1249, 1996.

[155] Eleonóra Parelius Jonášová and Bjørn Torger Stokke. Bioresponsive DNA-co-polymer hydrogels for fabrication of sensors. *Current Opinion in Colloid and Interface Science*, 26:1–8, 2016.

[156] Max A English, Luis R Soenksen, Raphael V Gayet, Helena de Puig, Nicolaas M Angenent-Mari, Angelo S Mao, Peter Q Nguyen, James J Collins, Helena De Puig, Nicolaas M Angenent-Mari, Angelo S Mao, Peter Q Nguyen, James J Collins, Helena de Puig, Nicolaas M Angenent-Mari, Angelo S Mao, Peter Q Nguyen, and James J Collins. Programmable CRISPR-responsive smart materials. *Science (New York, N.Y.)*, 365(6455):780–785, 2019.

[157] Angelo Cangialosi, Chang Kyu Yoon, Jiayu Liu, Qi Huang, Jingkai Guo, Thao D. Nguyen, David H. Gracias, and Rebecca Schulman. DNA sequence–directed shape change of photopatterned hydrogels via high-degree swelling. *Science*, 357(6356):1126–1130, 2017.

[158] Karolyn Barker, Shiva K. Rastogi, Jose Dominguez, Travis Cantu, William Brittain, Jennifer Irvin, and Tania Betancourt. Biodegradable DNA-enabled poly(ethylene glycol) hydrogels prepared by copper-free click chemistry. *Journal of Biomaterials Science, Polymer Edition*, 27(1):22–39, 2016.

[159] Kye Won Wang, Tania Betancourt, and Carol K. Hall. Computational Study of DNA-Cross-Linked Hydrogel Formation for Drug Delivery Applications. *Macromolecules*, 51(23):9758–9768, 2018.

[160] Soong Ho Um, Jong Bum Lee, Nokyoung Park, Sang Yeon Kwon, Christopher C. Umbach, and Dan Luo. Enzyme-catalysed assembly of DNA hydrogel. *Nature Materials*, 5(10):797–801, 2006.

[161] Friedrich C. Simmel and Rebecca Schulman. Self-organizing materials built with DNA. *MRS Bulletin*, 42(12):913–919, 2017.

[162] Zhongyang Xing, Alessio Caciagli, Tianyang Cao, Iliya Stoev, Mykolas Zupkauskas, Thomas O'Neill, Tobias Wenzel, Robin Lamboll, Dongsheng Liu, and Erika Eiser. Microrheology of DNA hydrogels. *Proceedings of the National Academy of Sciences of the United States of America*, 115(32):8137–8142, 2018.

Paper I

Current Opinion in Colloid & Interface Science 26 (2016) 1–8

Contents lists available at ScienceDirect

Current Opinion in Colloid & Interface Science

journal homepage: www.elsevier.com/locate/cocis

Bioresponsive DNA-co-polymer hydrogels for fabrication of sensors

Eleonóra Parelius Jonášová, Bjørn Torger Stokke *

Biophysics and Medical Technology, Dept of Physics, NTNU The Norwegian University of Science and Technology, NO-7491 Trondheim, Norway

ARTICLE INFO

Article history:
Received 7 June 2016
Received in revised form 30 June 2016
Accepted 11 July 2016
Available online 29 July 2016

Keywords:
DNA-co-polymer hydrogels
Biosensing
Responsive hydrogels
Aptamers

ABSTRACT

Bioresponsive hydrogels that include DNA within a non-DNA network (DNA-co-polymer hydrogels) constitute a group of soft materials possessing selective recognition ability hosted by the included DNA structure. They are furthermore characterized by the changes to the hydrogel properties which follow the recognition of the biological analyte. Such hydrogels can be synthesized with desired recognition ability through the selection of particular nucleotide sequence that is recognizing or binding ions, small molecules, biomolecules or parts of larger entities. The binding of the label-free analyte triggers a response of the hydrogel, such as changes in its swelling volume, mass, optical or mechanical properties. The hydrogel response is mediated by changes in network parameters such as charge density, crosslinking density or a combination of these associated with the interaction with the analyte. Bioresponsive DNA polymer hydrogels have found wide application in biosensors due to their versatile nature.

1. Introduction

In nature, nucleic acids are essential molecules in carrying genetic information, responsible for its transmission and translation. The hereditary functionality of nucleic acids was demonstrated more than 70 years ago, and has been widely penetrating the field of molecular biology since then. The facts that DNA adopts a double helical structure stabilized by the base-pair (bp) couples A and T and G and C between the opposing strands; that the two single-stranded constituents are antiparallel; and that the helix is topologically linear; are key features in such a context. The field of DNA nanotechnology has evolved based on the versatility of the DNA molecular structure combined with the capability to synthesize specified bp sequences. Thus, molecular constructs such as tiles, lattices, origamis with vast variety of geometries, nanoscale cubes with locks that can be opened with specific cues, and dynamic structures, have been reported [1–5]. The field of DNA-co-polymer hydrogels, i.e. DNA structures integrated into non-DNA polymer based hydrogels has emerged in the past 20 years following the first report on end-attachment of oligonucleotides amino modified at their 5′ end to a water soluble synthetic (vinyl) polymer [6••]. The aim of this first report was to include single-stranded (ss), bp complementary oligonucleotides grafted to polymers so that they formed additional DNA-based non-covalent crosslinks. The temperature dependence of the hybridization and denaturation of complementary oligonucleotides was then reflected in the temperature dependent crosslinking density of the hydrogel. It was reported that hybridization of the oligodeoxythymidylate (oligoT) and oligodeoxyadenylate (oligoA) did occur in a cast film subsequently immersed in water. This first hybrid DNA-co-polymer study exploited the specific oligonucleotide hybridization reaction as an effector of thermo-sensitive crosslinker functionality of the hydrogel material. Following this initial study, various other functionalities as hosted by the DNA and structural transitions associated with the particular sequence and its recognition have been reported. Incorporation of DNA as the sensing moiety within hydrogels allows for detection of variety of biomolecules. The changes to the gel-bound DNA brought on by the external stimulus lead to a response of the hydrogel. This can include changes in the local structure, overall swelling volume and mass as well as altered mechanical and optical properties. The hydrogel response can be monitored with the use of an appropriate readout platform, thus exploiting the responsive hydrogel as the recognition and transducing functionality in a sensor. This field of DNA-co-polymer hydrogels and their applications are distinct from hydrogels made only of DNA, e.g., by chemical crosslinking of DNA to yield ionic hydrogels with their characteristic properties [7–9]. Although the hybrid DNA-co-polymer field is not as rich in structural DNA motives so far included in the DNA Nanotechnology field, there is an increasing versatility. Recent reviews of hybrid DNA-co-polymer field and mechanisms important for these [10–12], provide an extensive source of relevant literature. In the following account, we focus on hybrid DNA-co-polymers with potential for sensing applications, the design principles exploited to support the specific sensing, how the changes in the integrated DNA structures mediate physical changes affecting the hydrogel and how this can be monitored at the hydrogel level. This will be followed by a brief account of selection procedures for specific DNA sequences and possible alternatives to the DNA with potentially similar versatility.

* Corresponding author.
E-mail address: bjorn.stokke@ntnu.no (B.T. Stokke).

http://dx.doi.org/10.1016/j.cocis.2016.07.001
1359-0294/

2. Hydrogels – handles to include DNA as transducing elements

Successful transformation of changes in a DNA higher order structures to a detectable change in the hydrogel which it is integrated into depends on details in how the DNA structure is included, how the DNA transforms into changes of the hydrogel and how this is determined. In the following, general aspects of transforming hydrogels to responsive hydrogels where changes in DNA higher order structures are mechanistic are outlined. The various effect mediators are outlined based on the Flory-Rehner-Donnan theory of hydrogel swelling, with critical network parameters to be exploited for DNA-polymer hybrid swelling responses. In this account, the equilibrium state is governed by zero total osmotic pressure (Π) of the hydrogel. The total osmotic pressure for the hydrogel swelling state is given by three contributions originating from different molecular mechanisms. The first contribution originates from mixing of solvent and the polymer (Π_{mix}), the second from the elastic retraction occurring on polymer chain deformation (Π_{elas}) and the third originates from concentration differences of ions ΔC_{tot} in the hydrogel relative to its immersing solution (Π_{ion}). Within this theory, the total osmotic pressure is given by [13–17]:

$$\begin{aligned} \Pi &= \Pi_{mix} + \Pi_{elas} + \Pi_{ion} \\ \Pi_{mix} &= \frac{RT}{V_1}\left(\ln \varphi_1 + \varphi_2 + \chi {\varphi_2}^2 \right) \\ \Pi_{elas} &= \frac{\upsilon RT}{V_0}\left(\frac{\varphi_2}{2\varphi_{2,0}} - \left(\frac{\varphi_2}{\varphi_{2,0}} \right)^{1/3} \right) \\ \Pi_{ion} &= RT\Delta C_{tot} \end{aligned} \tag{1.1}$$

where R is the molar gas constant, T is the absolute temperature, V_1 is the molar volume of the solvent, φ_1 and φ_2 are the volume fractions of the solvent and polymer phase, respectively, χ is the Flory-Huggins interaction parameter for intersegment contacts, V_0 is the volume of the hydrogel in the reference state, and υ is the molar number of elastic active polymer chains in reference to volume fraction $\varphi_{2,0}$ of the hydrogel. The term ΔC_{tot} describing the difference in molar concentration of mobile ions between the gel and the immersing aqueous solution can be estimated exploiting the theoretical expression for the Donnan equilibrium governing the ionic balance and using the relevant information on the electrolytes and molecular parameters of the network as reported [13,15].

In swelling equilibrium, when the ionic hydrogel is immersed in a solution with its electrolyte content, the volume fraction φ_2 will adjust to yield zero osmotic pressure. Inclusion of DNA within a polymer network possessing DNA recognition capacity is typically carried out with a small fraction of DNA relative to the polymer it is connected to. Furthermore, it is designed in such a way that the specific recognition and binding transforms into a hydrogel response based on either one, or a combination of effects working through the additive contributions governing the equilibrium swelling state (Eq. (1.1)). A change in DNA-co-hydrogel swelling mediated by affecting the mixing term can possibly be carried out by binding of components with altered hydrophobic nature. Such changes in basic physicochemical properties associated with binding the DNA component of the hydrogel are less discussed in the literature.

The second term represents the elastic restoring force of the network, limiting the overall expansion of DNA-co-polymer network. To have this mechanism playing a role associated with DNA-structural changes requires that the DNA structure undergoing a change on recognition is topologically connected to the polymer network. Or in other words, molecular binding events to a DNA grafted to the network with one end only are not directly affecting the crosslinking density of the network, and for this reason cannot transform the binding event to a change in the thermodynamics of the network through changes in the elastic part. On the other hand, DNA strand or complex of strands that is connected to the network by both its 3′ and 5′ ends, can transform binding events to changes in the term describing the elastic properties due to an altered end-to-end distance and thereby changes in crosslink density.

Exploitation of changes in properties governing the electrostatic contribution to the swelling equilibrium is the third option. Estimation of ΔC_{tot} and how this is related to alterations in changes in charge density driven by DNA based recognition processes can be carried out by exploiting the equilibrium condition for the salt. This can be estimated starting from

$$\Delta C_{tot} = (c_+ + c_-) - (c'_+ + c'_-) \tag{1.2}$$

where c is the concentration of ions and subscripts indicate the positive or negative ions, the prime depicts the immersing solution and the unprimed that within the gel. Within the theory of the infinite bath, the Donnan equilibrium requires electroneutrality in both compartments and equal chemical potential of the mobile ionic species across the gel-immersing solution interface [14,18]. Thus, the following equations are obtained:

$$z_+ c'_+ = z_- c'_- \tag{1.3}$$

$$z_+ c_+ = z_- c_- + z_p c_p \tag{1.4}$$

$$\gamma_\pm^2 c_+ c_- = \gamma'^2_\pm c'_+ c'_- \tag{1.5}$$

where z depict the valences of the cations, anions and polymer indicated by the subscripts +, − and p, respectively, the prime depict the immersing solution and the unprimed that within the gel. Furthermore, $\gamma_\pm^2$ and $\gamma'^2_\pm$ are the mean activity coefficients of the salt inside and outside of the gel raised to the second power. Structural changes of the DNA associated with the recognition process yield changes in the $z_p\, c_p$ parameter, which conventionally also is written:

$$z_p c_p = \frac{\rho \varphi_2}{M_2} \tag{1.6}$$

where ρ is the mass density of the dry polymer network and M_2 is the molar mass of the polymer, including connected DNA, per unit charge. The term $z_p\, c_p$ represents the counterions needed to balance the charged groups on the network, and possible ways to include Manning condensation in the calculation of these have been described [19]. Changes in the charge density of the DNA conjugated to the polymer network associated with the recognition process, can be expected to yield a contribution to the thermodynamics of the swelling, thus inducing a change in the equilibrium swelling state.

3. Changes in DNA higher order structures exploited in DNA-polymer hydrogel swelling changes

DNA is today recognized to have a wide repertoire of higher order structures far beyond the classical antiparallel duplex structure reported by Watson and Crick more than 60 years ago. So far, only a small fraction of such higher order structures have been exploited as recognizing and transducing element in DNA-polymer hydrogels. The DNA structural elements can exploit changes in crosslink density, equilibrium length of the DNA supported part connecting to other polymer chains (e.g., the elastically active network chains), and changes in the charge density of the ionic hydrogel properties as a consequence of the transformative molecular designs. The covalent integration of DNA into hydrogels is a necessary part in realizing the DNA-co-polymer hydrogels. Copolymerization strategies for including DNA strands into acrylamide based materials have been described and are increasingly being exploited due to the commercial availability, including custom designed bp sequences [20–22]. Such an experimental toolbox allows the realization of crosslinks, or elastically active network strands made up of oligonucleotides, alongside covalent crosslinks included by addition of bis

acrylamide. The bp of the oligonucleotides can be designed to simultaneously meet different criteria related to stability of junctions, specificity of recognition, and extent of change in physical dimensions and kinetics of transformation. In the following, we highlight some of these higher order structural elements, with emphasis on their potential changes due to recognition of the specific element when included in a hydrogel. This account focuses on the changes in the physical properties of the higher order structures and does not explicitly include reference to a particular bp sequence other than the complementarity requirements. Particular sequences mediating specificity of the structural changes as realized in selected examples will be discussed below.

The double stranded hybridization reaction, e.g., the complementary bp pairing of one ssDNA with another induces changes both in electrostatic aspects and end-to-end distance that offers means to change the equilibrium swelling state of the hydrogel. The changes in the overall physical extension of the structure due to the hybridization can be estimated by applying additive contributions of the root-mean-square end-to-end distances $\langle r^2_{e\text{-}e}\rangle^{1/2}$ for the single- and double-stranded segments. In the wormlike chain model, $\langle r^2_{e\text{-}e}\rangle$ depends on the contour length, l_c, and persistence length, l_p, as:

$$\langle r_{e-e}{}^2\rangle = 2l_p\left[l_c - l_p\left(1 - e^{-l_c/l_p}\right)\right] \tag{1.7}$$

There is an emerging consensus that the persistence length of dsDNA is about 50 nm in high salt concentrations (see [23] for an overview) although experimental approaches have been reported to yield deviating results. The ssDNA state is much more flexible, and l_p of 1.5 nm (in 2 M NaCl) to 3 nm (in 25 mM NaCl) were reported by fluorescence correlation spectroscopy [24]. Although alternative values of l_p were reported both for the ss and dsDNA structures, we suggest the values of 1.5 nm and 50 nm to provide illustrative examples of changes in the overall extension of the DNA structures. The changes in the overall physical dimensions are estimated as additive contributions from the ss and dsDNA parts as:

$$\Delta\langle r_{e-e}{}^2\rangle^{1/2} = \langle r_{e-e}{}^2\rangle^{1/2}{}_{end} - \langle r_{e-e}{}^2\rangle^{1/2}{}_{start} \tag{1.8}$$

where the value for each state is calculated as the composite value of the ss and ds segments:

$$\langle r_{e-e}{}^2\rangle^{1/2}{}_{state} = \langle r_{e-e}{}^2\rangle^{1/2}(l_{c,s}, l_{p,s}) + \langle r_{e-e}{}^2\rangle^{1/2}(l_{c,d}, l_{p,d}) \tag{1.9}$$

In Eq. (1.9), $l_{c,s}$ and $l_{c,d}$ are the contour length of the ss and dsDNA segments, and $l_{p,s}$ and $l_{p,d}$ the persistence lengths, both parameters referring to the particular state being either the end or start. The contour length for the duplex segments is estimated based on the axial distance of 0.34 nm per bp (from the B-DNA double-helical structure), while a value in the range of 0.43 to 0.58 nm per bp can be used for the ssDNA segments. These values are based on analysis of the electrostatic properties during temperature induced melting of DNA (see below) and the 70% elongation with the transition from the B-DNA to the S-DNA state [25]. The actual change in the overall extension of the DNA structure depends on the structural change, e.g., the number of bp involved in the hybridization, stem-loop change or bp overhang (toehold) in the competitive displacement.

Changes in the electrostatic properties are the other main molecular change exploited for hydrogel transformation triggered by DNA structural changes. Estimates of changes in effective charge of embedded DNA structures can be obtained based on electrostatic properties of ss and dsDNA. The double stranded DNA is among the most heavily charged macromolecules, and combined with its stiff nature, its electrostatic properties are widely explored. The effective polyion charge of dsDNA is reduced from that expected from the chemical composition and spacing along the B-DNA double helical structure due to partial charge neutralization by counterions, e.g. as described by Manning condensation due to the large charge density. In the Manning theory, the dimensionless linear charge density ζ that expresses the relation between the Bjerrum length, l_B, and the average spacing between the charged group of the phosphate backbone, b:

$$\xi = \frac{l_B}{b} \tag{1.10}$$

is a governing parameter. This parameter has a critical maximum value being the inverse of absolute value of valence of the counterions. The Bjerrum length is given by:

$$l_B = \frac{e^2}{4\pi\varepsilon_r\varepsilon_0 k_B T} \tag{1.11}$$

where e is the electronic charge, ε_r and ε_0 are the relative and vacuum permittivity, respectively, k_B is the Boltzman constant and T the absolute temperature. The Bjerrum length in aqueous solution at room temperature is $l_B \approx 0.715$ nm. For the B-DNA double helical structure with $b = 0.17$ nm, the ratio between l_b and b indicates a linear charge density far exceeding the critical value. Thus, counterions are constrained and thereby reducing the long range electrostatic charge density to that corresponding to the critical charge density, being e.g., 0.715 electrons/nm in the case of monovalent counterions. In this model, there are about 0.76 monovalent counterions associated per phosphate group for the B-DNA double helical structure.

Analysis of thermodynamic data for melting of T4 DNA indicates a change in the electrostatic properties, and a value of $b = 0.43 \pm 0.02$ nm per phosphate group in the coil state of DNA was obtained [26,27]. This b value is 26% larger than the axial spacing of phosphate groups in the B-DNA, which is indicating a substantially smaller increase in backbone extension going from the duplex to the ss state than stated above based on force induced structural transitions of duplex DNA.

Various design principles exploited within DNA-co-hydrogels and their connectivity to polymer network are illustrated in Fig. 1. In these illustrations, an analyte being a ssDNA is used to illustrate the structural changes. Nevertheless, recognition events and structural changes initiated by other types of molecules can be analyzed in a similar fashion using aptamer-type binding. The structural changes exploited are grouped into double stranded hybridization (Fig. 1a and b), stem loop-changes (Fig. 1c-f) and competitive displacement (Fig. 1g and h), and either of these types can be exploited with oligonucleotides covalently anchored with only one or both their 5′ and 3′ end to the polymer network. Changes in the charge density of the network associated with the various analytes binding are the main effect driving changes in the state of the hydrogels when only one end of the grafted oligonucleotide is covalently attached (Fig. 1a, c, e and g). The extent of change in the parameter M_2 in the Donnan term for the swelling of the hydrogel depends on the particular change in DNA structure, as well as on the oligonucleotide grafting density of the hydrogel. It should also be noted for the competitive displacement [28] pathway, there are intermediate states where both the displaced oligonucleotide (blocking ssDNA) and analyte ssDNA are bound to the grafted oligonucleotide (this state is not explicitly depicted in Fig. 1g). The individual grafted ssDNA is therefore mediating a charge density going through a maximum.

The other main topology of the grafted oligonucleotide in the polymer network is with both ends (3′ and 5′) connected to the polymer chains. For these topologies, changes in the overall extension or connectivity associated with the recognition event will contribute to alterations in the osmotic pressure contribution arising from the elastic term. For the equilibrated state, this is balanced with the changes in the electrostatic properties altering the Donnan term. For instance, for the hybridization of ssDNA (Fig. 1b), use of the information summarized above indicates that a reduction of the charge density may occur, while there is increase in the end-to-end distance. The interpretation of the data reporting [29••] a decrease of the swelling volume in such a case

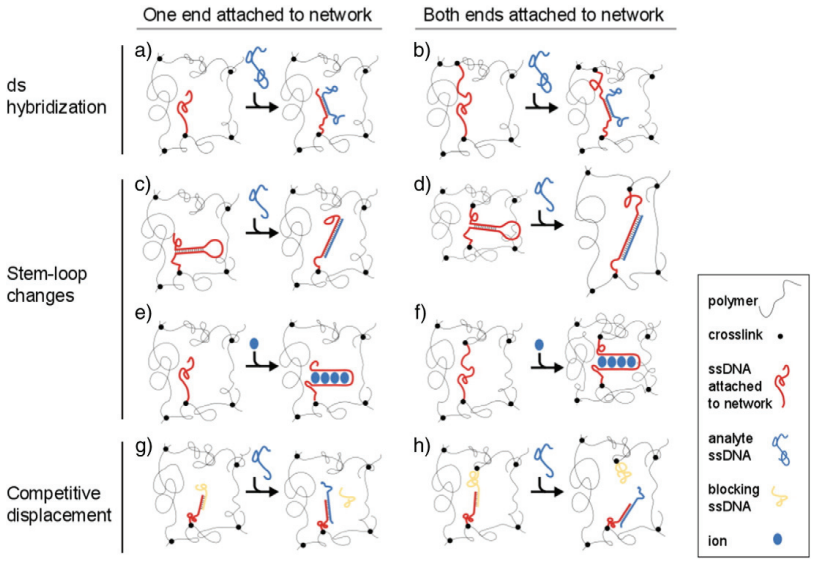

Fig. 1. Schematic illustrations of structural changes in DNA higher order structures utilized in designing responsive DNA-co-polymer hydrogels. The principles are built on double stranded hybridization (Fig. 1a and b), stem loop-changes (Fig. 1c–f) and competitive displacement (Fig. 1g and h). These principally three different DNA structural changes can be exploited in the hydrogel with the oligonucleotides covalently linked with only one or both their 5′ and 3′ end to the polymer network.

needs to include both effects. Similarly, for changes in the stem-loops, both the changes in the end-to-end distances and charge density occur, that contribute to adjustment to a new swelling equilibrium state. For the competitive displacement principle, the completion of the reaction will directly affect the crosslink density. The overall effect of this will also depend on the grafting density of oligonucleotide relative to the covalent crosslink density. The competitive displacement mechanism can also be extended to serially connected, partly hybridized oligonucleotides. There is also a range of additional higher order structures of DNA that can alter their properties based on various stimuli, e.g. [30] of which some already are integrated in hydrogels (see below).

4. Readout principles relevant for DNA-co-polymer hydrogels

The monitoring of consequences of the presence of specifically recognized molecules and the concomitant changes in the hydrogel state are essential in characterization and implementation of DNA-co-polymer as biospecific sensing and transducing elements. With the main strategy of including the DNA structures in the hydrogels being the transformative consequences of the recognition and processing events into readily detectable changes on the hydrogel state, we focus here on the current state of the art of monitoring of hydrogel swelling or mass. The DNA-co-polymer materials focused on here are considered mostly in terms of the label-free sensing concept. That implies that the analyte should not be processed to include some labeling directly monitored by e.g. fluorescence, but it does not imply that components of the hydrogel cannot be designed in a way to exploit spectroscopic detection schemes. The relevant readout principles need to be able to monitor changes in the DNA smart hydrogels that undergo changes when components in the embedding solutions interact with the hydrogels. The response of the DNA-co-polymer hydrogel can include changes in the local structure, overall swelling volume and mass. The re-adjustment to a new equilibrium swelling state is in many cases accompanied by alterations in physical properties, such as mechanical properties, refractive indices, and mass, which are amendable to optical readout or can be transformed to some other signal.

Optically based readout principles comprise a substantial group, and exploit various principles such as embedded colloidal crystal arrays in the hydrogel, Bragg diffraction from surface molded structures, surface plasmon resonance (SPR) and interferometry. Embedding colloidal spheres at sufficiently high concentration in a hydrogel matrix creates sufficient ordering of the beads to make this function like a photonic material. In the pioneering publications of their integration into responsive hydrogel matrixes [31,32], shifts of diffraction peaks driven by temperature of pNIPAM gel was reported. This principle, referred to as polymerized crystalline colloidal array (PCCA) can also be used to monitor swelling changes in DNA-co-polymers, e.g., as implemented for mercury sensing based on its DNA aptamer integrated in such a device [33•]. Monitoring of swelling of hydrogels with imprinted diffraction gratings has been reported for aptamer embedded hydrogels for detection of thrombin, viruses and heavy metals [33•,34,35•] (Fig. 2a). The wavelength of the Bragg reflected waves for the Hg^{2+} induced swelling displayed clearly detectable shifts for Hg^{2+} concentrations as low as 10 nM and the aptamer grafted hydrogel displayed high selectivity for response against Hg^{2+} when compared to other ions such as Pb^{2+}, Ag^{+}, Mn^{2+}, Zn^{2+}, Mg^{2+}, Ca^{2+}, Al^{3+}, Ba^{2+}, Fe^{3+}, Cu^{2+} and Cr^{3+} [33•].

Surface plasmon resonance sensing is based on detection of changes in the refractive index adjacent to metallic surfaces. Surface plasmons arise from the confinement of the light at the interface between a thin metal film and a dielectric medium, which also can be a DNA-co-polymer hydrogel. Changes in the hydrogel structure, e.g. swelling, will alter the concentration of the material and thereby the refractive index, n. The surface plasmons and their resonance frequency depend strongly on Δn, which is the basis for its widespread use in biosensing [36] This readout platform, however, has not been explored for characterization of DNA-co-polymer hydrogels. We have reported on the application of a fiber-optic based interferometric monitoring of swelling of a hemispherical hydrogel synthesized at the end of the optical fiber [37,38•,39] (Fig. 2b). With a typical radius of the biosensing hydrogel

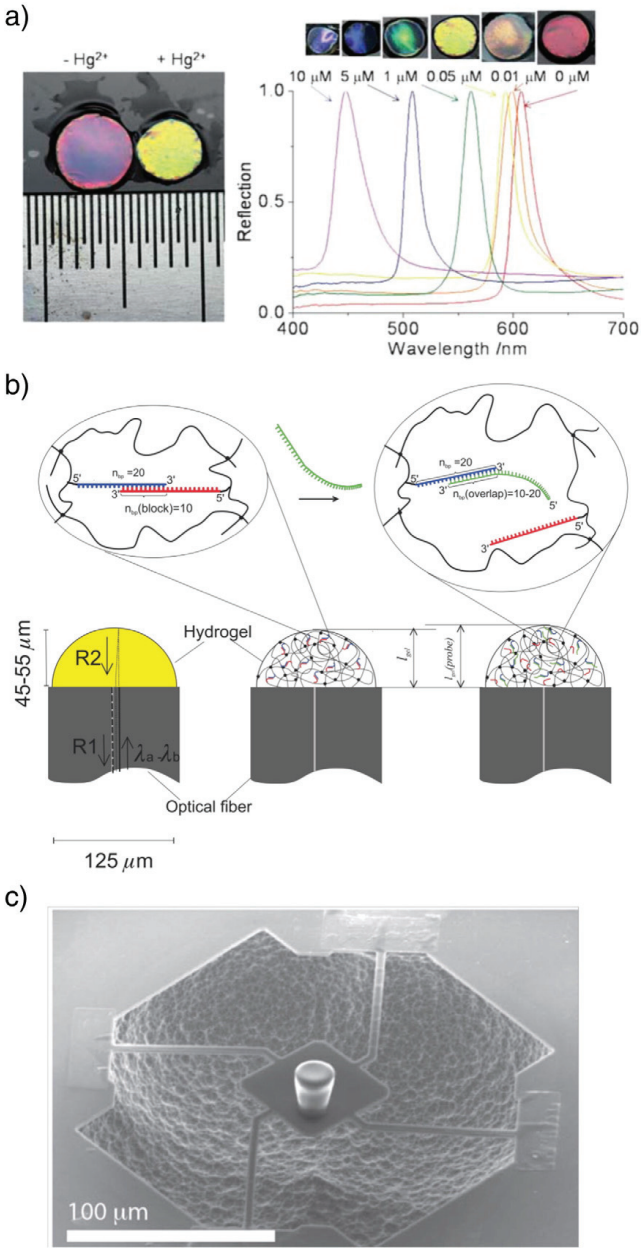

Fig. 2. Examples of some readout platforms for determination of hydrogel swelling. (a) Effect of exposure to mercury ions at increasing concentrations on swelling of a DNA-co-polymer hydrogel embedded with particles to make a photonic crystal material. The end-grafted oligonucleotide was selected as an aptamer sequence capable of inducing a structural change in the presence of Hg^{2+}. Reproduced with permission from [33•], copyright (2012) Royal Society of Chemistry. (b) A fiber-based interferometric set-up where the optical length of a hemispherical DNA-co-polymer hydrogel grafted at the end of the optical fiber is determined with high precision. The hydrogel design includes partly dsDNA grafted at both ends to the polymer, and the dsDNA can be destabilized by competitive displacement by an analyte ssDNA with longer bp complementarity. Reproduced with permission from [38•], copyright (2009) American Chemical Society. (c) A scanning electron micrograph of mass sensor fabricated using MEMS with a hydrogel centered on top. The mass of the PEGDA-DMPA hydrogel fabricated employing lithography was determined from the difference in the resonance frequency of the unloaded and hydrogel loaded mass resonator.
Reproduced with permission from [43], copyright (2012) John Wiley and Sons.

entity of 50 μm, and a resolution of 2 nm in the changes in the optical length passing the hydrogel, the relative sensitivity for detection of changes in swelling is of the order of 0.002%. The quartz crystal microbalance (QCM) readout principle has been employed in combination with DNA embedded hydrogel for the detection of avian influenza virus [40]. In this approach, the binding of the virus induces a decreased in the resonance frequency.

The novel sensing principles based on quantitative phase imaging (QPI), suspended micro-channel resonator (SMR) and pedestal resonant sensor recently highlighted for monitoring of dry cell mass [41, 42] are also interesting to explore for determination of hydrogel mass. This is despite that these sensing principles are not yet widely used, and it is only the MEMS fabricated pedestal resonant sensing principle that so far have been employed for hydrogels [43] (Fig. 2c). Readout based on electrochemical transduction, which in general is widely explored in biosensors, is not used in the field of DNA-co-hydrogels. In addition to the readout platforms mentioned, the field is supported by a number of additional characterization tools, e.g., based on fluorescence.

Designing a functional biosensor for a particular application requires consideration and effective combination of the recognition, transducing and readout parts. The role of the DNA-co-hydrogel is to integrate the recognition (specific reaction of the DNA) and the transduction of the signal (response on the hydrogel level). The last step is the readout of the hydrogel response, which has to be selected based on the type of response to be monitored as well as requirements on the sensitivity, set-up size, and other factors. The hydrogels can be synthesized in various shapes and sizes to accommodate different readout platforms. Several of the readout platforms mentioned above are not straightforward to include as basis for e.g., in vivo sensing, but there is also an ongoing technological development driven by the miniaturization approaches that can be expected to enhance integration of readout principles currently not considered for in vivo testing. The miniaturization of the optical confocal principle to a device based on an endoscope [44] is one example of this, although not directly supporting hydrogel readout.

5. Selection of oligonucleotide sequence

In the above description, we focused on the general aspect of DNA as a dynamic structure without being specific on the particular bp sequence except requirements on the duplex and stem-loop structures. For particular realizations, design of bp sequence to accommodate specificity for a specific recognition, and kinetics of the dynamic change are required. The inherent capacity of DNA to bind to other types of molecules than their complementary oligonucleotide is well recognized and exploited today. Of particular importance to identify novel sequences is the SELEX process (Systematic Evolution of Ligands by Exponential enrichment) [45••,46••], that has led to identification of particular oligonucleotide sequences, aptamers, exploited in various fields, including also integration in DNA-co-hydrogels.

6. Examples of DNA-co-hydrogels

Table 1 summarizes some of the hydrogels developed in the last 20 years that possess sensor functionality and fall into the category of DNA-polymer hydrogels, i.e. they employ DNA as the detecting moiety within a non-DNA polymer network. The most common type of supporting network is based on acrylamide and is used in all of the presented examples. This can be explained by the availability of DNA strands modified with Acrydite that allows them to be copolymerized with acrylamide.

The recognition processes used in the presented hydrogel designs, while often more complicated than the ones summarized in Fig. 1, can still be classified using these basic principles or their combinations: simple hybridization of a gel bound DNA strand to the analyte DNA strand [29••], and its equivalent with a single gel bound aptamer binding the ligand [33•,47,48] (where [48] can also fall into the category of stem-loop formation as a result of ligand binding); stem-loop straightening with a complementary DNA strand [29••]; competitive displacement involving an initial complex of 2 [38•,49] or 3 DNA strands [50••,51] and an aptamer equivalent of competitive displacement where the disruption of the complex is caused by one of the strands binding to a non-DNA ligand [35•,52••,53–55,56•], also involving 2 or 3 DNA strands. Some principles are more difficult to categorize, such as in the hydrogels developed by Bai et al. [57•], which use an assembly of aptamers (termed super-aptamer) to bind thrombin and later a virus particle within the hydrogel. The specific interactions of aptamers with the ligand form supramolecular crosslinks which cause the hydrogel to shrink.

Almost all of the presented systems have the recognition DNA complex anchored to the network with 2 (or more) attachments. This means that the DNA complex behaves as a crosslink, so changes to its stiffness or the dissociation of strands (and subsequent crosslink opening) will have an effect on the elastic part of the osmotic pressure. The two hydrogels in which the DNA is only anchored with one end have been prepared by Dave et al. [48] and Srinivas et al. [47]. Both designs use a single DNA strand bound to the network that can bind mercury ions and thrombin, respectively. Furthermore, the readout is based on fluorescence in both of the cases. Dave et al. use SYBR Green I dye which changes its fluorescence wavelength from yellow in the presence of DNA with random coil structure, to green when the DNA adopts a hairpin (stem-loop) structure. This structural change is a result of aptamer-Hg^{2+} binding. The design has been subsequently improved by tailoring the electrostatic interactions of the dye with the hydrogel [58], improving the sensitivity, and later by using microparticles instead of monolithic hydrogels to improve the kinetics of the response [59]. Srinivas et al. used a sandwich-assay within microgels, with one 'capture' aptamer bound to the gel and a free 'reporter' aptamer that was fluorescently labeled. The capture of the thrombin within the hydrogel microparticles was assessed using static imaging and microfluidic flow-through analysis.

There is a clear tendency towards increased use of aptamer-type binding, as this gives DNA-based sensors their versatility allowing for binding of various targets from ions [48], through small molecules [52••] to viruses [34] and cells [60]. There are also several hydrogel designs which support a dual input, responding to two different stimuli. One such hydrogel has been developed by Sicilia et al. [49], employing dsDNA crosslink that can be opened by complementary ssDNA as well as disulfide crosslinks that are disrupted by reducing conditions. The combination of these effects can be used to control the pore size and allow for controlled release of the gel's load. A gel developed by Yin et al. [55] uses a complex of three DNA strands within the gel, two of which have aptamer functionalities, binding ATP and cocaine. Depending on the details of the design, OR and AND logic gates can be materialized with either or both of the ligands being needed to disrupt the network and release gold nanoparticles, which provide the colorimetric output visible to the naked eye.

When considering the readout platforms used to monitor the presented hydrogels, it can be seen that many rely on sol–gel transition. One of the reasons for this is that some of the presented gels were designed for controlled release [49,51,52••], rather than sensing. However, they still possess sensing functionality and could be tailored for sensing purposes. Sol–gel transitions can be combined with fluorometric or colorimetric analyses, using quantum dots [51] or gold nanoparticles [54, 55] that are released following the binding of the analyte and the subsequent disruption of the network. Fluorescence can also be used on its own, without sol–gel transition, in cases where the binding of the analyte triggers fluorescent output [47,48]. An interesting use of the sol–gel transition was employed by Yan, Zhu et al. [56•], where the disruption of the network releases glucoamylase which then degrades the amylose, which was present outside of the gel, into glucose. The glucose levels then can be measured using a personal glucose meter. This example also shows a possible way of using controlled release type of

Table 1
Examples of DNA-co-hydrogels, their analyte, recognition process, readout and sensitivity.

Analyte	#Attachments	Recognition process	Readout	Purpose	Sensitivity	Citation
ssDNA	2	Competitive displacement, Initial complex of 3 strands	Sol–gel transition	Characterization Rheology		[50••]
ssDNA	2	1)Stem-loop straightening 2) hybridization	Size measurement in optical microscopy	Detection		[29••]
ssDNA	2	Competitive displacement, initial complex of 3 strands	Sol–gel transition, quantum dots	Controlled release		[51]
Adenosine	2	'Competitive displacement'. Initial complex of 3 strands disrupted when one strand binds adenosine	Sol–gel transition	Controlled release		[52••]
ssDNA, triggers thrombin release	2	Competitive displacement. Initial complex of 3 strands, 2 bound to gel, third binding also thrombin. Competitive displacement releases thrombin	Sol–gel transition	Controlled release		[53]
Cocaine	2	'Competitive displacement'. Initial complex of 3 strands disrupted when one strand binds cocaine	Sol–gel transition, AuNPs	Detection	20 ng	[54]
Hg^{2+}	1	Aptamer functionality, binding mercury, creating a stem-loop	Fluorescence	Detection and capture	10 nM	[48]
Thrombin	1	Aptamer functionality, binding thrombin	Fluorescence	Detection	4 pM	[47]
Heavy metal ions	2	Aptamer functionality, binding heavy metal ions	CPCH (colloidal photonic crystal hydrogel)	Detection	10 nM	[33•]
Cocaine and ATP	2	'Competitive displacement', Y DNA structure disrupted by the analytes	Sol–gel transition, AuNPs	Detection		[55]
Thrombin	2	'Competitive displacement', ds crosslinked opened when one strand binds thrombin	Diffraction grating	Detection	0.01 mg/ml	[35•]
Cocaine	2	'Competitive displacement'. Initial complex of 3 strands disrupted when one strand binds cocaine	Sol–gel transition of gel releases gel bound enzyme that degrades amylose to glucose and is detected with personal glucose meter	Detection	4.4 μM	[56•]
Thrombin	2 or more	Super-aptamer- assembly of aptamers. When binding to target they work as additional crosslinks	Volume change observed in capillaries	Detection	fM	[57•]
Virus	2 or more	Super-aptamer	Diffraction grating	Detection	10 ng/ml	[34]
ssDNA	2	Competitive displacement		Controlled release, Dual input		[49]

hydrogels for sensing purposes, by using the released molecule as a measurable output. Apart from sol–gel transition and fluorescence, measurements of the hydrogel size can be used to monitor its response. It can be done directly with the help of an optical microscope [29••], or with naked eye such as in the case of gels manufactured by Bai et al. [57•] inside of glass capillaries, where a small change in volume was translated into a large change in length of the gel. However, hydrogels often have very small sizes which require different methods for size monitoring. The methods used with the presented hydrogels are: interferometric readout of the size of a hydrogel synthetized at the end of an optical fiber [38•], the use of diffraction gratings [34,35•] and the Bragg diffraction based colloidal crystal array (CPCH) of monodisperse silica nanoparticles [33•] which have been discussed before.

7. DNA analogs

Hydrogels exploiting DNA analogues, such as peptide nucleic acid (PNA), locked DNA are so far rare. Kopecek and coworkers [61] reported on exploiting PNA in combination with DNA in a hybrid design. The focus was on the possible ssDNA mediated crosslinking of a PNA grafted on a water soluble polymer (HPMA). PNA are capable of forming hybrid duplex structures with DNA making a ssPNA-ssDNA duplex structure as well as other assembly modes between these two types of components. Substituting PNA with DNA in the structural changes will affect both the electrostatic considerations outlined above since it will represent substituting the highly charged DNA backbone with a peptide based one not carrying charges. Other DNA analogous like locked DNA (LNA) [62] or click nucleic acids [63] are so far not applied in hydrogels similar to DNA.

8. Conclusions

The current literature shows DNA-co-hydrogels as (bio) sensing materials to have large versatility with respect to recognition capacities that can be included. Use of DNA as a recognition supporting element allows for a range of varying binding and transformative reactions as well as an almost unlimited list of possible analytes through aptamer reactions. The inclusion of this powerful tool within a hydrogel can facilitate the monitoring of the sensing reaction, as the role of the responsive hydrogel is to translate the change undergone by its sensing part (DNA) into a change in the state of the hydrogel itself. Consequently, monitoring the changes in the hydrogel can reveal information on the specific recognition reactions taking place without the need for labeling or processing the analyte. However, most of the current responsive DNA-co-hydrogels that have been demonstrated are based on a sol–gel transition to monitor the changes. While this is the only necessary outcome if controlled release is the goal, for sensing applications more accurate monitoring can be desirable. A variety of readout platforms are available, but not often integrated with DNA-co-hydrogel sensors. We expect further advancement, as to exploit DNA-co-hydrogels as sensing and transducing materials will require stronger consideration of the kinetic aspects, the integration of these responsive materials with readout platforms that are appropriate for the particular monitoring, being it of environmental character, biomarker detection in clinical setting or narcotics. The combination of high sensitivity and specificity of the nucleotide based recognition should make them an ideal choice, where we so far only have seen a few of the all potential application areas.

References and recommended reading•,••

[1] Rothemund PWK. Folding DNA to create nanoscale shapes and patterns. Nature 2006;440:297–302.
[2] Andersen ES, Dong M, Nielsen MM, Jahn K, Subramani R, Mamdouh W, et al. Self-assembly of a nanoscale DNA box with a controllable lid. Nature 2009;459, 73-U5.
[3] Zhang F, Nangreave J, Liu Y, Yan H. Structural DNA nanotechnology: state of the art and future perspective. J Am Chem Soc 2014;136:11198–211.

• Of special interest.
•• Of outstanding interest.

[4] Jones MR, Seeman NC, Mirkin CA. Programmable materials and the nature of the DNA bond. Science 2015;347.
[5] Seeman NC, Structural DNA. Nanotechnology. Cambridge, U.K.: MRS Materials Research Society, Cambridge University Press; 2015
[6] Nagahara S, Matsuda T. Hydrogel formation via hybridization of oligonucleotides derivatized in water-soluble vinyl polymers. Polym gels networks. 1996;4:111–27 [Oligonucleotides were integrated within a polyacrylamide hydrogel for the first time. Most DNA-copolymer hydrogel since then use the same chemistry].
[7] Amiya T, Tanaka T. Phase transitions in crosslinked gels of natural polymers. Macromolecules 1987;20:1162–4.
[8] Costa D, Hansson P, Schneider S, Miguel MG, Lindman B. Interaction between covalent DNA gels and a cationic surfactant. Biomacromolecules 2006;7:1090–5.
[9] Costa D, Queiroz J, Miguel MG, Lindman B. Swelling behavior of a new biocompatible plasmid DNA hydrogel. Colloids Surf B Biointerfaces 2012;92:106–12.
[10] Liu JW. Oligonucleotide-functionalized hydrogels as stimuli responsive materials and biosensors. Soft Matter 2011;7:6757–67.
[11] Li J, Mo LT, Lu CH, Fu T, Yang HH, Tan WH. Functional nucleic acid-based hydrogels for bioanalytical and biomedical applications. Chem Soc Rev 2016;45:1410–31.
[12] Baker BA, Mahmoudabadi G, Milam VT. Strand displacement in DNA-based materials systems. Soft Matter 2013;9:11160–72.
[13] Schröder UP, W O. Properties of Polyelectrolyte Gels. Physical Properties of Polymeric Gels. Chichester: J. Wiley & Sons; 1996 19–38.
[14] Treloar LRG. The Physics of Rubber Elasticity. Oxford: Clarendon Press; 1975.
[15] Shibayama M, Tanaka T. Volume phase transition and related phenomena of polymer gels. Adv Polym Sci 1993;109:1–62.
[16] Brannonpeppas L, Peppas NA. Equilibrium swelling behavior of pH-sensitive hydrogels. Chem Eng Sci 1991;46:715–22.
[17] Eichenbaum GM, Kiser PF, Dobynin AV. Investigation of the swelling response and loading of ionic microgels with drugs and proteins: the dependence on cross-link density. Macromolecules 1999;32:4867–78.
[18] Tanford C. Physical chemistry of macromolecules. Physical chemistry of macromolecules. N.Y.: John Wiley & Sons Inc.; 1961
[19] Guo B, Elgsaeter A, Christensen BE, Stokke BT. Sclerox-chitosan co-gels: effects of charge density on swelling of gels in ionic aqueous solution and in poor solvents, and on the rehydration of dried gels. Polym Gels Networks 1998;6:471–92.
[20] Kenney M, Ray S, Boles TC. Mutation typing using electrophoresis and gel-immobilized acrydite (TM) probes. Biotechniques 1998;25:516–21.
[21] Nelson C, Hendy S, Reid K, Cavanagh J. Acrylamide capture of DNA-bound complexes: electrophoretic purification of transcription factors. Biotechniques 2002; 32:808–15.
[22] Chan A, Krull UJ. Capillary electrophoresis for capture and concentrating of target nucleic acids by affinity gels modified to contain single-stranded nucleic acid probes. Anal Chim Acta 2006;578:31–42.
[23] M. U. Polyelectrolytes. physicochemical aspects and biological significance. DNA Interactions with Polymers and Surfactants; 2007. p. 1–39.
[24] Murphy MC, Rasnik I, Cheng W, Lohman TM, Ha T. Probing single-stranded DNA conformational flexibility using fluorescence spectroscopy. Biophys J 2004;86: 2530–7.
[25] Ritort F. Single-molecule experiments in biological physics: methods and applications. J Phys Condens Matter 2006;18, R531-R83.
[26] Record MT, Anderson CF, Lohman TM. Thermodynamic analysis of ion effects on the binding and conformational equilibria of proteins and nucleic acids: the role of ion association or release, screening, and ion effects on water activity. Q Rev Biophys 1978;11:103–78.
[27] Bloomfield VA, Crothers DM, Tinoco I. Nucleic Acids. Structures, properties and Functions. Sausalito: University Science Books; 2000.
[28] Srinivas N, Ouldridge TE, Sulc P, Schaeffer JM, Yurke B, Louis AA, et al. On the biophysics and kinetics of toehold-mediated DNA strand displacement. Nucleic Acids Res 2013;41:10641–58.
[29] Murakami Y, Maeda M. DNA-responsive hydrogels that can shrink or swell. Biomacromolecules 2005; 6: 2927-9. [Prepared the first shrinking and swelling DNA-hydrogels. The binding of the target DNA did not lead to the opening of the DNA crosslink, merely changing its stiffness and charge density. Consequently, the hydrogels did not dissolve, but responded by shrinking or swelling depending on the design. This work demonstrated how differing DNA sequences within the hydrogel can lead to different behavior and used size measurement as a readout method].
[30] Wang F, Liu XQ, Willner I. DNA switches: from principles to applications. Angew Chem Int Ed 2015;54:1098–129.
[31] Holtz JH, Asher SA. Polymerized colloidal crystal hydrogel films as intelligent chemical sensing materials. Nature 1997;389:829–32.
[32] Weissman JM, Sunkara HB, Tse AS, Asher SA. Thermally switchable periodicities and diffraction from mesoscopically ordered materials. Science 1996;274:959–60.
[33] Ye B-F, Zhao Y-J, Cheng Y, Li T-T, Xie Z-Y, Zhao X-W, et al. Colorimetric photonic hydrogel aptasensor for the screening of heavy metal ions. Nanoscale 2012;4: 5998–6003 [Hydrogel size monitoring using colloidal photonic crystal hydrogel].
[34] Bai W, Spivak DA. A double-imprinted diffraction-grating sensor based on a virus-responsive super-aptamer hydrogel derived from an impure extract. Angew Chem Int Ed 2014;53:2095–8.
[35] Wang X, Wang X. Aptamer-functionalized hydrogel diffraction gratings for the human thrombin detection. Chem Commun 2013;49:5957–9 [Use of hydrogel diffraction gratings].
[36] Johnsson B, Lofas S, Lindquist G. Immobilization of proteins to a carboxymethyldextran-modified gold surface for biospecific interaction analysis in surface-plasmon resonance sensors. Anal Biochem 1991;198:268–77.
[37] Tierney S, Hjelme DR, Stokke BT. Determination of swelling of responsive gels with nanometer resolution. Fiber-optic based platform for hydrogels as signal transducers. Anal Chem 2008;80:5086–93.
[38] Tierney S, Stokke BT. Development of an oligonucleotide functionalized hydrogel integrated on a high resolution interferometric readout platform as a label-free macromolecule sensing device. Biomacromolecules 2009;10:1619–26 [Introduction of interferometric readout for hydrogel size monitoring].
[39] Gao M, Gawel K, Stokke BT. Toehold of dsDNA exchange affects the hydrogel swelling kinetics of a polymer-dsDNA hybrid hydrogel. Soft Matter 2011;7:1741–6.
[40] Wang RH, Li YB. Hydrogel based QCM aptasensor for detection of avian influenza virus. Biosens Bioelectron 2013;42:148–55.
[41] Popescu G, Park K, Mir M, Bashir R. New technologies for measuring single cell mass. Lab Chip 2014;14:646–52.
[42] Park K, Millet LJ, Kim N, Li HA, Jin XZ, Popescu G, et al. Measurement of adherent cell mass and growth. Proc Natl Acad Sci U S A 2010;107:20691–6.
[43] Millet LJ, Corbin EA, Free R, Park K, Kong H, King WP, et al. Characterization of mass and swelling of hydrogel microstructures using MEMS resonant mass sensor arrays. Small 2012;8:2555–62.
[44] Piyawattanametha W, Ra H, Qiu Z, Friedland S, Liu JTC, Loewke K, et al. In vivo near-infrared dual-axis confocal microendoscopy in the human lower gastrointestinal tract. J Biomed Opt 2012;17:0211021–4.
[45] Ellington AD, Szostak JW. In vitro selection of RNA molecules that bind specfic ligands. Nature 1990;346:818–22 [The development of SELEX – method to select oligonucleotides with binding affinity to a given target – enabled all aptamer-based sensitive hydrogels].
[46] Tuerk C, Gold L. Systematic evolution of ligands by exponential enrichment - RNA ligands to bacteriophage T4 DNA-polymerase. Science 1990;249:505–10 [The development of SELEX – method to select oligonucleotides with binding affinity to a given target – enabled all aptamer-based sensitive hydrogels].
[47] Srinivas RL, Chapin SC, Doyle PS. Aptamer-functionalized microgel particles for protein detection. Anal Chem 2011;83:9138–45.
[48] Dave N, Chan MY, Huang P-JJ, Smith BD, Liu J. Regenerable DNA-functionalized hydrogels for ultrasensitive, instrument-free mercury(II) detection and removal in water. J Am Chem Soc 2010;132:12668–73.
[49] Sicilia G, Grainger-Boultby C, Francini N, Magnusson JP, Saeed AO, Fernandez-Trillo F, et al. Programmable polymer-DNA hydrogels with dual input and multiscale responses. Biomater Sci 2014;2:203–11.
[50] Lin DC, Yurke B, Langrana NA. Mechanical properties of a reversible, DNA-crosslinked polyacrylamide hydrogel. J Biomech Eng 2004;126:104–10 [The authors reported the first DNA-copolymer hydrogel sensitive to DNA. A polyacrylamide hydrogel, crosslinked solely by DNA strands was dissolved by addition of a complementary DNA strand that opened the crosslink in a process of competitive displacement].
[51] Liedl T, Dietz H, Yurke B, Simmel F. Controlled trapping and release of quantum dots in a DNA-switchable hydrogel. Small 2007;3:1688–93.
[52] Yang H, Liu H, Kang H, Tan W. Engineering target-responsive hydrogels based on aptamer — target interactions. J Am Chem Soc 2008;130:6320–1 [First hydrogel using aptamers to target a molecule, in this case adenosine].
[53] Wei B, Cheng I, Luo KQ, Mi Y. Capture and release of protein by a reversible DNA-induced Sol–gel transition system. Angew Chem Int Ed 2008;47:331–3.
[54] Zhu Z, Wu C, Liu H, Zou Y, Zhang X, Kang H, et al. An aptamer cross-linked hydrogel as a colorimetric platform for visual detection. Angew Chem Int Ed 2010;49:1052–6.
[55] Yin B-C, Ye B-C, Wang H, Zhu Z, Tan W. Colorimetric logic gates based on aptamer-crosslinked hydrogels. Chem Commun 2012;48:1248–50.
[56] Yan L, Zhu Z, Zou Y, Huang Y, Liu D, Jia S, et al. Target-responsive "sweet" hydrogel with glucometer readout for portable and quantitative detection of non-glucose targets. J Am Chem Soc 2013;135:3748–51 [Binding of the target leading to a sol–gel transition release amylase from the gel to the solution where it degrades amylose to glucose. Glucose can then be measured using a personal glucose meter, providing a more quantifiable measurement].
[57] Bai W, Gariano NA, Spivak DA. Macromolecular amplification of binding response in superaptamer hydrogels. J Am Chem Soc 2013;135:6977–84 [Use of diffraction grating for size monitoring of the hydrogel. Their hydrogel is also capable of detecting viruses, based on cooperation of many aptamers].
[58] Joseph KA, Dave N, Liu J. Electrostatically directed visual fluorescence response of DNA-functionalized monolithic hydrogels for highly sensitive Hg2 + detection. ACS Appl Mater Interfaces 2011;3:733–9.
[59] Helwa Y, Dave N, Froidevaux R, Samadi A, Liu J. Aptamer-functionalized hydrogel microparticles for fast visual detection of mercury(II) and adenosine. ACS Appl Mater Interfaces 2012;4:2228–33.
[60] Li SH, Chen NAC, Gaddes ER, Zhang XL, Dong C, Wang Y. A drosera-bioinspired hydrogel for catching and killing cancer cells. Sci Rep 2015;5.
[61] Chu TW, Feng JY, Yang JY, Kopecek J. Hybrid polymeric hydrogels via peptide nucleic acid (PNA)/DNA complexation. J Control Release 2015;220:608–16.
[62] Petersen M, Wengel J. LNA: a versatile tool for therapeutics and genomics. Trends Biotechnol 2003;21:74–81.
[63] Xi W, Pattanayak S, Wang C, Fairbanks B, Gong T, Wagner J, et al. Clickable nucleic acids: sequence-controlled periodic copolymer/oligomer synthesis by orthogonal Thiol-X reactions. Angew Chem Int Ed 2015;54:14462–7.

Paper II

Journal of Biomedical Optics

BiomedicalOptics.SPIEDigitalLibrary.org

Recovering fluorophore concentration profiles from confocal images near lateral refractive index step changes

Eleonóra Parelius Jonášová
Astrid Bjørkøy
Bjørn Torger Stokke

SPIE.

Eleonóra Parelius Jonášová, Astrid Bjørkøy, Bjørn Torger Stokke, "Recovering fluorophore concentration profiles from confocal images near lateral refractive index step changes," *J. Biomed. Opt.* **21**(12), 126014 (2016), doi: 10.1117/1.JBO.21.12.126014.

Journal of Biomedical Optics 21(12), 126014 (December 2016)

TECHNICAL NOTE

Recovering fluorophore concentration profiles from confocal images near lateral refractive index step changes

Eleonóra Parelius Jonášová, Astrid Bjørkøy, and Bjørn Torger Stokke*
Norwegian University of Science and Technology (NTNU), Section for Biophysics and Medical Technology, Department of Physics, Høgskoleringen 5, Trondheim 7491, Norway

Abstract. Optical aberrations due to refractive index mismatches occur in various types of microscopy due to refractive differences between the sample and the immersion fluid or within the sample. We study the effects of lateral refractive index differences by fluorescence confocal laser scanning microscopy due to glass or polydimethylsiloxane cuboids and glass cylinders immersed in aqueous fluorescent solution, thereby mimicking realistic imaging situations in the proximity of these materials. The reduction in fluorescence intensity near the embedded objects was found to depend on the geometry and the refractive index difference between the object and the surrounding solution. The observed fluorescence intensity gradients do not reflect the fluorophore concentration in the solution. It is suggested to apply a Gaussian fit or smoothing to the observed fluorescence intensity gradient and use this as a basis to recover the fluorophore concentration in the proximity of the refractive index step change. The method requires that the reference and sample objects have the same geometry and refractive index. The best results were obtained when the sample objects were also used for reference since small differences such as uneven surfaces will result in a different extent of aberration.
 [DOI: 10.1117/1.JBO.21.12.126014]

Keywords: confocal laser scanning microscopy; refractive index; optical aberration; embedded object; polydimethylsiloxane.

Paper 160641TNR received Sep. 16, 2016; accepted for publication Nov. 28, 2016; published online Dec. 21, 2016.

Confocal laser scanning microscopy (CLSM) is widely applied in biological and biomedical sciences. While in many cases the objective is a localization of fluorescent species, some applications seek to quantify the concentration of fluorophores.[1–3] This proves less than straightforward in the proximity of an object with a refractive index (n) different from that of the surrounding medium. The refractive index mismatch introduces optical aberrations and blocks optical access to the objects of interest, resulting in the fluorescence intensity distribution not reflecting the fluorophore concentrations. Such situations can be observed inside polydimethylsiloxane (PDMS) channels used for microfluidics[4] or in hydrogels attached to optical fibers[5] where a vertical boundary between media with different refractive indices is present. This challenge can be circumvented in many cases by imaging only near the sample/coverslip interface, but if images from larger depths are required, the issue needs to be addressed differently. One of the options is to match the refractive index of the solution to that of the object, but due to the difficulty of achieving a perfect match, this merely reduces rather than eliminates the issue. Thus, it is common to image further from the object where the optical aberration due to index mismatch does not have an effect.[4] In some instances, this approach is not usable, such as in the case of hydrogels attached to optical fibers,[5,6] where the region of interest is in close proximity to the cylindrical glass fiber. The refractive index matching strategy may also introduce changes in other physical parameters, e.g., viscosity that is unwanted in certain applications.

The effects of mismatches in the refractive index along the optical axis have previously been reported.[7–13] These include mismatch between the sample medium and the lens immersion fluid or use of coverslips with thicknesses different from that calibrated for the objective lens. The result is a broadening and loss of axial symmetry in the point spread function (PSF), and a shift in the axial position of the maximum of the PSF (focal point). This spherical aberration causes a depth-dependent decrease in resolution and brightness and generates errors in quantitative measurements involving the axial dimension. Not only has the refractive index mismatch along the optical axis been studied and described, there are also various correcting procedures suggested.[14,15]

In the case of a lateral refractive index step change as considered here, the boundary is vertical and only a part of the illuminating cone and detected light is affected. This is illustrated in Fig. 1 using simple geometrical optics for light rays in the xz-plane [i.e., two-dimensional (2-D) illustration showing only a cross section of the illuminating cone of the objective]. The light rays not affected by the object are focused at the nominal focus position (NFP), which is the geometrical focus in a perfectly matched system. The part of the illuminating cone that passes through the object is reflected/refracted and not focused (at NFP or elsewhere). However, it can still contribute to the total illumination PSF (iPSF) and cause distortions to the unaffected part of the iPSF. Additionally, a fraction of the incident illumination undergoes total internal reflection inside the

*Address all correspondence to: Bjørn Torger Stokke, E-mail: bjorn.stokke@ntnu.no

1083-3668/2016/$25.00 © 2016 SPIE

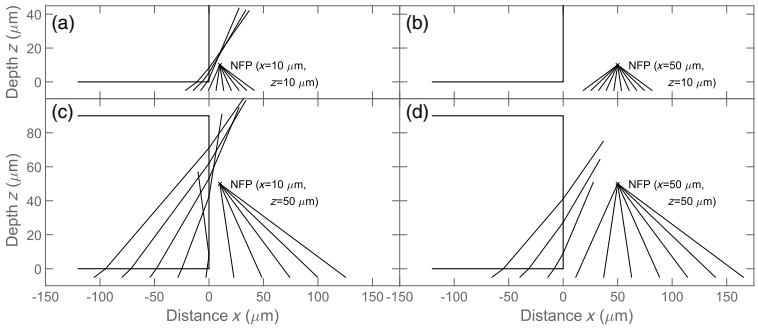

Fig. 1 Effect of refraction on the excitation light rays at four different scanning points (a–d) with NFP x- and z-coordinates being (10, 10), (50, 10), (10, 50) and (50, 50) μm, respectively. The image shows a 2-D ray optics scheme of light illuminating the sample. The refractive indices of the object and the solution are 1.50 and 1.33, respectively (for the wavelength of the depicted light rays). The half angle of the collected light is 64.5 deg, equivalent to a numerical aperture of 1.2, with a water immersion lens ($n = 1.33$ for the wavelength used). Assuming that the objective is corrected for the coverslip and immersion fluid, the refraction at these horizontal boundaries is not taken into account and thus not shown in the images.

object. The detection PSF is affected in a similar manner. Fluorescence emitted from NFP and passing though the object is rejected by the pinhole, thus further reducing the detected intensity, whereas emission from points other than NFP may reach the detector after being refracted by passing through the object.

The 2-D simulations (Fig. 1) indicate that the fraction of affected light increases with the focal plane z (distance from focal point to coverslip/sample interface), as well as with the decreasing lateral distance x from the refractive index boundary. The larger the solid angle taken up by the object as viewed from the focus toward the objective, the larger the fraction of light refracted and reflected, causing more severe spherical aberration. This introduces gradients in the detected fluorescence intensity both in the axial z-direction (as for sample/immersion mismatch) and in the lateral x-direction, thus making quantitative estimates of the concentration of the fluorophore not straightforward.

The following experimental data were acquired using glass cuboids (borosilicate glass, $n \approx 1.5230$, VWR), PDMS cuboids ($n \approx 1.41$[16]), and cleaved optical glass fibers ($n \approx 1.4436$ for the core, Huber-Suhner, cylindrical shape with diameter 125 μm; the n of the cladding are estimated to $n \approx 1.50$) as embedded objects. These objects were embedded in buffered aqueous solution (150 mM NaCl, 10 mM Tris, 1 mM EDTA) of Alexa Fluor 647-conjugated oligonucleotides ($n \approx 1.334$[17]). A polyacrylamide hydrogel attached to an optical fiber was also imaged. The refractive index of the hydrogel was calculated to be $n \approx 1.35$ using a linear expansion of n for water in the polymer concentration c_p and refractive index increment of $(dn/dc_p) = 0.165$ mL/g.[18] Images were acquired by a confocal laser scanning microscope (Leica TCS SP5) with a 63×, NA = 1.2 water immersion objective. The exciting wavelength was 633 nm and a bandpass filter of 655 to 709 nm was employed on the emission side. For cuboids, fluorescence intensity profiles perpendicular to the lateral edge were averaged. In the case of the cylinders (fibers), the profiles were averaged over [−25 deg, 25 deg] angle from the axis of the fiber.

The CLSM micrographs and the corresponding intensity profiles in the proximity of a glass cuboid immersed in a homogeneous fluorescent solution (Fig. 2) illustrate the depth and lateral dependence of the recorded fluorescence intensity. At depth $z = 0$ μm, the intensity of the detected fluorescence in the solution is constant, independent of the lateral distance.

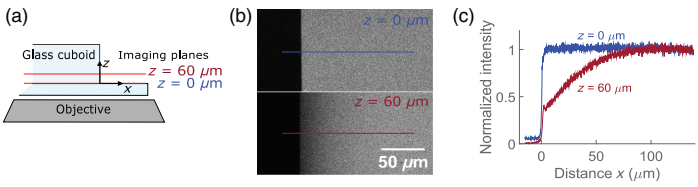

Fig. 2 (a) Schematics of the experimental setup for CLSM with a glass cuboid immersed in a homogeneous fluorescent solution, indicating also two different imaging planes. (b) CLSM images of a glass cuboid ($n = 1.52$) in a homogeneous fluorescent solution ($n = 1.334$) at depth $z = 0$ and 60 μm. The lines depict the location of the intensity profiles used for analysis. (c) Fluorescence intensity profiles at depths $z = 0$ and 60 μm perpendicular to the boundary. The profiles are an average of 200 profiles taken parallel to the lines in images from (b).

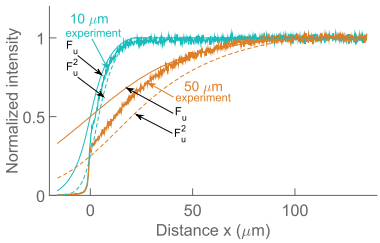

Fig. 3 Experimental fluorescence intensity profiles in the proximity of a vertical glass/solution interface extracted from CLSM images of a glass cuboid ($n = 1.52$) in a homogeneous fluorescent solution ($n = 1.334$). Normalized detected intensity as a function of distance x from the glass/solution interface is shown for NFP at depths z 10 (blue) and 50 μm (orange). The smooth lines show F_u for corresponding depths z. The dotted lines show F_u^2.

At depth 60 μm, there is a significant decrease in fluorescence depending on the lateral distance to the glass cuboid. The fluorescence loss extends ~70 μm laterally from the cuboid/solution interface and the intensity close to the interface is about one-third of the plateau intensity. The fluorescence intensity loss in the proximity of the boundary increases with the imaging depth z. Thus, the detected fluorescence intensity in the xz-image does not reflect the expected constant fluorophore concentration in the solution.

The fraction of the illuminating and detection cone that is passing through the object influences the extent of the aberration. In the first approximation, it can be assumed that only the fraction unaffected by the object contributes to the image formation. The fraction of the light cone that does not pass through a cuboid infinitely long in the y direction (the unaffected fraction F_u), depends on the lateral distance x and depth z as

$$F_u = 0.5 + \frac{0.5x}{\sin(\alpha)\sqrt{x^2 + z^2}}, \tag{1}$$

where x is the distance from the vertical refractive index boundary to the NFP, z is the distance from the coverslip/sample interface to the NFP (Fig. 1), and α is the half-angle of the collected rays from the NFP.

The fluorescence profiles recorded when imaging at depths z ranging from 0 to 70 μm, close to the glass cuboid, are compared with the F_u of a light cone for a cuboid infinitely long in the y direction calculated using Eq. (1) (Fig. 3). This model accounts for the illumination only, while in reality this effect would be observed both for the illumination and for the emitted fluorescence. Assuming that only light emitted from the NFP can pass a pinhole, the same fraction will pass through the object in the case of the emitted light as for the illumination light, hence a square of the F_u (F_u^2) should provide a better fit.

In this largely simplified geometrical model, none of the refracted light rays contributes to the PSF, which leads to large deviations from the experimental data. This error becomes larger with increasing depth z, as the fraction of affected light increases. Although this geometrical approach is too simplified to provide an accurate fit for the data, it illustrates the effect of the refractive index on the detected intensity and can identify the distance at which this effect will be observed for each depth z.

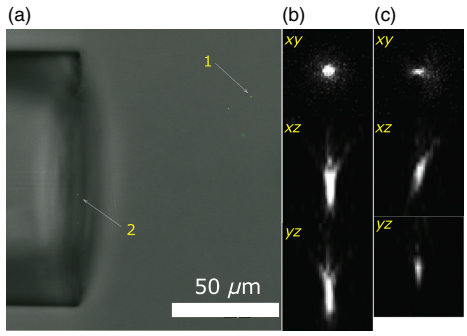

Fig. 4 Fluorescent PSF beads and a glass fiber cylinder immersed in a polyacrylamide gel. (a) The merged CLSM fluorescent and transmission image acquired 62 μm into the sample using the 63 × /1.2 NA water immersion lens. The slices in (b) and (c) show the fluorescence of the beads indicated by arrows 1 and 2 in (a), respectively. The xy-images show the maximum intensity projection (image size 6.29 × 6.17 μm), whereas the xz and yz images are slices across the center of the two beads [image size in (b) 6.29 × 7.36 μm and 6.17 × 7.36 μm for xz and yz, respectively, and in (c) 6.29 × 6.89 μm and 6.17 × 6.89 μm for xz and yz, respectively]. The voxel size is 121 × 121 × 462 nm.

The distorted PSFs were characterized based on acquisition of a z-stack of the glass fiber cylinder immersed in an acrylamide gel (10 wt. % acrylamide, 1 mol. % N-N-methylene-bisacrylamide, $n = 1.35$) with 170-nm green fluorescent subresolution beads (PS-Speck, P7220, from Invitrogen), using the 63× water immersion lens. The excitation wavelength was 488 nm and the fluorescence detected in the range 500 to 550 nm. The PSFs close to the coverslip (small z) and some distance (x in the range above 75 μm) from the fiber were not distorted (images not shown). For the PSF obtained at larger z, spherical aberration becomes more severe, particularly in the vicinity of the fiber where the light is refracted and reflected [Fig. 4(c)]. The xz orthogonal central slice and the xy-slice show PSF asymmetry and anisotropy. Also, loss in intensity is observed. The PSF far away from the fiber is distorted only in the z-direction because of the large imaging depth and slight refractive index mismatch between the sample and the immersion fluid.

Due to the presence of the lateral refractive index boundary, the PSF becomes asymmetrical and spatially variant both in the z and x directions. For the most accurate restoration of the concentration profiles within the image, a deconvolution using spatially variant PSFs should be applied. This is computationally demanding, and current algorithms only employ a z-variant PSF.[19,20] The available algorithms also restore the total intensity of the images, but they do not compensate for intensity lost outside of the sample volume. Since a significant part of the intensity is permanently lost due to the fiber, these algorithms would not restore the intensity. Deconvolution would also require the knowledge of the PSF at each point in space, either by measuring or by calculating it. However, the PSF becomes complicated as different light rays gain different phase shifts due to the refraction. Salter and Booth[21] have suggested a solution to a similar problem in laser manufacturing that consisted of modulating the phase of the laser to restore the PSF to its intended

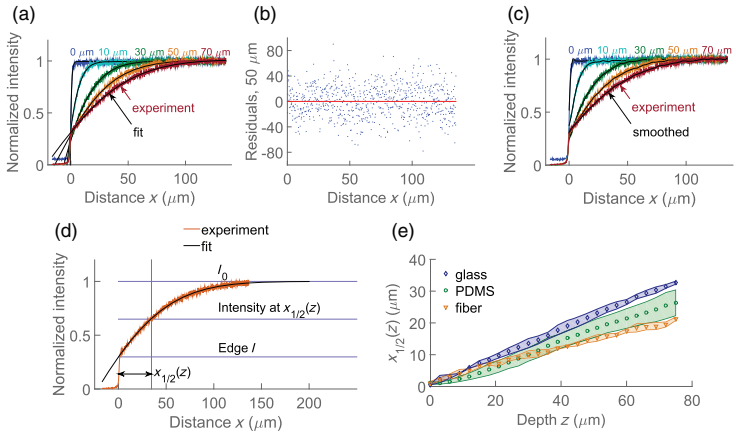

Fig. 5 (a) Experimental fluorescence intensity profiles in the proximity of a vertical glass/solution interface extracted from CLSM images of a glass cuboid ($n = 1.52$) in a homogeneous fluorescent solution ($n = 1.334$). Normalized detected intensity as a function of distance x from the glass/solution interface is shown for NFP at depths z varying from 0 μm (blue) up to 70 μm (red). Black lines indicating a fitted Gaussian. (b) Plot of residuals as a function of x for the fitting of profile at 50 μm in (a). (c) Experimental fluorescence profile as in (a) and smoothed profiles using a Savitzky–Golay filter. (d) $x_{1/2}(z)$ (see text for details) for $z = 50$ μm. (c) $x_{1/2}(z)$ for fibers ($n = 1.50$ for cladding), PDMS ($n = 1.41$) and glass cuboids ($n = 1.52$) at different depths. The markers show the average values of four measurements for fiber and PDMS and two measurements for glass cuboid and the shaded areas depict the standard deviations. The online version depicts the plots in color.

shape and thereby avoid aberration. This approach can also, in principle, be implemented in microscopy to compensate for axial refractive index mismatch, although phase modulation is not readily available for commercial microscopes. In our case, due to the light being refracted twice by the object, the computations become even more complicated.

Instead of a deconvolution, we propose to apply an empirical scaling factor to restore the lost intensity although not the resolution. To recover the concentration profiles from a sample image taken in the proximity of an object with different n, a reference image is taken of the same object (or similar object with the same geometry and n) in a homogeneous solution. The intensity profile from the reference image is fitted to a suitable function (for simpler geometries, where applicable) or simply smoothed; acquiring a reference profile $\mathrm{Ref}(x, z)$. The sample profile is then multiplied by the scaling factor $1/\mathrm{Ref}(x, z)$ to recover the concentration gradients.

For the geometries presented here (cuboids and cylinders), the profiles were fitted with a Gaussian curve. The Gaussian was selected because it is the simplest function that adequately describes the experimental data, and causes minimal trends in the residuals as a function of x.

The fitting function has the following form:

$$I(x) = I_0 - I_{\mathrm{amp}} e^{-\frac{(x-x_c)^2}{x_d^2}}, \tag{2}$$

where I is the intensity at distance x along the profile, I_0 is the plateau intensity in the unaberrated case, I_{amp} is the height of the peak, x_c is the center of the peak, and x_d gives information about the width of the peak.

The adjusted R^2 values for each fit were calculated. For cuboid geometries, the values ranged between 0.980 and 0.996, for cylinders between 0.940 and 0.960. For both geometries the R^2 values were lower for fitting at $z = 0$, with R^2 0.880 to 0.890. These profiles resemble the step change the most and it is usually not necessary to use the correction for them. In Fig. 5(b) an example of a plot of residuals is shown, with no apparent trends.

To compare the effects for different materials (different refractive indices n) and different geometries (glass cuboid, end of glass cylinder-fiber) the lateral distance to the half maximum intensity was used. Half maximum intensity [Fig. 5(d)] is the average of the intensity at the boundary and the plateau intensity of the solution in the unaberrated case, located at $x_{1/2}(z)$ = distance to half maximum. Figure 5(e) shows the plot of the distance to half maximum intensity for glass cuboids, glass fibers, and PDMS cuboids. The relatively large standard deviations are partly due to the unevenness of the object edges which was largest for the PDMS cuboid. The parameter $x_{1/2}(z)$ is larger for glass than for PDMS cuboids at a given z which could be due to a larger refractive index difference between the glass and solution than between the PDMS and solution. The $x_{1/2}(z)$ parameter for the fiber is expected to differ from that of the cuboid due to the difference in geometry as well as n.

To test the applicability of the proposed restoration procedure using the scaling factor $1/\mathrm{Ref}(x, z)$, several sample objects (Fig. 6) in a homogeneous solution were imaged and intensity profiles from the images were restored using data from reference objects of the same n and geometry (in this case the reference object and sample object were not the same). Since the samples

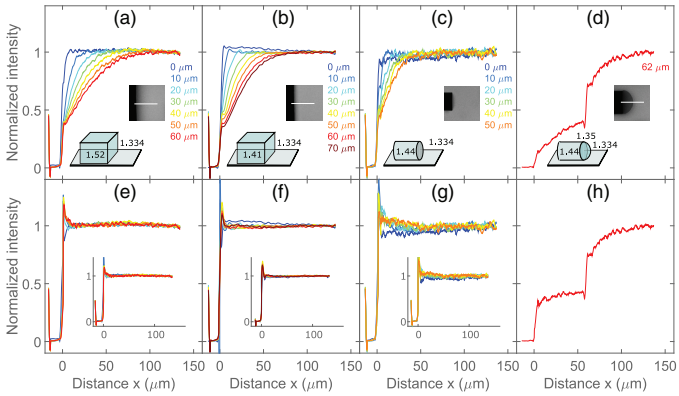

Fig. 6 Fluorescence restoration using Gaussian fitting and smoothing. Examples of unrestored (a–d) and restored (e–h) profiles along the white lines shown in the CLSM image (205 μm × 205 μm) for different materials (refractive indices indicated) and geometries. The profiles restored using Gaussian fitting are the main ones, while the restored intensities using the smoothing are shown as insets (e–g). (a, e) Glass cuboid, (b, f) PDMS cuboid, (c, g) glass fiber cylinder, and a (d, h) glass fiber with a polyacrylamide PAM hydrogel at its end. Each object is immersed in a homogeneous fluorescent solution ($n = 1.334$). The intensity profiles at various depths are plotted individually and normalized before correction and after the correction. In the case of the hydrogel, the reference object was a fiber without a hydrogel. Optical effects due to refraction at hydrogel/solution interface were not taken into account. The online version depicts the plots in color.

were immersed in homogeneous solutions, there is an x-independent concentration of the fluorophore which should be recovered by the proposed restoration procedure. The scaling was done using both Gaussian fitting and smoothing with a Savitzky–Golay filter. The restored profiles are nearly constant (Fig. 6), but deviations are observed near the edge of the object. This is mostly due to the restoration process being sensitive to misalignments in the sample and reference image depths, as well as in the x-position of the object edge. Both the z position of the imaging plane inside the object and the exact position of the edge are difficult to identify precisely due to the blurring at the boundaries, which occurs as a result of the nonzero confocal volume.

Figure 6 also shows the restoration procedure applied to a polyacrylamide gel bound to the end of the glass fiber. Here the reference image was of a fiber in a solution only. This means that the refractive index difference for the reference object (fiber/solution) differs from that of the sample object (fiber/gel) and is not accurate. However, the correction still shows that what appeared to be a concentration gradient inside the gel in the initial image is an imaging aberration due to the presence of the fiber. There is also an observed intensity loss in the solution in the proximity of the gel/solution interface. This loss is not corrected for in the restoration procedure, suggesting that a similar aberration process takes place at this interface.

Optical aberration occurs whenever light crosses a refractive index boundary. Direct quantitative concentration measurements are impossible near such boundaries due to the observed fluorescence gradient. The extent of this aberration increases with imaging depth (distance from coverslip/sample boundary) and with the proximity to the boundary. While the loss due to aberration is negligible for images recorded close to the coverslip/sample interface, the effect can reduce observed intensity to one-third at larger depths. If it is not possible to image at a sufficient distance from the boundary, we show that using a Gaussian fitting for a reference object allows restoration to recover fluorescence and detect true concentration gradients near simple geometries such as a cuboid or a base of a cylinder.

Disclosures

The authors have no financial conflicts to declare.

References

1. D. Fairbairn, K. L. O'Neill, and M. D. Standing, "Application of confocal laser scanning microscopy to analysis of H_2O_2-induced DNA damage in human cells," *Scanning* **15**(3), 136–139 (1993).
2. H. Kawai et al., "Direct measurement of doxorubicin concentration in the intact, living single cancer cell during hyperthermia," *Cancer* **79**(2), 214–219 (1997).
3. J. W. Lampe et al., "Imaging macromolecular interactions at an interface," *Langmuir* **26**(4), 2452–2459 (2010).
4. A. D. Stroock et al., "Chaotic mixer for microchannels," *Science* **295**(5555), 647–651 (2002).
5. K. Gawel, M. Gao, and B. T. Stokke, "Impregnation of weakly charged anionic microhydrogels with cationic polyelectrolytes and their swelling properties monitored by a high resolution interferometric technique. Transformation from a polyelectrolyte to polyampholyte hydrogel," *Eur. Polym. J.* **48**(11), 1949–1959 (2012).
6. M. Gao, K. Gawel, and B. T. Stokke, "High resolution interferometry as a tool for characterization of swelling of weakly charged hydrogels subjected to amphiphile and cyclodextrin exposure," *J. Colloid Interface Sci.* **390**(1), 282–290 (2013).
7. A. Egner and S. W. Hell, "Aberrations in confocal and multi-photon fluorescence microscopy induced by refractive index mismatch," in *Handbook of Biological Confocal Microscopy*, J. B. Pawley, Ed., pp. 404–413, Springer, New York (2006).
8. S. Hell et al., "Aberrations in confocal fluorescence microscopy induced by mismatches in refractive index," *J. Microsc.* **169**(3), 391–405 (1993).
9. R. Rottenfusser, C. E. Steenerson, and M. W. Davidson, "Focus depth and spherical aberration. Interactive tutorials, basic microscopy," http://

www.zeiss.com/microscopy/en_de/solutions/reference/all-tutorials/basic-microscopy/focus-depth-and-spherical-aberration.html (12 December 2016).
10. E. H. Keller, "Objective lenses for confocal microscopy," in *Handbook of Biological Confocal Microscopy*, J. B. Pawley, Ed., pp. 145–161, Springer, New York (2006).
11. M. J. Nasse and J. C. Woehl, "Realistic modeling of the illumination point spread function in confocal scanning optical microscopy," *J. Opt. Soc. Am. A* **27**(2), 295–302 (2010).
12. Y. Deng and J. W. Shaevitz, "Effect of aberration on height calibration in three-dimensional localization-based microscopy and particle tracking," *Appl. Opt.* **48**(10), 1886–1890 (2009).
13. A. Diaspro, F. Federici, and M. Robello, "Influence of refractive-index mismatch in high-resolution three-dimensional confocal microscopy," *Appl. Opt.* **41**(4), 685–690 (2002).
14. H. W. Yoo et al., "Automated spherical aberration correction in scanning confocal microscopy," *Rev. Sci. Instrum.* **85**(12), 123706 (2014).
15. M. J. Booth, M. A. A. Neil, and T. Wilson, "Aberration correction for confocal imaging in refractive-index-mismatched media," *J. Microsc.* **192**(2), 90–98 (1998).
16. I. Martinček, I. Turek, and N. Tarjányi, "Effect of boundary on refractive index of PDMS," *Opt. Mater. Express* **4**(10), 1997–2005 (2014).
17. W. M. Haynes Ed., "Concentrative properties of aqueous solutions: density, refractive index, freezing point depression, and viscosity," in *CRC Handbook of Chemistry and Physics*, 97th ed., CRC Press/Taylor & Francis, Boca Raton, Florida (2016).
18. J. François et al., "Polyacrylamide in water: molecular weight dependence of $\langle R2 \rangle$ and $[\eta]$ and the problem of the excluded volume exponent," *Polymer* **20**(8), 969–975 (1979).
19. S. B. Hadj and L. Blanc-Féraud, *Restoration Method for Spatially Variant Blurred Images*, RR-7654, INRIA (2011).
20. S. B. Hadj et al., "Modeling and removing depth variant blur in 3D fluorescence microscopy," in *IEEE Int. Conf. on Acoustics, Speech and Signal Processing (ICASSP 2012)* (2012).
21. P. S. Salter and M. J. Booth, "Focusing over the edge: adaptive subsurface laser fabrication up to the sample face," *Opt. Express* **20**(18), 19978–19989 (2012).

Biographies for the authors are not available.

Paper III

BioMACROMOLECULES

pubs.acs.org/Biomac Article

Toehold Length of Target ssDNA Affects Its Reaction-Diffusion Behavior in DNA-Responsive DNA-*co*-Acrylamide Hydrogels

Eleonóra Parelius Jonášová, Astrid Bjørkøy, and Bjørn Torger Stokke*

Cite This: https://dx.doi.org/10.1021/acs.biomac.9b01515 Read Online

ABSTRACT: In the present study, we expand on the understanding of hydrogels with embedded deoxyribonucleic acid (DNA) cross-links, from the overall swelling to characterization of processes that precede the swelling. The hydrogels respond to target DNA strands because of a toehold-mediated strand displacement reaction in which the target strand binds to and opens the dsDNA cross-link. The spatiotemporal evolution of the diffusing target ssDNA was determined using confocal laser scanning microscopy (CLSM). The concentration profiles revealed diverse partitioning of the target DNA inside the hydrogel as compared with the immersing solution: excluding a nonbinding DNA, while accumulating a binding target. The data show that a longer toehold results in faster cross-link opening but reduced diffusion of the target, thus resulting in only a moderate increase in the overall swelling rate. The parameters obtained by fitting the data using a reaction-diffusion model were discussed in view of the molecular parameters of the target ssDNA and hydrogels.

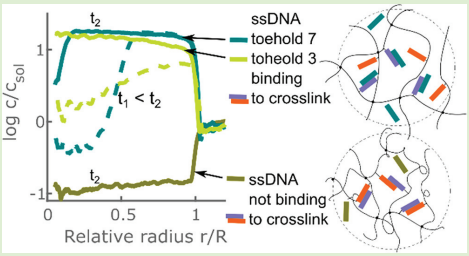

INTRODUCTION

DNA and DNA-hybrid hydrogels are responsive hydrogels where the DNA in the hydrogel and its interactions with the components in immersing solution are key in transforming molecular changes to altered hydrogel state.[1−4] The unique appeal of incorporating DNA in a hydrogel is due to the high specificity of the complementary base pairing in the hybridization reaction. The versatility and tunability lies in the combination of the large number of possible unique base pair sequences accessible by custom-design and high degree of control over the molecule's higher-order structure and its interactions with other DNA molecules or other types of molecules through potential aptamer functionality.[5] The rapidly growing field of DNA nanotechnology is taking advantage of these properties that make DNA a unique building block.[6−11]

Conjugation of DNA within hydrogels allows translation of the specific and controllable interactions on molecular level to the micro- or even macro-level of the hydrogel. The level of control, specificity, and versatility of DNA as a sensing moiety, paired with the hydrogels' tunability, biocompatibility, and responsiveness at various length scales, underpin the potential of DNA-hybrid hydrogels' application within biosensing,[12−21] diagnostics,[22] targeted drug delivery[23−25] as well as cell culturing,[26] scaffolds in tissue engineering,[27,28] and various soft devices.[29,30]

We have previously developed a sensor platform based on hydrogels integrated on an optical fiber for interferometric readout of changes in the optical length with 2 nm resolution for hydrogels with dimensions of about 50 μm.[31] This setup was used to study DNA-polyacrylamide hydrogels applying a particular molecular design first reported by Nagahara and Matsuda[32] in 1996 that respond by swelling to the presence of a specific oligonucleotide.[33,34] The recognition is supported by partially double stranded DNA (dsDNA) cross-links within the hydrogel that bind the target oligonucleotide and subsequent toehold-mediated strand displacement. In this process, the invading single-stranded DNA (the target ssDNA) will hybridize with one of the strands (the sensing strand) in the DNA cross-link after binding to a complementary region called the toehold. By branch migration, a back and forth migration of the junction point where the three strands meet, the invading strand is displacing the complementary oligonucleotide in the DNA duplex called the blocking strand. Eventually, the blocking strand is completely displaced, and a more stable DNA duplex is formed. Completion of the strand displacement leads to dissociation of the dsDNA link between network strands, thus reducing the number of cross-links and facilitating transformation of the processes at the molecular level to a (local) change in the swelling state. The overall swelling rates have been reported for various bp-lengths of complementary

Special Issue: Anselme Payen Award Special Issue

Received: November 4, 2019
Revised: December 19, 2019
Published: December 30, 2019

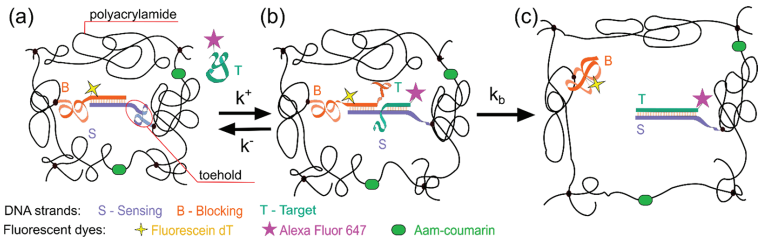

Figure 1. Schematic illustration of the DNA-polyacrylamide hydrogel network and the process of toehold-mediated strand displacement. The target DNA (T) binds to (rate constant k^+) and dissociates (rate constant k^-) from the hybridized sensing-blocking SB dsDNA in the hydrogels (a,b), and a bound target DNA undergoes branch migration with a rate k_b to dissociate the SB duplex (b,c). Three different types of gels were prepared: SB hydrogels with no dyes attached to the network or network-bound DNA, CoumSB hydrogels containing only Aam-coumarin and SBF hydrogels only labeled with Fluorescein dT on B strand.

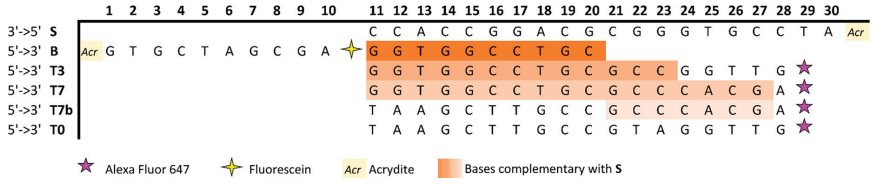

Figure 2. DNA sequences of the sensing S, blocking B and target strands T0, T3, T7, and T7b. The positions of the fluorescent dyes and the acrydite groups are shown, and the complementary regions between S and B, and S and the targets are highlighted.

dsDNA regions as well as toehold regions for the target strands diffusing into the hydrogels.[34]

The interferometric readout platform provides high-resolution information on the swelling of the hydrogels as a response to the diffusing target DNA as an average over the changes along the optical path, but it does not provide information on localized swelling. In the present work, we employ fluorescent labeling and confocal laser scanning microscopy (CLSM) to determine the spatiotemporal ssDNA target apparent diffusion through the gel and how it is affected by the length of the toehold region. This approach provides insight into the cascading processes, starting by the attachment of invading ssDNA, the opening of a DNA crosslink in the hydrogel, and ending with a change in the hydrogel volume. The target can be described as undergoing a reaction-diffusion process, where its net transport is the result of the interplay between its diffusion inside the hydrogel and the binding and dissociation to and from the hydrogel-bound dsDNA. The translation mechanism of the change from the molecular DNA level to the hydrogel level determines the overall response time of the system and thus is of interest in most applications. A thorough understanding of the processes preceding the swelling is necessary in order to better design and tune the kinetics of the gel swelling to the needs of each application.

■ MATERIALS AND METHODS

Materials. Acrylamide ≥99% (Aam), *N,N′*-methylenebis-(acrylamide) ≥99.5% (Bis), squalane oil, dimethyl sulfoxide (DMSO), 3-(trimethoxysilyl) propyl methacrylate 98%, 1-hydroxycyclohexyl phenyl ketone 99% (HCPK), 2-amino-2-hydroxymethyl-propane-1,3-diol (Tris), and 7-[4-(trifluoromethyl)coumarin]-acrylamide (Aam-coumarin) were purchased from Sigma-Aldrich; ethylenediaminetetraacetic acid (EDTA) and sodium chloride (NaCl) were obtained from VWR. Single-stranded DNA oligonucleotides with custom specified base pair (bp) sequence and functionalized with an acrydite group, both unlabeled and fluorescently labeled at specific bp, were obtained from Integrated DNA Technologies (IDT, Coralville, U.S.A.). All materials were used without further purification. Deionized water with a resistivity of 18.2 MΩ cm (Millipore Milli-Q) was used throughout.

Hydrogel Design. The quasi-hemispherical shaped hydrogels were prepared at the end of optical fibers to support the interferometric length measurement.[31] The responsive hydrogels consist of a covalently cross-linked polyacrylamide network (10 wt % acrylamide, 0.6 mol % Bis) with additional partially double-stranded DNA cross-links (0.2 mol %) (Figure 1). In addition, pure polyacrylamide hydrogels PolyAam08 without DNA, but with cross-linking density equivalent to that of DNA-hydrogels (0.8 mol % Bis), were prepared.

The hybridized sensing strand (S) and blocking strand (B) are covalently attached to the network, forming the dsDNA cross-links. S and B oligonucleotides were obtained with an acrydite group at 5′-ends to allow covalent bonding with the polyacrylamide network. The S and B strands were designed with 20 bases with a 10-base complementary region at their 3′ ends, which is referred to as the blocking region (Figure 2). The hybridized regions were designed with a high GC content to ensure a melting temperature above the ambient temperature of 22 °C used in the experiments. The melting temperature of the SB duplex was estimated to be 48.9 °C using online an oligonucleotide properties calculator OligoCalc.[35]

The DNA cross-link can be opened by a target T strand in a toehold-mediated strand displacement process (Figures 1, 3).

The hydrogels were immersed in aqueous buffer solutions of 20 μM target ssDNA of either of the targets T0, T3, T7, or T7b (each consisting of 18 bases) (Figure 2 and 3). T3 and T7 strands are complementary to the sensing strand S for the same bases as B (the blocking region), as well as an additional complementary region (toehold) of 3 and 7 bases, respectively, while T7b is only complementary to S on a toehold region of 7 bases. T0 is designed to be noncomplementary to S and does not bind.

https://dx.doi.org/10.1021/acs.biomac.9b01515
Biomacromolecules XXXX, XXX, XXX−XXX

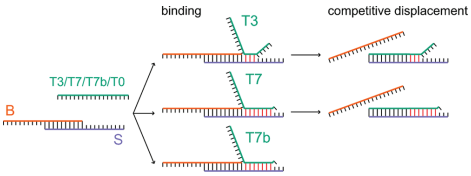

Figure 3. Schematics of the interactions (binding and competitive toehold-mediated strand displacement) between the dsDNA cross-link SB and various target strands T3, T7, T7b, and T0. The bonds in the complementary region of the toeholds are shown in red.

Labeling Strategy. Fluorescent dyes were used to monitor the processes taking place before and during the swelling of the hydrogel. The hydrogels were immersed in aqueous buffer solutions with target ssDNA (T0, T3, T7, or T7b) where 10% of the target ssDNA were labeled with Alexa Fluor 647 at their 3′ ends (Figure 2) to be used as a reporting molecule when visualizing their diffusion and binding within the hydrogel.

In addition to fluorescent labeling of the target strands, several strategies involving labeling of the hydrogel (polyacrylamide or hydrogel-bound DNA) were explored with the intention of using this as internal reference or to gain more understanding of the underlying molecular processes. While these strategies were not successful (see SI: Use of FRET for monitoring of cross-link opening, Figures S1 and S2), we included information on the labeled hydrogels alongside the unlabeled ones to report on the observed effects of fluorescent dye incorporation.

Three different types of hydrogels with respect to presence of fluorescent dyes were prepared. Hydrogels denoted SB carried no fluorescent dyes; CoumSB hydrogels included a coumarin-labeled acrylamide incorporated in the polymer network (at concentration 0.05 mol % of acrylamide monomer); and SBF hydrogels had 10% of the blocking strands labeled with Fluorescein dT.

Pregel and Target DNA Solutions. Pregel solutions were prepared by dissolving 10 wt % Aam (optionally also including 0.05 mol % Aam-coumarin), 0.6 mol % Bis, 0.2 mol % dsDNA (SB), and 0.13 mol % HCPK in buffer (10 mM Tris, 1 mM EDTA and 150 mM NaCl, adjusted to pH 7.5). HCPK and Aam-coumarin were first dissolved in DMSO to the concentrations of 0.1 and 0.11 M, respectively, before being added to the pregel solution. SBF hydrogels were prepared with 10% of the B oligonucleotides labeled with Fluorescein dT. After preparing the pregel solution, a minimum of 3 h of passive mixing was allowed, to ensure the formation of SB duplexes. PolyAam08 hydrogels were prepared without DNA, but with 10 wt % Aam and 0.8 mol % Bis, that is, identical total cross-linker density to the DNA hydrogels (where both Bis and DNA serve as cross-linkers).

Stock solutions of target ssDNA were prepared by dissolving the T0, T3, T7, or T7b strands in aqueous buffer (10 mM Tris, 1 mM EDTA, and 150 mM NaCl, adjusted to pH 7.5) to a concentration of 60 μM. The target stock solutions were prepared with 10% Alexa Fluor 647 labeled target oligonucleotides.

All solutions were stored at −18 °C.

Fiber Preparation. The optical fibers (SMF-28-J9 from ThorLabs, diameter without coating 125 μm) were first stripped of the coating, and the ends were cut to obtain a flat and even surface (cutter: Fitel model S323, Furukawa Electric Co. Ltd.). After cleaning with ethanol, the ends were treated with 0.1 M HCl solution for 20 min and cleaned with ethanol again. Then the fiber ends were soaked for 15 min in a 2 vol % solution of 3-(trimethoxysilyl) propyl methacrylate dissolved in degassed MiliQ water at pH 3.5. The methacrylated fibers were again cleaned with ethanol and with duct tape to remove dust from the end face. The silanization procedure resulted in surface-bound methacrylate groups to ensure covalent linking of the acrylamide during polymerization.

Gel Preparation. A small amount of the pregel solution (∼0.3 nL) was deposited at the end face of an optical fiber immersed in a squalane oil droplet and polymerized using UV-light. The squalane oil was saturated with HCPK (2.6 mg/mL). The oil solution was prepared at least 2 h before polymerization, kept in the dark and on constant stirring and used for up to 1 week.

A small aliquot of the pregel solution was manually deposited on the end of the optical fiber using a pipet as aided by inspection through a stereo microscope. Polymerization was initiated using a UV light from a UV lamp (fiber coupled LED UV source M340F3, nominal wavelength 340 nm, ThorLabs, or Dymax blue wave, 50W) for 5 min.

Interferometry. The end of the fiber with the hydrogel was inserted into an Eppendorf tube containing 200 μL of buffer solution (10 mM Tris, 1 mM EDTA and 150 mM NaCl, adjusted to pH 7.5) and left to equilibrate for at least an hour. Then 100 μL of the stock target solution (60 μM target DNA) was added to obtain the final target solution (20 μM target DNA, of which 10% fluorescently

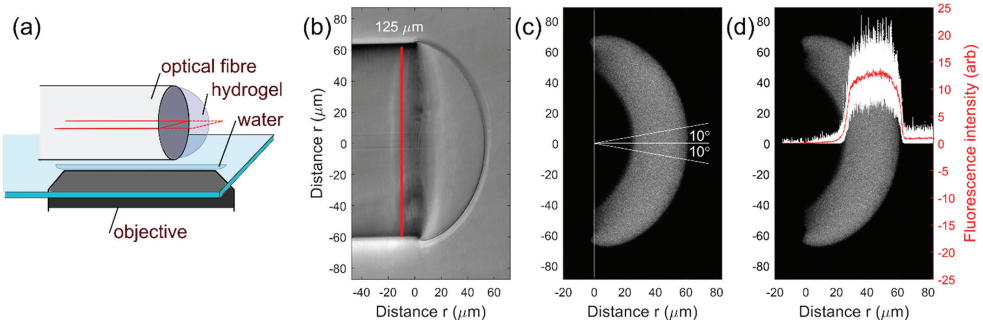

Figure 4. Acquiring intensity profiles from confocal micrographs. (a) Schematics of an optical fiber with a hydrogel attached to its end face as it is imaged using confocal laser scanning microscopy. Fluorescence micrographs were acquired at a plane through the middle of the hydrogel, at a 62 μm depth, shown in red. (b) Transmitted light image of a hydrogel and the fiber end face. (c) Micrograph showing the fluorescence acquired from Alexa Fluor 647 on target strand T7. The image is showing an intermediate state during the swelling and is acquired 35 min after gel being immersed in the target solution. The distribution of target T7 in the particular gel reached equilibrium at 70 min. The lines depict the angle within which intensity profiles are extracted. (d) The extracted individual fluorescence profiles from panel c are shown in white and their average in red overlaid the fluorescence micrograph of the hydrogel. The fiber end face is located at $r = 0$.

https://dx.doi.org/10.1021/acs.biomac.9b01515
Biomacromolecules XXXX, XXX, XXX−XXX

labeled, pH 7.5, 150 mM NaCl). The monitoring of the total gel length along the axis and its changes was performed using the interferometric setup, as described in detail elsewhere.[31] Briefly, a light wave (wavelength range 1530−1560 nm) is sent through the fiber and along the axis of the hydrogel and light reflected from the fiber-hydrogel and hydrogel−solution interfaces is detected. The gel is a micro Fabry−Perot cavity and the physical length of the hydrogel R (precision 1 μm) is determined by the free spectral range of the cavity. The phase change of the interference signal is used to determine changes in the length of the hydrogel ΔR that is due to changes in the swelling (precision 2 nm). The data logging started 90 s prior to the addition of target strands. The data was recorded every second for up to 150 min.

Using the initial size $R_0 = R(t = 0)$, ($t = 0$ referring to addition of target stock solution to the immersing aqueous buffer) and the change in size of the hydrogel ΔR, relative swelling was calculated:

$$R\% = \Delta R/R_0 \tag{1}$$

Confocal Laser Scanning Microscopy. The end of the fiber with the covalently attached hydrogel was pinched off using tweezers and glued to the bottom of a Glass Bottom Microwell Dish (P35G-1.5-10-C) from MatTek. Then 200 μL of the buffer solution (10 mM Tris, 1 mM EDTA and 150 mM NaCl, adjusted to pH 7.5) was added, and the gel was left to equilibrate for at least 1 h before the addition of the target stock solution.

The final target solutions (20 μM target DNA, with 10% fluorescently labeled strands, pH 7.5, and 150 mM NaCl) were prepared immediately prior to CLSM time lapse imaging by adding 100 μL of target stock solutions (60 μM target DNA) to the buffer solution equilibrating the gel. Time lapse imaging of the gels was performed at 22 °C using a Confocal Laser Scanning Microscope (Zeiss LSM800) with a 40×, NA = 1.2 water immersion objective (optical slice thickness of 0.9 μm). The imaging started 30−40 s after adding the stock target solution, and a micrograph was acquired every 60 s for up to 4 h. The excitation wavelengths were 640, 488, and 405 nm for Alexa Fluor 647, Fluorescein dT, and Aam-coumarin, respectively. Bandpass filters of 650−700, 500−550, and 400−600 nm were employed on the emission side to capture the fluorescence from Alexa Fluor 647, Fluorescein dT, and Aam-coumarin, respectively.

Acquiring Fluorescence Intensity Profiles from CLSM Micrographs. Custom scripts in Matlab R2017a (Mathworks) were developed for analysis and visualization of fluorescence intensity from the time lapse CLSM micrographs. Fluorescence intensity profiles were first extracted from the DNA hydrogel micrographs over several lines and averaged (Figure 4 showing a representative hydrogel of length 60 μm). The profiles used as basis for the averaging were acquired from a micrograph in a plane parallel to the coverglass and the fiber axis (core) (shown in red in Figure 4a). Averaged intensity profiles were extracted from a circular sector with a central angle of 20°. A profile was acquired every half a degree (Figure 4c). A plane rather than a cone was chosen for practical reasons and because of possible depth-dependent loss of fluorescence due to absorption and refraction. The averaging procedure assumes a spherical geometry; however, the hydrogels are not perfectly spherical. To minimize the resulting error, the averaging angle was restricted to 20°.

Relationship between Measured Fluorescence Intensity and Concentration. *Partitioning of Nonbinding Oligonucleotide T0 in DNA-Hydrogels.* The partition coefficient K_i of a solute i is defined as a ratio of its concentration in the gel c_{gel} and in the solution c_{sol} at equilibrium:

$$K_i = \frac{C_{gel}}{C_{sol}} \tag{2}$$

This partitioning is governed by equal chemical potential of the solute in the two phases. In addition to size effects, the partitioning is dependent on interactions between the hydrogel and the solute and thus is influenced by the properties of both. If these interactions are independent, they can be separated into individual contributions to the partition coefficient:[36]

$$\ln K_i = \ln K_{i,el} + \ln K_{i,hphob} + \ln K_{i,biosp} + \ln K_{i,size} + \ln K_{i,conf} + \ln K_{i,o} \tag{3}$$

where el, hphob, biosp, size, conf, and o denote, respectively, electrostatic, hydrophobic, biospecific affinity, size-related, conformational effects, and other interactions.

Fluorescence Intensity in the Proximity of the Fiber. Estimates of relative concentrations of the target T ($I_{TX/T0}$), $X = 3$ or 7, from the experimentally determined fluorescence intensity were obtained considering the effect of optical aberrations due to refraction caused by the presence of a glass fiber in the near vicinity of the hydrogel.[37] Previously, the loss of fluorescence due to the fiber was observed to extend up to approximately 50 μm from the end face of the fiber into the solution.[37] Assuming this is unchanged by the presence of the hydrogel, the ratio between the fluorescence intensity inside the hydrogel 60 μm from the end of the fiber and the fluorescence intensity of the surrounding solution reflects the ratio of the target concentrations in these domains.

The fluorescence intensity inside the hydrogel can also be reduced because of increased absorption as well as refractive index difference between the hydrogel and the immersing solution used during microscopic imaging. However, we observed a corresponding decrease in fluorescence inside the gel compared with the solution also when imaging in a plane closer to the coverglass, suggesting no significant effect from absorption and refractive index mismatch, which means that the decrease in fluorescence is mostly due to partitioning and the presence of the fiber.

On the basis of these assumptions, we used the ratio between the intensity inside the hydrogel at 60 μm from the end face and in the surrounding solution as the partitioning coefficient, that is, assuming that the ratio of fluorescence intensities of the target DNA in the solution and in the hydrogel at 60 μm from the fiber reflects the ratio of the corresponding concentrations.

The shape of the intensity profiles within the hydrogel is distorted due to aforementioned presence of the glass fiber and does not reflect a real decrease in concentration in the vicinity of the fiber. This was corrected for by using a reference profile that was obtained by immersing the hydrogel in a solution of a nonbinding target T0.[37] The averaged intensity (I_{TX}) profiles to be corrected were smoothed using a Savitzky−Golay filter, normalized so that the intensity of the surrounding solution is 1 and divided by smoothed and normalized (to maximum intensity in hydrogel being 1) reference profiles (Figure 5).

The alternative correction method employing Aam-coumarin as an internal reference yielded relative concentration profiles similarly resembling a more appropriate distribution (Figure S1). However, the correction based on Aam-coumarin was not employed further because of a possible effect of the coumarin dye on the partitioning of the target DNA (see below) and because of observed dye-clustering.

Parameter Estimation of the Spatiotemporal Profiles. Finally, the relative concentration profiles $I_{TX/T0}$ were fitted to an error function to obtain empirical parameters reflecting the spatiotemporal evolution of the target DNA concentration profiles in the hydrogels. An error function was chosen as this is derived from a diffusion process and in the present case was found to fit the observed transitions in concentration (in the following referred to as wavefront). Only the parts of the profiles that were inside the gel, the wave propagating toward the fiber end face, were used for the fitting (Figure 6). The fitting function has the following form:

$$F(r) = A\,\mathrm{erf}\left(\frac{r - r_0}{\sigma\sqrt{2}}\right) + C \tag{4}$$

where r is the distance from the fiber end face along the axis of the hydrogel, A is half of the height of the wavefront, C is the height of the wavefront midpoint above 0, r_0 is the distance from fiber end face to

https://dx.doi.org/10.1021/acs.biomac.9b01515
Biomacromolecules XXXX, XXX, XXX−XXX

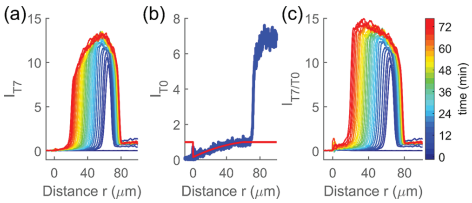

Figure 5. Correcting the intensity profiles for the optical effect caused by the presence of the fiber. (a) Profiles showing the fluorescence intensity acquired from Alexa Fluor 647 attached to T7 strand (I_{T7}), smoothed and normalized such that the intensity of the fluorescence of the free solution is 1. A profile is shown for every 3rd minute after addition of the target to the immersing solution. The colorbar specifies for each profile its time point after addition of the target. (b) In blue, the equilibrium intensity profile of the nonbinding target T0 (I_{T0}) inside (r less than 70 μm) and outside a hydrogel, smoothed and normalized so that the maximum intensity within the hydrogel is 1. In red, a second-degree polynomial fit to the part of the profile within the hydrogel. (c) Intensity profiles I_{T7} from a) divided by a reference profile acquired from T0 (as shown in red in panel b) to obtain the corrected relative intensity (i.e., estimated relative concentration $I_{T7/T0}$). The fiber end face is located at $r = 0$.

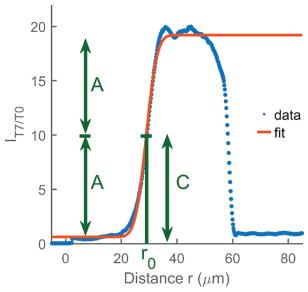

Figure 6. Fitting of the experimental concentration wavefront that is propagating toward the fiber end face to an error function (fiber end face at $r = 0$). Relative concentration profile $I_{T7/T0}$ normalized to the intensity of the surrounding solution (blue curve) along with the fit to error function (red curve).

the wavefront midpoint, and σ relates to the width of the wavefront; and erf denotes a standard error function of the form

$$\mathrm{erf}(x) = \frac{2}{\sqrt{\pi}} \int_0^x e^{-t^2} \mathrm{d}t \tag{5}$$

The fitted function was also differentiated analytically at the wavefront midpoint $r = r_0$ to obtain the value of the steepest slope, reflecting the largest concentration gradient of the target T diffusing into the hydrogel. This parameter was calculated as

$$\left.\frac{\mathrm{d}I_{T/T0}}{\mathrm{d}r}\right|_{r=r_0} = \left.\frac{\mathrm{d}F(r)}{\mathrm{d}r}\right|_{r=r_0} = \frac{\sqrt{2}A}{\sqrt{\pi}\sigma} \tag{6}$$

The size $R(t)$ of the hydrogel at each time was also determined by finding the location of maximal negative slope of each profile. For this purpose, experimental profiles were numerically differentiated.

From the fitting coefficients and measured size $R(t)$ of the hydrogel, we obtained the relative transport of the targets T determined by the movement of the wavefront midpoint position into the hydrogel, $r_0\%$ (t)

$$r_0\%(t) = \frac{R_0 - r_0}{R_0} \tag{7}$$

to describe how far into the hydrogel the midpoint of target T is located at a given time.

Mathematical Model for Reaction-Diffusion Process of Target T into the Hydrogel. The concentration c of a molecule undergoing pure diffusion follows the Fick's second law, which reads

$$\frac{\partial c}{\partial t} = D\Delta c \tag{8}$$

where D is the diffusion coefficient, t is time and Δ is a Laplacian ($\Delta c = \sum_i \frac{\partial^2}{\partial x_i^2}$ with x_i being Cartesian coordinates).

For diffusion within a radially symmetric sphere the concentration $c(\hat{r},t)$ as a function of time t and relative radial position $\hat{r} = r/R$ (where r is the radial position and R the radius of the sphere) is given as[38]

$$\frac{\partial c}{\partial t} = \frac{1\partial}{\hat{r}^2 \partial \hat{r}}\left(\hat{r}^2 \frac{D\partial c}{R^2 \partial \hat{r}}\right) \tag{9}$$

We assume that the equations valid for diffusion in a sphere are also valid for diffusion along the axis of a half sphere, as is our case. The hard boundary at the fiber end causes reflection of the diffusing molecules with similar result as diffusion from the other (missing) half of the sphere would have given. The hydrogels in question are also not perfectly hemispherical, which will introduce error into the model, depending on the magnitude of the deviation from a spherical geometry.

The reaction of strand T with the SB duplex integrated in the hydrogel can be modeled as a two-step process.[39] In the first step, T binds to the toehold region of S, creating a three-strand complex SBT. The junction point then migrates until eventually reaching the other end of the S−T binding region and dissociating into a strand B and ST duplex. The reaction rate constant for the hybridization of the toehold is denoted k^+, the reaction rate for its dissociation k^-. The rate constant for the branch migration process of a bound target is denoted k_b (see also Figure 1). When the cross-link is opened, we assume the reverse reaction is negligible, since the opening of the cross-link will lead to network relaxation and the hydrogel-bound strands S and B can be expected to be too far from each other for the rebinding to occur.[40] The evolution of the concentration of the target T can then be described by the following partial differential equations (PDEs):

$$\frac{\partial c}{\partial t} = \frac{1\partial}{\hat{r}^2 \partial \hat{r}}\left(\hat{r}^2 \frac{D\partial c}{R^2 \partial \hat{r}}\right) - k^+ c m_f + k^- m_c \tag{10}$$

$$\frac{\partial m_c}{\partial t} = k^+ c m_f - k^- m_c - k_b m_c \tag{11}$$

$$\frac{\partial m_o}{\partial t} = k_b m_c \tag{12}$$

$$m_t = m_f + m_c + m_o \tag{13}$$

where c is the molar concentration of the free target T, m_t is the total molar concentration of accessible binding cites, m_f is the molar concentration of free binding sites, m_c the molar concentration of three-strand complexes and m_o of the open cross-links. Equation 13 is the conservation of binding sites in the various possible states.

By introducing $\alpha = \frac{D}{R^2} > 0$, eq 10 can be rewritten as

$$\frac{\partial c}{\partial t} = \frac{\alpha \partial}{\hat{r}^2 \partial \hat{r}}\left(\hat{r}^2 \frac{\partial c}{\partial \hat{r}}\right) - k^+ c m_f + k^- m_c \tag{14}$$

By expressing m_f as a function of m_t, m_o and m_t we obtain a set of three equations (for c, m_c and m_o) with their corresponding boundary (B.C.) and initial conditions (I.C.):

$$\frac{\partial c}{\partial t} = \frac{\alpha \partial}{\hat{r}^2 \partial \hat{r}}\left(\hat{r}^2 \frac{\partial c}{\partial \hat{r}}\right) - k^+ c m_t + k^+ c m_c + k^+ c m_o + k^- m_c \tag{15}$$

https://dx.doi.org/10.1021/acs.biomac.9b01515
Biomacromolecules XXXX, XXX, XXX−XXX

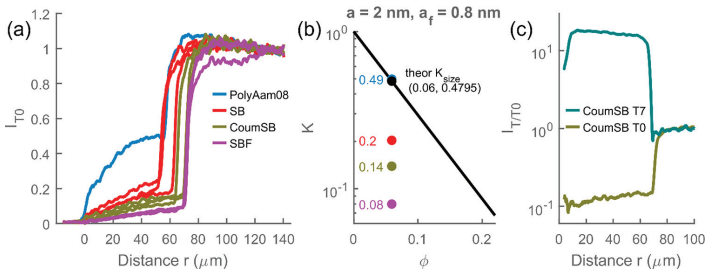

Figure 7. (a) Normalized fluorescence intensity of nonbinding T0 target labeled with Alexa Fluor 647 in different hydrogels: SB, CoumSB, SBF and PolyAam08. (b) Plot of partition coefficient K_{size} as a function of matrix volume fraction ϕ according to theory of Ogston (continuous line). The points depict the experimentally determined K of the T0 target DNA for the hydrogels shown in panel a. (c) Relative concentration profiles of the nonbinding target T0 and in binding target T7 in the same CoumSB hydrogel at equilibrium. Fiber end face at $r = 0$.

$$\text{B.C.:}\ \frac{\partial c(0,t)}{\partial \hat{r}} = 0,\ t \geq 0 \tag{16}$$

$$c(1,t) = c_{out} \tag{17}$$

$$\text{I.C.:}\ c(\hat{r},0) = \begin{cases} 0,\ 0 \leq \hat{r} < 1 \\ c_{out},\ \hat{r} = 1 \end{cases} \tag{18}$$

$$\frac{\partial m_c}{\partial t} = k^+ c m_t - k^+ c m_c - k^+ c m_o - k^- m_c - k_b m_c \tag{19}$$

$$\text{B.C.:}\ \frac{\partial m_c(0,t)}{\partial t} = 0 \tag{20}$$

$$m_c(1,t) = 0 \tag{21}$$

$$\text{I.C.:}\ m_c(\hat{r},0) = 0,\ 0 \leq \hat{r} \leq 1 \tag{22}$$

$$\frac{\partial m_o}{\partial t} = k_b m_c \tag{23}$$

$$\text{B.C.:}\ \frac{\partial m_o(0,t)}{\partial t} = 0 \tag{24}$$

$$m_o(1,t) = 0 \tag{25}$$

$$\text{I.C.:}\ m_o(\hat{r},0) = 0,\ 0 \leq \hat{r} \leq 1 \tag{26}$$

where c_{out} is the concentration at the boundary of the hydrogel.

Numerical Solution of the Reaction-Diffusion PDEs. To solve this system of equations numerically, we can apply the method of lines which reduces the PDE to a system of ordinary differential equations (ODEs) by discretizing one dimension (here the radial dimension) onto a finite grid with equal spacing and coordinates $\hat{r}_i = i\Delta\hat{r}$ for $i = 0,1,\cdots,N$. Similarly, c, m_o, m_c at grid point i will be denoted as c_i, m_{oi} and m_{ci}, respectively. The spatial derivatives are approximated using the second order centered finite difference approximation in spherical coordinates[41] and a system of ordinary differential equations (ODEs) is obtained at each point in the grid:

$$\frac{dc_i}{dt} = \begin{cases} \frac{6\alpha}{\Delta\hat{r}^2}(c_1 - c_0) - k^+ c_0 m_t + k^+ c_0 m_{c0} + k^+ c_0 m_{o0} \\ \quad + k^- m_{c0},\ \text{if } i = 0; \\ 0,\ \text{if } i = N; \\ \frac{\alpha}{i\Delta\hat{r}^2}[(i+1)c_{i+1} - 2ic_i + (i-1)c_{i-1}] - k^+ c_i m_t \\ \quad + k^+ c_i m_{ci} + k^+ c_i m_{oi} + k^- m_{ci},\ \text{otherwise} \end{cases} \tag{27}$$

$$\frac{dc_{bi}}{dt} = \begin{cases} 0,\ \text{if } i = N; \\ k^+ c_i m_t - k^+ c_i m_{ci} - k^+ c_i m_{oi} - k^- m_{ci} - k_b m_{ci},\ \text{otherwise} \end{cases} \tag{28}$$

$$\frac{dc_{oi}}{dt} = \begin{cases} 0,\ \text{if } i = N; \\ k_b m_{ci},\ \text{otherwise} \end{cases} \tag{29}$$

This set of equations can be solved using MATLAB built in ODE solver functions, here *ode15s*.

Fitting the Model to Experimental Data. The mathematical model of the reaction-diffusion process in a sphere was then fitted to the experimental data using MATLAB's *fminsearch* function. The boundary conditions for the free target concentration c were chosen with the partitioning effect taken into account for each of the different types of the hydrogels, i.e., the concentration of the free target at the boundary was $c(\hat{r} = 1,t) = c_{out} = K\ c_{sol}$, where K is the partition coefficient of nonbinding target T0 for the given type of gel and c_{sol} is the target concentration in the immersing solution. The experimentally determined values of K were employed in the modeling.

The model does not account for swelling, and the experimental data used for the fitting were composed of parts of the profile that fall within the hydrogel's initial size; that is, the length of the hydrogel used in the modeling was constant equal to its initial length R_s.

We also excluded several profiles at the beginning and end of the experiment, as the profiles were getting established and as they reached the fiber end face.

The parameters α, k^+, k^-, k_b, m_t, and t_{delay} were determined in the fitting procedure. The first scan was performed 20−40 s after adding the target stock solution in the physical experiments. The parameter t_{delay} was added to the model accounting for this time-shift, and the parameter estimation also included fitting of parameter values for t_{delay}.

RESULTS AND DISCUSSION

Partitioning. The normalized fluorescence intensity profile of nonbinding T0 target DNA labeled with Alexa Fluor 647 throughout various hydrogels after equilibration were determined for SB, CoumSB, SBF hydrogels as well as pure polyacrylamide hydrogels PolyAam08 (Figure 7a). These profiles clearly indicate exclusion of T0 DNA from the hydrogels, and the data from the individually prepared hydrogels clearly indicate that the extent of exclusion also depends on the nature of the hydrogel.

The partitioning coefficient was calculated as the ratio between the fluorescence intensity inside the hydrogel and the fluorescence intensity of the surrounding solution and averaged for hydrogels of the same type. The intensity inside

https://dx.doi.org/10.1021/acs.biomac.9b01515
Biomacromolecules XXXX, XXX, XXX−XXX

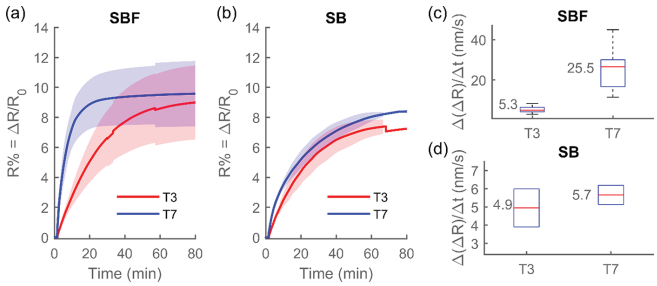

Figure 8. Relative swelling kinetics as determined by interferometry of SBF (a) and SB (b) hydrogels immersed in aqueous buffer solutions following an addition of either T7 or T3 to the immersing solution to a concentration of 20 μM. The lines show the average values, and the shaded areas show the standard deviation of several independent experiments (13 for SBF-T7, 7 for SBF-T3, and 2 for SB). The discontinuities in the curve are due to different time durations of some of the experiments. All individual curves are in Figure S9. (c,d) Initial rate of swelling at $t = 0$ as box plots.

the hydrogel was measured at a distance greater than 60 μm from the fiber, in order to avoid the effect of refraction from the fiber. The measured partition coefficients are depicted in Figure 7b. The partitioning of a binding target (T7) at equilibrium was also compared to the partitioning of a nonbinding target (T0) inside the same hydrogel (Figure 7c).

Several of the interactions that affect the partitioning (eq 3) can be expected to occur in the case of the target DNA strands in the DNA-hydrogels studied here. Size effects are a result of physical properties of the system, such as the size and shape of the solute and the size and shape of the hydrogel pores. Even when the solute is not physically obstructed from entering the gel network (due to size larger than the pore size), lower entropy due to fewer orientations available within the hydrogel contribute to exclusion of the solute.[36] Since PolyAam08 hydrogels do not contain DNA cross-links and the polyacrylamide network is itself electrically neutral, there are no electrostatic or biospecific interactions and the contribution to the total partition coefficient are expected to arise from size effects. Ogston[42] provided an equation to estimate the size contribution K_{size} to the partitioning coefficient K. It is based on placing spheres of radius a (solute) in a matrix of long cylindrical fibers of radius a_f, with a total volume fraction ϕ:

$$K = e^{-\phi\left(1+\frac{a}{a_f}\right)^2} \tag{30}$$

Approximating the parameter a by the radius of gyration of a single stranded DNA of 20 base pairs (a = 2 nm)[43] and using experimentally determined volume fraction ϕ = 0.06, and fiber radius a_f = 0.8 nm from Williams at al,[44] we would expect the size contribution to the partitioning coefficient to be K_{size} = 0.48 (Figure 7b).

There is excellent agreement between the theoretical value of K_{size} and the experimentally observed one for T0 DNA within the polyacrylamide hydrogels without any added DNA (PolyAam08) (Figure 7b). This also indicates that the ratio of the fluorescence intensity in the outermost layer of the hydrogel (over 60 μm from the fiber) compared with the surrounding solution reflects the actual ratio of the concentrations, unaffected by the presence of the fiber and/or distorted by other phenomena, such as increased light absorption inside the hydrogel.

There is a clear effect on the partition coefficient of T0 DNA due to the presence of hydrogel-bound DNA, for example, the difference observed for the SB hydrogel as compared to PolyAam08 (Figure 7a). Note that the PolyAam08 and the DNA-cross-linked hydrogels (SB, CoumSB, and SBF) were all prepared with the same 0.8 mol % cross-linker concentration relative to the Aam monomer, with only Bis or Bis and dsDNA-mediated cross-links, respectively. The fact that DNA is a polyanion, electrostatic interactions will be present between the hydrogel-bound DNA (S and B) and the solute (target T), favoring exclusion of T from the hydrogel in such a case (Figure 7a). The presence of the fluorescent dyes also influences the partition coefficient, as indicated from the data from CoumSB and SBF hydrogels (Figure 7a,b). This could be through effects on the stiffness of the chains, changes in hydrophobicity or charge. In particular, the hydrophobic character of fluorescein and coumarin and their difference in this, as indicated by their aqueous solubility (0.01 M for coumarin,[45] 1.5×10^{-4} M for fluorescein[46]), or the decrease in solution critical temperature of poly(*N*-isopropylacrylamide) hydrogels upon integration in these,[47] suggests that their hydrophobicity has a possible effect on the partitioning (e.g., differences in $K_{i,hphob}$ in eq 3).

For DNA-hydrogels immersed in solutions containing targets T that bind to the DNA incorporated in the hydrogel, this biospecific affinity leads to accumulation of the solute T inside of the hydrogel and a partition coefficient greater than 1. In Figure 7c, the effect of biospecific affinity on the partitioning can be seen, since the only difference between targets T7 and T0 is their complementarity, or lack thereof, with the hydrogel-bound DNA. The target T7 binds to the network and accumulates within the hydrogel, reaching concentrations greater than the concentration of the surrounding solution by 1 order of magnitude. The observation reported in Figure 7c indicates that the biospecific contribution to the partitioning (eq 3) is approximately 2 orders of magnitude greater as compared with the exclusion effects (T7 probe as compared to T0).

Effect of Toehold Length on the Overall Swelling. Figure 8 shows the relative swelling R% of SB and SBF hydrogels in solutions of targets T3 and T7. In the context of the theory for swelling of ionic hydrogels, the binding of the polyanionic target DNA to the network changes the ionic contribution to the osmotic pressure (T3, T7, T7b), and the concomitant elimination of a cross-link changes the elastic

https://dx.doi.org/10.1021/acs.biomac.9b01515
Biomacromolecules XXXX, XXX, XXX−XXX

contribution to the osmotic pressure (T3, T7), resulting in gel swelling. The actual relative swelling data (Figure 8) reveal a substantial variation in the rate and relative swelling at equilibrium among the independently prepared hydrogels. Despite this variation, which is elaborated below, a clear systematic difference in the initial swelling rate for the different toehold lengths are evident for SBF hydrogels (Figure 8c). The mean value of initial swelling rate is 5.3 nm/s for the swelling induced by 20 μM of T3 DNA, which is increased to 25.5 nm/s for the T7 DNA at the same concentration. For SB hydrogels there seems to be some indication of a larger initial swelling rate for T7 than T3, but not as large a difference as for the SBF type hydrogels. This could, however, be due to limited number of parallel experiments combined with the rather large observed variations between parallelly prepared hydrogels. Furthermore, the possible impact of a different purification method used by the oligonucleotide manufacturer for B strands and fluorescently labeled B strands on the swelling behavior is difficult to assess.

Nevertheless, the difference in the swelling rates between the two toehold lengths, from SBF data as well as from the limited available SB data, is far less than estimates based on the binding rates in solution would suggest. The rate of toehold-mediated strand displacement in solution has been shown to increase exponentially with the toehold length for toeholds up to 7 nucleotides (for toeholds longer than 7, the rate constant reaches a plateau).[39,48] For toehold lengths between 0 and 7 nucleotides, the rate of strand displacement is in order of 10^{toehold} M^{-1} s^{-1}. As a consequence, if the free target was available to the whole volume of the hydrogel immediately, target T7 binding should be leading to a swelling at a rate 10 000 times greater than T3 binding. From the plot of the swelling rate in Figure 8, we can see that this is not the case, and the changes in the swelling rate due to the differing toehold lengths are at best moderate.

Effect of Toehold Length on the Migration of the Target. The overall swelling of the DNA-*co*-acrylamide hydrogels is the result of a complex interplay in the cascade of processes involving diffusion of the target DNA, its initial binding and toehold-mediated strand displacement. The spatiotemporal relative concentration profiles of target DNA (T3, T7, T7b) represent the sum of concentrations of the free target (T) and the bound target (in SBT or ST) within the hydrogel, and the free target (T) in the surrounding solution. Examples of relative concentration profiles are shown in Figure 9. The profiles show the relative spatiotemporal concentrations of the three different binding targets T3, T7, and T7b in CoumSB hydrogels. The profiles for other parallel preparations of CoumSB hydrogels as well as SB and SBF hydrogels are qualitatively similar (Figures S4, S5, and S6), with the only difference being time to reach equilibrium (with SBF being the slowest on average and SB fastest).

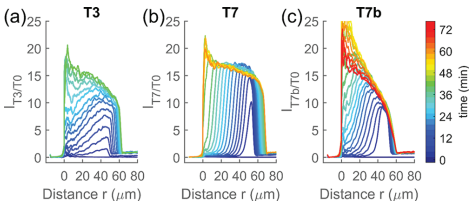

Figure 9. Example of spatiotemporal evolution of relative concentration of the target strand (a) T3, (b) T7, and (c) T7b inside CoumSB hydrogels. A profile is plotted for every 3rd minute. The fiber end faces are located at $r = 0$.

In the case of all three target strands, the target's concentration within the hydrogel is rapidly increasing to levels higher than those in the surrounding solution due to the binding of the target to the DNA conjugated to the network. The maximum equilibrium fluorescence intensity indicates a DNA probe concentration inside the hydrogel from 10 to 25 times the concentration of the surrounding solution. The displacement of the outer edge of the profiles toward increasing r reflects the hydrogel swelling.

Notably, the following differences in spatiotemporal concentration profiles of the target DNA reflect the molecular properties of the target DNAs. T3 DNA, with a toehold length of 3 nucleotides, is found to imbibe the DNA-*co*-AAm hydrogel by gradually increasing its fluorescence intensity throughout the hydrogel. For the particular hydrogel in Figure 9a, already after the first 3 min, the T3 DNA concentration in the vicinity of the fiber is reaching the levels of the outside solution. The T3 strand concentration at the hydrogel–solution interface is increasing gradually, reaching its maximum after 18 min. In contrast, the T7 DNA (example shown in Figure 9b) is first reaching its maximum concentration on the edge of the hydrogel, already within the first 6 min, before any of the target molecules reach the fiber end face. It exhibits a steep wavefront which then moves with unchanged slope of the invading front toward the optical fiber. The target T7b, which has the same toehold as T7, but is not complementary to S on the blocking region, only binds and does not lead to cross-link opening. The concentration profiles of T7b are similar to those of T7, but we observe an increase in fluorescence close to the fiber and a decrease on the outer edge of the hydrogel.

The abrupt peaks in fluorescence observed near the fiber end face (0–10 μm), as best seen in Figure 9b, are due to noise introduced by the procedure used to correct for the presence of the fiber. The method is sensitive to misalignments in the radial position of the sample (I_T) and the reference (I_{T0}).[37] However, an increase in fluorescence intensity beyond this effect has been observed for T7b consistently for all types of hydrogels (Figure 9c and S3–S5). This behavior suggests the presence of a mechanism other than binding and cross-link opening, but at present of unclear origin, which is affecting the partition and/or diffusion of target T7b.

Figure 10 depicts the relative position of the wavefront midpoint in the hydrogel and the slope of the profiles at wavefront midpoint as a function of time for repeated experiments exposing hydrogels SB, CoumSB, and SBF to target strands T3 or T7. The substantial variability in the wavefront movement observed for independently prepared hydrogels can mask differences arising from differing toehold lengths. The wavefront midpoint is seen to invade into SB hydrogels on average faster than in the other hydrogels, with SBF hydrogels being on average the slowest. However, there is a large overlap between and a large variability within the three hydrogel groups, complicating any conclusions.

The difference in the apparent target diffusion depending on the molecular properties of the toehold is more evident in the slope at the wavefront midpoint (Figure 10). The slopes of wavefronts for apparent T7 diffusion are larger than those for T3 by several orders of magnitude. We can also observe that

https://dx.doi.org/10.1021/acs.biomac.9b01515
Biomacromolecules XXXX, XXX, XXX–XXX

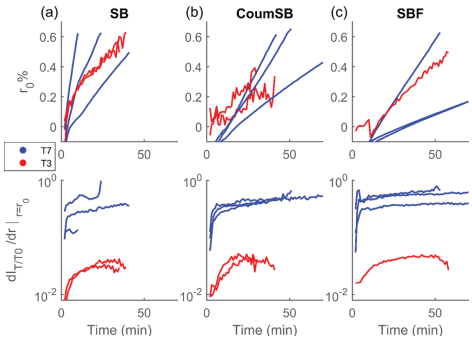

Figure 10. Empirical parameters reflecting the spatiotemporal evolution of the target DNA (T3 and T7) in (a) SB, (b) CoumSB, and (c) SBF hydrogels, as deduced from the time-lapse confocal micrographs. These data are the relative position of the wavefront midpoint in the hydrogel r_0% and the slope at the wavefront midpoint. Both shown as a function of time after the targets T3 or T7 were introduced into the solution surrounding the hydrogels at $t = 0$.

the slopes of T7 concentration wavefront are nearly constant with time, showing no diffusional broadening. For T3, the wavefront slopes are getting steeper with time as the concentration in the outermost part is increasing faster than at the fiber end face, thus increasing the height of the wavefront and its slope with it. For T3, the slope begins to decrease when the wavefront is reaching the fiber.

Similar to the relative swelling (as determined by interferometry, Figure 8) the time evolution of the wavefront midpoint position r_0% varies between hydrogels, and the interhydrogel variability in this case seems to mask the difference arising from the different toehold lengths (Figure 10). Possible differences in the heterogeneity among the independently prepared hydrogels, as elaborated below in the context of the parameters obtained using the reaction diffusion modeling, could contribute to the variability.

The longer toehold T7, despite its 10 000 times larger rate of toehold-mediated strand displacement compared to that of T3, offers only a moderate increase in the overall swelling rate of the hydrogel. Qualitative evaluation of the concentration profiles in Figure 9 as well as the values of the slope at wavefront midpoint (Figure 10) offer an explanation. The rate of initial binding of T7 is so high that each hydrogel layer must be filled up to an equilibrium before the target strands can diffuse further without being drained from the diffusable pool by binding to the dsDNA, thus resulting in a sharp front. This is in contrast to a less-stable binding of the T3 DNA due to the initial binding to the short toehold being less stable. Targets T3 are detaching from the binding sites on S at a much higher rate and are allowed to diffuse further into the gel between each binding event and the wavefronts are shallower. A similar observation was made for adsorption of various transported proteins in agarose gels by Emily Schirmer and Giorgio Carta.[49] This difference in the effective diffusion has an effect on the overall swelling of the hydrogel. Longer toehold and higher rate of toehold-mediated strand displacement means that although the target is binding stronger and reaching a high concentration within the hydrogel very quickly, the binding is occurring in a limited volume compared with the binding of a target with a shorter toehold and consequently the swelling is locally limited to this volume.

Diffusion Coefficient and Binding Rates Estimated from Reaction-Diffusion Modeling. Figure 11 shows the

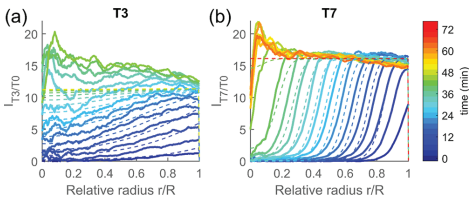

Figure 11. Spatiotemporal evolution of the relative concentration of targets (a) T3 and (b) T7 inside the same CoumSB hydrogels as shown in Figure 9. A profile is plotted for every 3rd minute. In dotted lines, the profiles obtained by fitting the numerical reaction-diffusion model to the experimental data are shown.

same experimental profiles for T3 and T7 in CoumSB hydrogels as were shown in Figure 9, here overlaid with the profiles obtained from the fitting of the reaction-diffusion model (shown for every third minute, but fitting was conducted on the basis of data acquired every minute).

Figure 12 depicts the parameters obtained by fitting the reaction-diffusion model to the time evolution of the T3 and

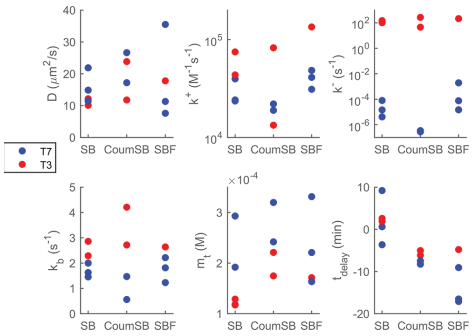

Figure 12. Parameters acquired by fitting experimentally determined reaction-diffusion profiles of the T3 (red symbols) and T7 (blue symbols) target DNA to the reaction-diffusion numerical model for SB, CoumSB, and SBF hydrogels when immersed in 20 μM of the target DNA.

T7 target concentration profiles. The parameters estimated this way are the diffusion coefficient D, the rate constants, the concentration of available binding sites and a delay parameter that reflects the initiation time for exposing the hydrogels to the aqueous solution with the target DNA. The fitted profiles for the rest of the hydrogels are shown in Figures S7, S8, and S9.

The model fits the T7 profiles better than T3 profiles, but the fits to the reaction-diffusion pattern for both toehold lengths reproduce essential experimentally determined trends. In case of hydrogels exposed to T3, the optimization yielded local minima depending on the starting conditions, where different combinations of rate constants yielded equally

https://dx.doi.org/10.1021/acs.biomac.9b01515
Biomacromolecules XXXX, XXX, XXX−XXX

adequate fitting curves, while the other parameters were largely unaffected. For reaction rate constants reported here, the estimates derived from the strand displacement model of Zhang and Winfree[39] were used as starting parameters.

An important assumption made when performing the model fitting was that the ratio of the fluorescence intensities between the hydrogel and the surrounding solution reflects the actual concentration ratio (after adjusting for the effect of the fiber presence). This assumption was made in the light of the findings about the different partitioning for the different types of hydrogels and the fact that the observed partitioning for pure polyacrylamide hydrogel was in agreement with the literature. The difference in the different types of hydrogels was then reflected in the choice of boundary conditions, dictated by the partitioning.

The diffusion coefficient of the target DNA was measured to be 17 ± 8 $\mu m^2/s$. The diffusion coefficient of ssDNA with a number of nucleotides $N \geq 10$ in aqueous solution at 20 °C can be estimated by[50]

$$D_{ssDNA} = 7.38 \times 10^{-6} N^{-0.539} cm^2/s \quad (31)$$

which for a strand of 18 bases leads to $D_{ssDNA,18} = 155\ \mu m^2/s$. The diffusion coefficient is reduced inside the hydrogel. The estimated reduction according to Park et al.[51] can be calculated as

$$\frac{D_{gel}}{D_{sol}} = \exp(-3.03 R_h^{0.59} C^{0.94}) \quad (32)$$

where R_h is the hydrodynamic radius of the solute in angstrom (approximately 20 Å for ssDNA of length 18 bases) and C (g/mL) is the acrylamide concentration (in our case approximately 0.07 g/mL in a swollen hydrogel). This estimates the diffusion coefficient of the target DNA strands in the hydrogel to be 23% of its value in solution (i.e., 36 $\mu m^2/s$).

For polyethylene glycol of varying molecular weight, the diffusion coefficient in neutral polyacrylamide hydrogel of the same volume fraction as the hydrogels presented here (0.06) is reduced to 15% of its value in solution.[52] For our ssDNA (which similarly to polyethylene glycol behaves as a random coil), this would reduce the diffusion coefficient to 23 $\mu m^2/s$. A similar value of approximately 30 $\mu m^2/s$ was reported for ssDNA of corresponding molecular weight in polyacrylamide hydrogels[53] (of somewhat different composition than ours,[54] 6%T, 5%C, compared with our approximately 10%T, 2%C, where %T is the total concentration of monomers and %C is the weight percentage of cross-linker).

The concentration of the SB duplex in the pregel solution is 2.82 mmol/L. After polymerization the gels are equilibrated in buffer and they reach a new swelling equilibrium before the target solution is added. This swelling of the hydrogel reduces the concentration of the SB duplex to approximately 2 mmol/L and subsequent swelling induced by the interaction with target ssDNA will reduce this concentration further. However, the apparent concentration of the binding sites that provides the best model fits is 0.2 ± 0.07 mmol/L (i.e., one tenth of the SB concentration as calculated from the initial concentrations). A possible explanation would be that only a tenth of the SB duplexes within the hydrogel are available for binding of the target strands, the other ones being inaccessible due to constraints created by the hydrogel network. The constraints induced by the Aam network and variation in this could originate from the heterogeneity of such network synthesized in a copolymerization cross-linking reaction.[55−57] As the local environment surrounding the dsDNA are expected to vary both within a particular hydrogel, variation in average accessible dsDNA for binding target DNA can also be expected to occur among parallel preparations. A variation in this available fraction would also explain the differences between the partitioning values for the different hydrogels at equilibrium as well as differences in the relative swelling at equilibrium as measured by the interferometer (Figure 8). Thus, a sensor application using this design would have to implement a calibration for each individual hydrogel to account for the variation arising from network heterogeneity.

The experimentally obtained values of the rate constants k^+, k^-, and k_b are shown in Table 1, along with the theoretical values calculated according to Zhang and Winfree.[39] Except for k^+, all the rate constants are within two standard deviations of the theoretical value, and k^- is within one standard deviation. The observed reduction in k^+ (which reflects the toehold hybridization rate) compared with its expected value in solution is in accordance with the previously reported decrease in the melting temperature for DNA incorporated within a polyacrylamide hydrogel.[58] Similar effects have been seen for hybridization of DNA bound to a hard surface.[59−63] Shielding of the binding sites, whether by physical, electrostatic, or other effects, is usually stated as the underlying mechanism for the reduction in the hybridization rate.

Table 1. Estimated Average Values of Reaction Rate Constants and Their Standard Deviations Acquired by Fitting Experimental Data to the Reaction-Diffusion Model for T3 and T7 Target DNA[a]

	experimental value[b]	estimated value[39]
k^+ (M^{-1} s^{-1})	T3: $10^{(4.7\pm0.4)}$	T3: $6 \times 10^6 = 10^{6.8}$
	T7: $10^{(4.5\pm0.1)}$	T7: $6 \times 10^6 = 10^{6.8}$
k^- (s^{-1})	T3:$10^{(2.1\pm0.3)}$	T3: $224.7 = 10^{2.3}$
	T7: $10^{(-5\pm1)}$	T7: $6.6 \times 10^{-6} = 10^{-5.2}$
k_b (s^{-1})	2 ± 1	4

[a]Estimated Values Using Prediction Models by Zhang and Winfree[39].
[b]The averaged values were obtained based on the estimates of the parameter values determined in the fit of the reaction−diffusion model to experiments in several independently prepared SB, CoumSB and SBF hydrogels (Figure 12) for the T3 and T7 target DNA.

The values of the t_{delay} parameter vary between −20 and +10 min. We expected this parameter to be mostly within 1 min as it was supposed to account for the delay between exposing the hydrogel to the target solution and the first scan within 20−40 s. It is possible that the larger values of t_{delay} reflect the fact that swelling was not taken into account by the model, and as a result, the numerically calculated profiles offer a worse fit to experiment especially for the initial profiles. Since SBF hydrogels showed on average the slowest target transport, the time before the profiles were fully established further from the edge was the longest, which is possibly reflected in the largest t_{delay} values for SBF hydrogels.

The parameters obtained by model fitting vary little both within and between the three different types of hydrogels (Figure 12), despite the large variability observed for parallelly prepared hydrogels and the response kinetics being on average different for the different hydrogel types (as seen from the evolution of the wavefront midpoint position r_0%, Figure 10

https://dx.doi.org/10.1021/acs.biomac.9b01515
Biomacromolecules XXXX, XXX, XXX−XXX

and from spatiotemporal target concentration profiles (Figures S4−S6)).

This suggests that the model accounts for both the hydrogel variability as well as the effect of the fluorescent dyes that define the different hydrogel types. As discussed above, the inherent inhomogeneity of polyacrylamide hydrogels could be reflected in the concentration of the binding sites—a parameter estimated by model fitting.

The addition of the fluorescent dyes was seen to limit the partitioning of the target compared with unlabeled hydrogels, to a degree dependent on the type of the dye. Simulations by Schuck[64] show that lower partition coefficient can have similar effects on the overall transport in a hydrogel as a lower diffusion coefficient. By measuring the partition coefficient for a nonbinding target, we were able to take this into account when modeling and use this value to derive the effective experimental boundary conditions. This allowed us to separate the effect of partitioning from that of diffusion, and the remaining parameters are consistent between the different hydrogel types. This finding suggests that fluorescent dyes affect hydrogel kinetics mainly through their effect on the target partitioning.

The good agreement of fitted parameters with the literature suggests that the theoretical values of rate constants based on toehold and binding region lengths can be used to predict the behavior of DNA-hybrid hydrogels. This is despite the fact that these theoretical values are developed for reactions in solution, and there is evidence suggesting that tethering DNA to a surface[59,61−63,65] or inside a hydrogel[58] can have an effect on its hybridization kinetics. However, for an accurate simulation of the target reaction-diffusion process, the total available binding site concentration and the partitioning of the target need to be estimated along with the rate constants.

CONCLUSIONS

In the present study, we have found that spatiotemporal evolution of migrating target DNA with different molecular properties in dsDNA-*co*-acrylamide hydrogels yield insight into the interdependence of the cascading processes that precede the swelling (i.e., transport, binding, cross-link opening, and localized swelling). In particular, the data indicate that the more strongly interacting target DNA possessing a longer toehold with the conjugated dsDNA is drained from the migrating target DNA pool, yielding a reaction-diffusion pattern with a steep moving wavefront within the hydrogel. In contrast, the hydrogel is filling more gradually throughout its entire volume for the target DNA that possesses a shorter toehold. A change of toehold length thus leads not only to a change in the binding properties of the target, but it has an effect on its transport throughout the gel as well. The resulting swelling is a result of an interaction between these processes. Both the partitioning and the parameter values from the reaction-diffusion modeling of the process indicate that most of the embedded dsDNA in the hydrogels are sterically hindered from interacting with the target DNA. This facet is suggested to arise from the heterogeneous nature of the hydrogels prepared by the copolymerization−cross-linking strategy. Furthermore, the diffusion coefficient and the reaction rate constants of the strand displacement were found to be in good agreement with other reported or theoretical values, suggesting the possibility to use this simple model and theoretical rate constant values to qualitatively predict the spatiotemporal concentration profiles of the target inside the hydrogel. Overall, the fluorescence-based characterization of the spatiotemporal evolution of the migrating target DNA offer novel insight in the underlying processes eventually leading to target DNA induced swelling of dsDNA-*co*-acrylamide hydrogels.

ASSOCIATED CONTENT

Supporting Information

The Supporting Information is available free of charge at https://pubs.acs.org/doi/10.1021/acs.biomac.9b01515.

Correcting the intensity profiles for the optical effect caused by the presence of the fiber by using Coumarin labeled acrylamide as internal reference (Figure S1); use of FRET for monitoring of cross-link opening (text); decrease in Fluorescein's fluorescence intensity in SBF hydrogels, after exposure of the hydrogel to the target solution (Figure S2); relative swelling kinetics as determined by interferometry of SBF and SB (Figure S3); spatio-temoral evolution of relative concentrations of the target T3, T7, and T7b inside SB hydrogels (Figure S4); CoumSB hydrogels (Figure S5) and SBF hydrogels (Figure S6); profiles obtained by fitting the numerical reaction-diffusion model to the experimental profiles of relative concentration of T3 or T7 in SB hydrogels (Figure S7); CoumSB hydrogels (Figure S8) and SBF hydrogels (Figure S9) (PDF)

AUTHOR INFORMATION

Corresponding Author

Bjørn Torger Stokke − *NTNU—Norwegian University of Science and Technology, Trondheim, Norway;* orcid.org/0000-0003-2991-8088; Email: bjorn.stokke@ntnu.no

Other Authors

Eleonóra Parelius Jonášová − *NTNU—Norwegian University of Science and Technology, Trondheim, Norway*

Astrid Bjørkøy − *NTNU—Norwegian University of Science and Technology, Trondheim, Norway*

Complete contact information is available at: https://pubs.acs.org/10.1021/acs.biomac.9b01515

Author Contributions

The manuscript was written through contributions of all authors. All authors have given approval to the final version of the manuscript.

Notes

The authors declare no competing financial interest.

ACKNOWLEDGMENTS

This research was supported by the Research Council of Norway (Project no 240299/F20).

REFERENCES

(1) Li, J.; Mo, L.; Lu, C.-H.; Fu, T.; Yang, H.-H.; Tan, W. Functional Nucleic Acid-Based Hydrogels for Bioanalytical and Biomedical Applications. *Chem. Soc. Rev.* **2016**, *45* (5), 1410−1431.

(2) Liu, J. Oligonucleotide-Functionalized Hydrogels as Stimuli Responsive Materials and Biosensors. *Soft Matter* **2011**, *7* (15), 6757−6767.

(3) Xiong, X.; Wu, C.; Zhou, C.; Zhu, G.; Chen, Z.; Tan, W. Responsive DNA-Based Hydrogels and Their Applications. *Macromol. Rapid Commun.* **2013**, *34* (16), 1271−1283.
(4) Jonášová, E. P.; Stokke, B. T. Bioresponsive DNA-Co-Polymer Hydrogels for Fabrication of Sensors. *Curr. Opin. Colloid Interface Sci.* **2016**, *26*, 1−8.
(5) Meng, H. M.; Liu, H.; Kuai, H.; Peng, R.; Mo, L.; Zhang, X. B. Aptamer-Integrated DNA Nanostructures for Biosensing, Bioimaging and Cancer Therapy. *Chem. Soc. Rev.* **2016**, *45* (9), 2583−2602.
(6) Aldaye, F. A.; Palmer, A. L.; Sleiman, H. F. Assembling Materials with DNA as the Guide. *Science (Washington, DC, U. S.)* **2008**, *321* (5897), 1795−1799.
(7) Seeman, N. C. DNA in a Material World. *Nature* **2003**, *421*, 427−431.
(8) Roh, Y. H.; Ruiz, R. C. H.; Peng, S.; Lee, J. B.; Luo, D. Engineering DNA-Based Functional Materials. *Chem. Soc. Rev.* **2011**, *40* (12), 5730−5744.
(9) Chao, J.; Zhu, D.; Zhang, Y.; Wang, L.; Fan, C. DNA Nanotechnology-Enabled Biosensors. *Biosens. Bioelectron.* **2016**, *76*, 68−79.
(10) Zhang, F.; Nangreave, J.; Liu, Y.; Yan, H. Structural DNA Nanotechnology: State of the Art and Future Perspective. *J. Am. Chem. Soc.* **2014**, *136* (32), 11198−11211.
(11) Pinheiro, A. V.; Han, D.; Shih, W. M.; Yan, H. Challenges and Opportunities for Structural DNA Nanotechnology. *Nature Nanotechnology* **2011**, *6*, 763−772.
(12) Mao, Y.; Li, J.; Yan, J.; Ma, Y.; Song, Y.; Tian, T.; Liu, X.; Zhu, Z.; Zhou, L.; Yang, C. A Portable Visual Detection Method Based on a Target-Responsive DNA Hydrogel and Color Change of Gold Nanorods. *Chem. Commun.* **2017**, *53* (47), 6375−6378.
(13) Kim, T.; Park, S.; Lee, M.; Baek, S.; Lee, J. B.; Park, N. DNA Hydrogel Microspheres and Their Potential Applications for Protein Delivery and Live Cell Monitoring. *Biomicrofluidics* **2016**, *10* (3), 034112.
(14) Ma, Y.; Mao, Y.; An, Y.; Tian, T.; Zhang, H.; Yan, J.; Zhu, Z.; Yang, C. J. Target-Responsive DNA Hydrogel for Non-Enzymatic and Visual Detection of Glucose. *Analyst* **2018**, *143*, 1679−1684.
(15) Liu, S.; Su, W.; Li, Y.; Zhang, L.; Ding, X. Manufacturing of an Electrochemical Biosensing Platform Based on Hybrid DNA Hydrogel: Taking Lung Cancer-Specific MiR-21 as an Example. *Biosens. Bioelectron.* **2018**, *103*, 1−5.
(16) Yang, H.; Liu, H.; Kang, H.; Tan, W. Engineering Target-Responsive Hydrogels Based on Aptamer–Target Interactions. *J. Am. Chem. Soc.* **2008**, *130* (20), 6320−6321.
(17) Srinivas, R. L.; Chapin, S. C.; Doyle, P. S. Aptamer-Functionalized Microgel Particles for Protein Detection. *Anal. Chem.* **2011**, *83* (23), 9138−9145.
(18) Bai, W.; Spivak, D. A. A Double-Imprinted Diffraction-Grating Sensor Based on a Virus-Responsive Super-Aptamer Hydrogel Derived from an Impure Extract. *Angew. Chem., Int. Ed.* **2014**, *53* (8), 2095−2098.
(19) Wei, X.; Tian, T.; Jia, S.; Zhu, Z.; Ma, Y.; Sun, J.; Lin, Z.; Yang, C. J. Microfluidic Distance Readout Sweet Hydrogel Integrated Paper-Based Analytical Device (MDiSH-PAD) for Visual Quantitative Point-of-Care Testing. *Anal. Chem.* **2016**, *88* (4), 2345−2352.
(20) Joseph, K. A.; Dave, N.; Liu, J. Electrostatically Directed Visual Fluorescence Response of DNA-Functionalized Monolithic Hydrogels for Highly Sensitive Hg2+ Detection. *ACS Appl. Mater. Interfaces* **2011**, *3* (3), 733−739.
(21) Ye, B.-F.; Zhao, Y.-J.; Cheng, Y.; Li, T.-T.; Xie, Z.-Y.; Zhao, X.-W.; Gu, Z.-Z. Colorimetric Photonic Hydrogel Aptasensor for the Screening of Heavy Metal Ions. *Nanoscale* **2012**, *4* (19), 5998−6003.
(22) Song, P.; Ye, D.; Zuo, X.; Li, J.; Wang, J.; Liu, H.; Hwang, M. T.; Chao, J.; Su, S.; Wang, L. L.; et al. DNA Hydrogel with Aptamer-Toehold-Based Recognition, Cloaking, and Decloaking of Circulating Tumor Cells for Live Cell Analysis. *Nano Lett.* **2017**, *17* (9), 5193−5198.
(23) Chen, W. H.; Liao, W. C.; Sohn, Y. S.; Fadeev, M.; Cecconello, A.; Nechushtai, R.; Willner, I. Stimuli-Responsive Nucleic Acid-Based Polyacrylamide Hydrogel-Coated Metal−Organic Framework Nanoparticles for Controlled Drug Release. *Adv. Funct. Mater.* **2018**, *28*, 1705137.
(24) Lai, J.; Li, S.; Shi, X.; Coyne, J.; Zhao, N.; Dong, F.; Mao, Y.; Wang, Y. Displacement and Hybridization Reactions in Aptamer-Functionalized Hydrogels for Biomimetic Protein Release and Signal Transduction. *Chem. Sci.* **2017**, *8* (11), 7306−7311.
(25) Wang, Z.; Xia, J.; Cai, F.; Zhang, F.; Yang, M.; Bi, S.; Gui, R.; Li, Y.; Xia, Y. Aptamer-Functionalized Hydrogel as Effective Anti-Cancer Drugs Delivery Agents. *Colloids Surf., B* **2015**, *134*, 40−46.
(26) Jiang, F. X.; Yurke, B.; Firestein, B. L.; Langrana, N. A. Neurite Outgrowth on a DNA Crosslinked Hydrogel with Tunable Stiffnesses. *Ann. Biomed. Eng.* **2008**, *36* (9), 1565−1579.
(27) Shao, Y.; Jia, H.; Cao, T.; Liu, D. Supramolecular Hydrogels Based on DNA Self-Assembly. *Acc. Chem. Res.* **2017**, *50* (4), 659−668.
(28) Zhang, Z.; Du, J.; Li, Y.; Wu, J.; Yu, F.; Chen, Y. An Aptamer-Patterned Hydrogel for the Controlled Capture and Release of Proteins: Via Biorthogonal Click Chemistry and DNA Hybridization. *J. Mater. Chem. B* **2017**, *5* (30), 5974−5982.
(29) Cangialosi, A.; Yoon, C. K.; Liu, J.; Huang, Q.; Guo, J.; Nguyen, T. D.; Gracias, D. H.; Schulman, R. DNA Sequence−Directed Shape Change of Photopatterned Hydrogels via High-Degree Swelling. *Science (Washington, DC, U. S.)* **2017**, *357* (6356), 1126−1130.
(30) Fern, J.; Scalise, D.; Cangialosi, A.; Howie, D.; Potters, L.; Schulman, R. DNA Strand-Displacement Timer Circuits. *ACS Synth. Biol.* **2017**, *6* (2), 190−193.
(31) Tierney, S.; Hjelme, D. R.; Stokke, B. T. B. T. Determination of Swelling of Responsive Gels with Nanometer Resolution. Fiber-Optic Based Platform for Hydrogels as Signal Transducers. *Anal. Chem.* **2008**, *80* (13), 5086−5093.
(32) Nagahara, S.; Matsuda, T. Hydrogel Formation via Hybridization of Oligonucleotides Derivatized in Water-Soluble Vinyl Polymers. *Polym. Gels Networks* **1996**, *4* (2), 111−127.
(33) Tierney, S.; Stokke, B. T. Development of an Oligonucleotide Functionalized Hydrogel Integrated on a High Resolution Interferometric Readout Platform as a Label-Free Macromolecule Sensing Device. *Biomacromolecules* **2009**, *10* (6), 1619−1626.
(34) Gao, M.; Gawel, K.; Stokke, B. T. Toehold of DsDNA Exchange Affects the Hydrogel Swelling Kinetics of a Polymer-DsDNA Hybrid Hydrogel. *Soft Matter* **2011**, *7* (5), 1741−1746.
(35) Kibbe, W. A. (Northwestern U. OligoCalc: An Online Oligonucleotide Properties Calculator. *Nucleic Acids Res.* **2007**, *35*, W43.
(36) Gehrke, S. H.; Fisher, J. P.; Palasis, M.; Lund, M. E. Factors Determining Hydrogel Permeability. *Ann. N. Y. Acad. Sci.* **1997**, *831* (1), 179−184.
(37) Jonášová, E. P.; Bjørkøy, A.; Stokke, B. T. Recovering Fluorophore Concentration Profiles from Confocal Images near Lateral Refractive Index Step Changes. *J. Biomed. Opt.* **2016**, *21* (12), 126014.
(38) Ford Versypt, A. N.; Arendt, P. D.; Pack, D. W.; Braatz, R. D. Derivation of an Analytical Solution to a Reaction-Diffusion Model for Autocatalytic Degradation and Erosion in Polymer Microspheres. *PLoS One* **2015**, *10* (8), e0135506.
(39) Zhang, D. Y.; Winfree, E. Control of DNA Strand Displacement Kinetics Using Toehold Exchange. *J. Am. Chem. Soc.* **2009**, *131* (47), 17303−17314.
(40) Yurke, B.; Mills, A. P. Using DNA to Power Nanostructures. *Genet. Program. Evolvable Mach.* **2003**, *4* (2), 111−122.
(41) Crank, J. *The Mathematics of Diffusion*; Oxford University Press: Oxford, 1975; pp 148−149.
(42) Ogston, A. G. The Spaces in a Uniform Random Suspension of Fibres. *Trans. Faraday Soc.* **1958**, *54* (0), 1754−1757.
(43) Sim, A. Y. L.; Lipfert, J.; Herschlag, D.; Doniach, S. Salt Dependence of the Radius of Gyration and Flexibility of Single-Stranded DNA in Solution Probed by Small-Angle x-Ray Scattering. *Phys. Rev. E* **2012**, *86*, 021901.

https://dx.doi.org/10.1021/acs.biomac.9b01515
Biomacromolecules XXXX, XXX, XXX−XXX

(44) Williams, J. C., Jr; Mark, L. A.; Eichholtz, S. Partition and Permeation of Dextran in Polyacrylamide Gel. *Biophys. J.* **1998**, *75* (1), 493−502.
(45) Dannenfelser, R. M.; Yalkowsky, S. H. Data Base of Aqueous Solubility for Organic Non-Electrolytes. *Sci. Total Environ.* **1991**, *109−110* (C), 625−628.
(46) Dehn, W. M. Comparative Solubilities in Water, in Pyridine and in Aqueous Pyridine. *J. Am. Chem. Soc.* **1917**, *39* (7), 1399−1404.
(47) Yamada, A.; Hiruta, Y.; Wang, J.; Ayano, E.; Kanazawa, H. Design of Environmentally Responsive Fluorescent Polymer Probes for Cellular Imaging. *Biomacromolecules* **2015**, *16* (8), 2356−2362.
(48) Li, Q.; Luan, G.; Guo, Q.; Liang, J. A New Class of Homogeneous Nucleic Acid Probes Based on Specific Displacement Hybridization. *Nucleic Acids Res.* **2002**, *30* (2), e5.
(49) Schirmer, E. B.; Carta, G. Protein Adsorption in Charged Agarose Gels Studied by Light Microscopy. *AIChE J.* **2007**, *53* (6), 1472−1482.
(50) Stellwagen, E.; Lu, Y.; Stellwagen, N. C. Unified Description of Electrophoresis and Diffusion for DNA and Other Polyions. *Biochemistry* **2003**, *42* (40), 11745−11750.
(51) Park, I. H.; Johnson, C. S.; Gabriel, D. A. Probe Diffusion in Polyacrylamide Gels. *Macromolecules* **1990**, *23*, 1548−1553.
(52) Tong, J.; Anderson, J. L. Partitioning and Diffusion of Proteins and Linear Polymers in Polyacrylamide Gels. *Biophys. J.* **1996**, *70* (3), 1505−1513.
(53) Yin, H.; Kleemiß, M. H.; Lux, J. A.; Schomburg, G. Diffusion Coefficients of Oligonucleotides in Capillary Gel Electrophoresis. *J. Microcolumn Sep.* **1991**, *3* (4), 331−335.
(54) Yin, H.; Lux, J. A.; Schomburg, G. Production of Polyacrylamide Gel Filled Capillaries for Capillary Gel Electrophoresis (CGE): Influence of Capillary Surface Pretreatment on Performance and Stability. *J. High Resolut. Chromatogr.* **1990**, *13* (9), 624−627.
(55) Shibayama, M. Universality and Specificity of Polymer Gels Viewed by Scattering Methods. *Bull. Chem. Soc. Jpn.* **2006**, *79* (12), 1799−1819.
(56) Habicht, A.; Schmolke, W.; Lange, F.; Saalwächter, K.; Seiffert, S. The Non-Effect of Polymer-Network Inhomogeneities in Microgel Volume Phase Transitions: Support for the Mean-Field Perspective. *Macromol. Chem. Phys.* **2014**, *215* (11), 1116−1133.
(57) Di Lorenzo, F.; Seiffert, S. Nanostructural Heterogeneity in Polymer Networks and Gels. *Polym. Chem.* **2015**, *6* (31), 5515−5528.
(58) Fotin, A. V.; Drobyshev, A. L.; Proudnikov, D. Y.; Perov, A. N.; Mirzabekov, A. D. Parallel Thermodynamic Analysis of Duplexes on Oligodeoxyribonucleotide Microchips. *Nucleic Acids Res.* **1998**, *26* (6), 1515−1521.
(59) Hoefert, M. J.; Sambriski, E. J.; Jose de Pablo, J. Molecular Pathways in DNA-DNA Hybridization of Surface-Bound Oligonucleotides. *Soft Matter* **2011**, *7*, 560−566.
(60) Wong, I. Y.; Melosh, N. A. An Electrostatic Model for DNA Surface Hybridization. *Biophys. J.* **2010**, *98* (12), 2954−2963.
(61) Hagan, M. F.; Chakraborty, A. K. Hybridization Dynamics of Surface Immobilized DNA. *J. Chem. Phys.* **2004**, *120* (10), 4958−4968.
(62) Peterson, A. W.; Heaton, R. J.; Georgiadis, R. M. The Effect of Surface Probe Density on DNA Hybridization. *Nucleic Acids Res.* **2001**, *29* (24), 5163−5168.
(63) Vainrub, A.; Pettitt, B. M. Accurate Prediction of Binding Thermodynamics for DNA on Surfaces. *J. Phys. Chem. B* **2011**, *115* (45), 13300−13303.
(64) Schuck, P. Kinetics of Ligand Binding to Receptor Immobilized in a Polymer Matrix, as Detected with an Evanescent Wave Biosensor. I. A Computer Simulation of the Influence of Mass Transport. *Biophys. J.* **1996**, *70* (3), 1230−1249.
(65) Erickson, D.; Li, D.; Krull, U. J. Modeling of DNA Hybridization Kinetics for Spatially Resolved Biochips. *Anal. Biochem.* **2003**, *317* (2), 186−200.

https://dx.doi.org/10.1021/acs.biomac.9b01515
Biomacromolecules XXXX, XXX, XXX−XXX

Supporting information

Toehold length of target ssDNA affects its reaction-diffusion behavior in DNA-responsive DNA-co-acrylamide hydrogels.

Eleonóra Parelius Jonášová, Astrid Bjørkøy and Bjørn Torger Stokke.

Biophysics and Medical Technology, Dept of Physics, NTNU The Norwegian University of Science and Technology, NO-7491 Trondheim, Norway.

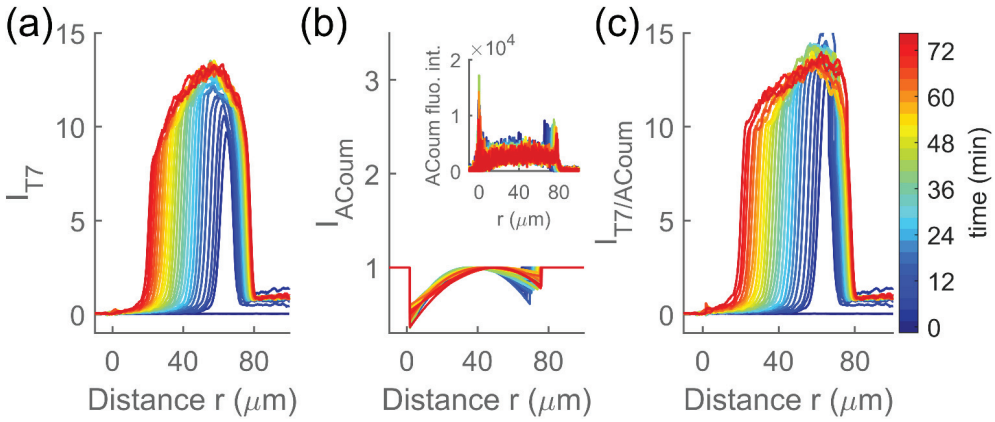

Figure S1 Aam-coumarin was included to be used as internal reference in ratiometric fluorescence imaging of Alexa Fluor 647 labelled target DNA. This Figure shows the correcting of the fluorescence intensity profiles of target DNA profiles in DNA-co-acrylamide hydrogels for the optical effect caused by the presence of the fiber using Coumarin labeled acrylamide as internal reference. a) Profiles showing the fluorescence intensity acquired from Alexa Fluor 647 attached to T7 strand (I_{T7}), smoothed and normalized such that the intensity of the fluorescence of the free solution is 1. A profile is shown for every 3rd minute after addition of the T7 target DNA to 20 µM to the immersing aqueous buffer at t=0. b) Smoothed and normalized profiles

showing the fluorescence intensity from Aam-coumarin attached to the polyacrylamide network (I_{ACoum}) for the hydrogel used for the experiments in a) at corresponding times. The insert shows the profiles before smoothing. c) Intensity profiles from a) divided by reference profiles I_{ACoum} from b). Fiber end face at $r = 0$.

Use of FRET for monitoring of crosslink opening

In order to gain more insight into the kinetics of the toehold-mediated strand displacement within the hydrogels, we intended to use Fluorescein dT to monitor the triplex state of the SBT complex via its Förster resonance energy transfer (FRET) reaction with Alexa Fluor 647. When all three strands (S, B and T) are bound together during the toehold-mediated strand displacement, the two dyes are sufficiently close to undergo FRET. The Förster distances for the SBT complexes were estimated to be up to 5.8 nm for T7 and T7b and 7.8 nm for T3 where the B strand was labelled with fluorescein on the terminal G of the blocking region (Figure 2 in the main text), and assuming 0.34 nm per base pair of dsDNA and 0.676 nm per nucleotide of ssDNA.

However, the FRET measurement proved challenging, mainly because the quantum yield of Fluorescein dT is changing depending on whether it is bound to a single strand or double strand DNA (Figure S2b), thus making straightforward interpretations impossible.[1] Moreover, although we did observe a decrease in Fluorescein fluorescence intensity due to FRET, there was no subsequent recovery of this signal which would be expected ones the SBT complex dissociated and crosslink was opened (Figure S2a). This could be due to Fluorescein's stabilization effect on dsDNA, which could potentially stabilize the SBT complex and concomitantly prevent crosslink from opening.[2]

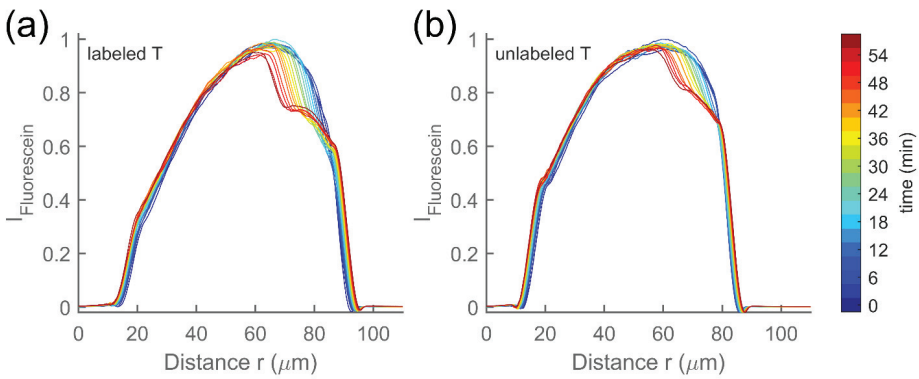

Figure S2 Spatio-temporal evolution of fluorescence intensity of Fluorescein dT dye attached to the B strand in SBF hydrogels after the addition of target strand T7 at concentration 20 µM to the hydrogel's immersing solution at t = 0. Profile shown for every 3rd minute. In a) 10% of the

target T7 is labeled with Alexa Fluor 647. When the target strand is bound in the SBT complex, the two dyes are in sufficient proximity for FRET to occur, i.e. fluorescein de-excitation occur partly via FRET to Alexa Fluor 647 and a decrease in the fluorescence from Fluorescein dT can be observed. However, as seen in b), where the target T7 is not labeled, there is also a decrease in fluorescence from Fluorescein dT which cannot in this case be explained by FRET, but can be attributed to changing quantum yield depending on whether it is bound to a double or single stranded DNA.

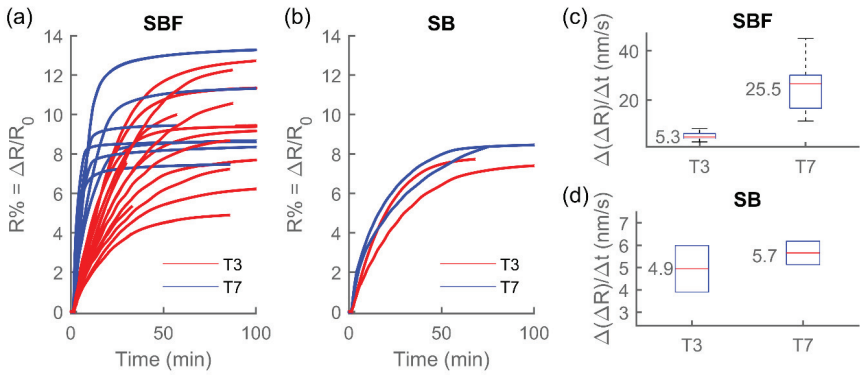

Figure S3 Relative swelling kinetics as determined by interferometry of SBF (a) and SB (b) hydrogels immersed in aqueous buffer solutions following an addition of either T7 or T3 to the immersing solution at a concentration of 20 μM. The individual lines represent repeat experiments performed on independently prepared hydrogels. Same data are used for averaging in Figure 8 in the main text. (c) and (d) show box plots of the initial rate of swelling at $t = 0$.

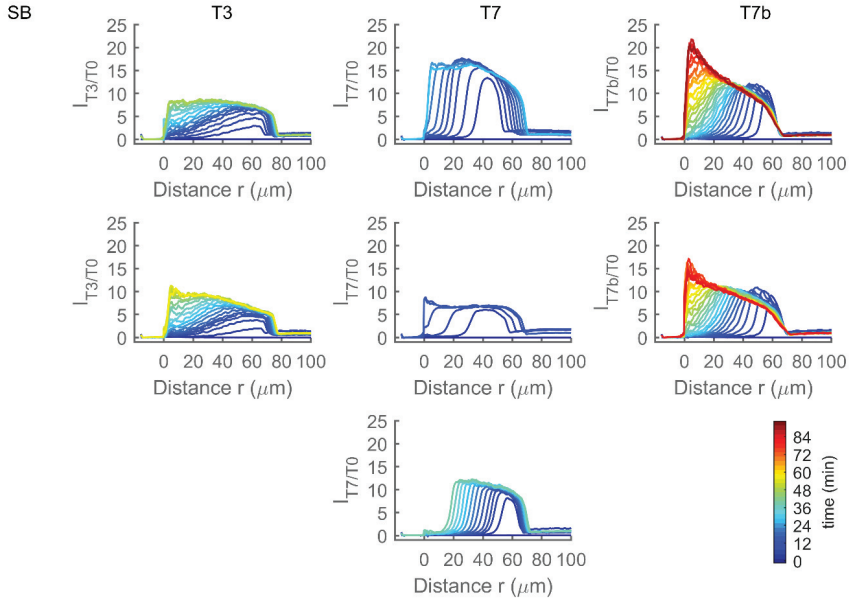

Figure S4 Spatio-temporal evolution of relative concentration of T3 (left), T7 (middle) and T7b (right) strands inside SB hydrogels. The individual plots depict individual independently prepared hydrogels. A profile is plotted for every 3rd minute. Fiber end face at $r = 0$.

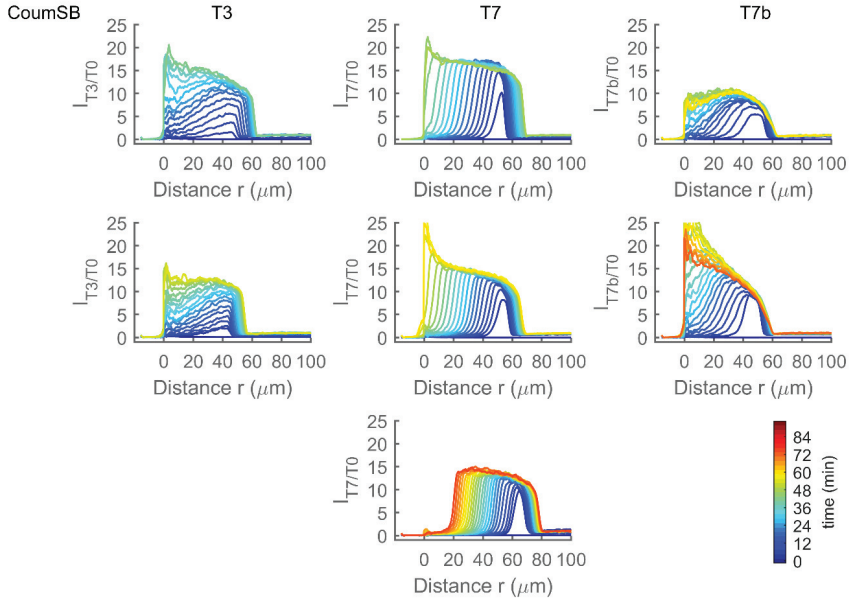

Figure S5 Spatio-temporal evolution of relative concentration of T3 (left), T7 (middle) and T7b (right) strands inside CoumSB hydrogels. The individual plots depict individual independently prepared hydrogels. A profile is plotted for every 3rd minute. Fiber end face at $r = 0$.

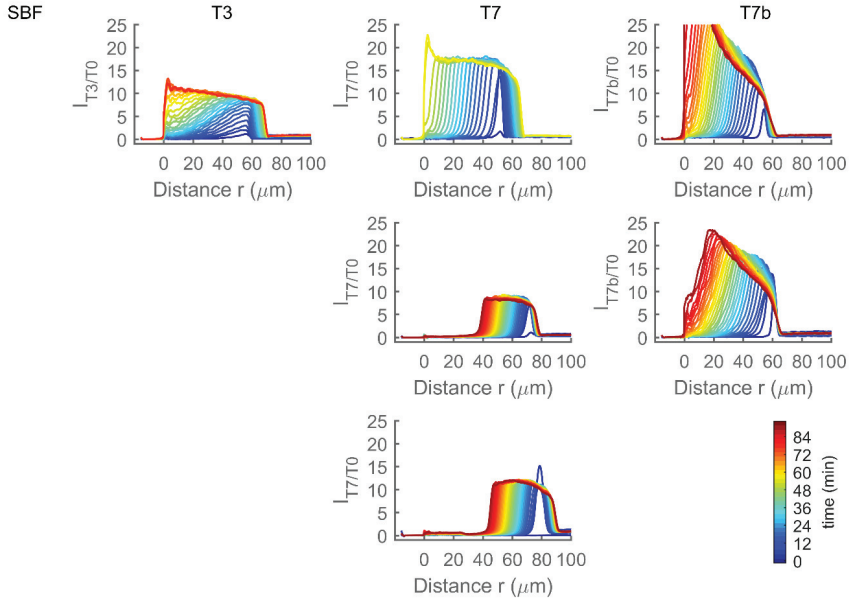

Figure S6 Spatio-temporal evolution of relative concentration of T3 (left), T7 (middle) and T7b (right) strands inside SBF hydrogels. The individual plots depict individual independently prepared hydrogels. A profile is plotted for every 3rd minute. Fiber end face at $r = 0$.

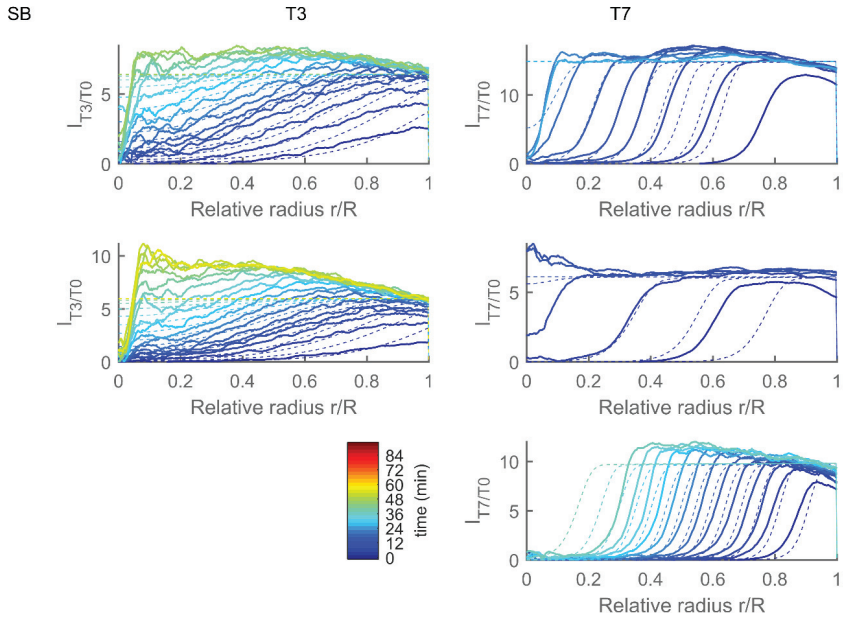

Figure S7 Spatio-temporal evolution of the relative concentration of targets (a) T3 and (b) T7 inside the same SB hydrogels as shown in Figure S4. In dotted lines, the profiles obtained by fitting the numerical reaction-diffusion model to the experimental data are shown. The individual plots depict individual independently prepared hydrogels. A profile is plotted for every 3rd minute. Fiber end face at $r = 0$.

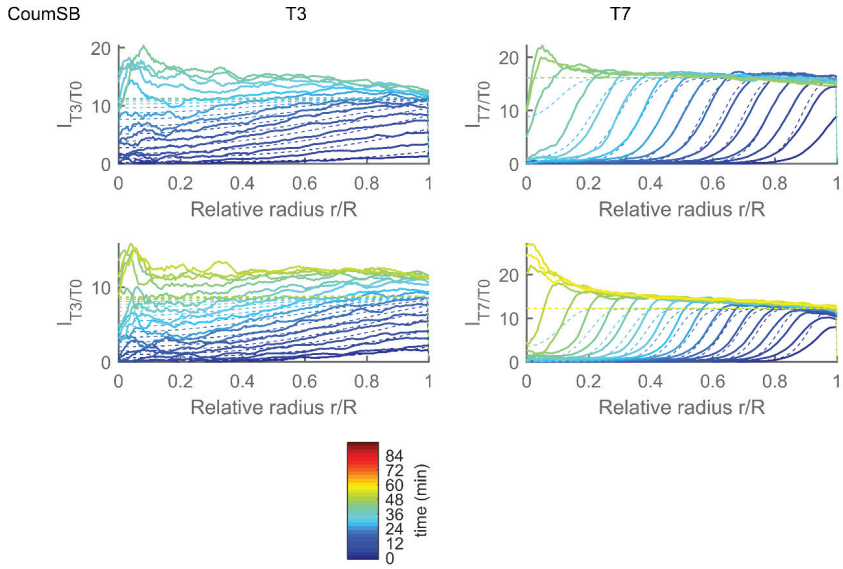

Figure S8 Spatio-temporal evolution of the relative concentration of targets (a) T3 and (b) T7 inside the same SB hydrogels as shown in Figure S5. In dotted lines, the profiles obtained by fitting the numerical reaction-diffusion model to the experimental data are shown. The individual plots depict individual independently prepared hydrogels. A profile is plotted for every 3rd minute. Fiber end face at $r = 0$.

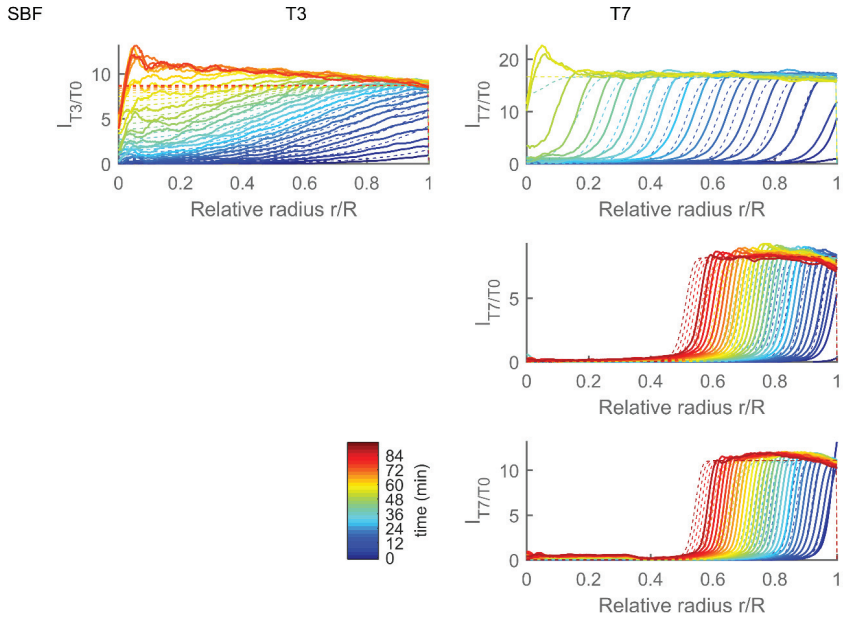

Figure S9 Spatio-temporal evolution of the relative concentration of targets (a) T3 and (b) T7 inside the same SB hydrogels as shown in Figure S6. In dotted lines, the profiles obtained by fitting the numerical reaction-diffusion model to the experimental data are shown. The individual plots depict individual independently prepared hydrogels. A profile is plotted for every 3rd minute. Fiber end face at $r = 0$.

References

1. Sjöback, R., Nygren, J. & Kubista, M. Characterization of Fluorescein – Oligonucleotide Conjugates and Measurement of Local Electrostatic Potential. *Biopolymers* **46**, 445–453 (1998).

2. Moreira, B. G., You, Y., Behlke, M. A. & Owczarzy, R. Effects of fluorescent dyes, quenchers, and dangling ends on DNA duplex stability. *Biochem. Biophys. Res. Commun.* **327**, 473–484 (2005).

Paper IV

polymers

MDPI

Article

Cascading molecular processes in oligo-morpholino functionalized responsive hydrogels

Eleonóra Parelius Jonášová[1], Bjørn Torger Stokke [1,*]

[1] Biophysics and Medical Technology, Dept of Physics, NTNU - Norwegian University of Science and Technology, NO-7491 Trondheim, Norway

* Correspondence: bjorn.stokke@ntnu.no

Received: date; Accepted: date; Published: date

Abstract: Responsive hydrogels featuring DNA as a functional unit are attracting increasing interest due to combination of versatility and numerous applications. However, some applications would benefit from altering certain DNA properties. In the present work, the commonly employed DNA oligonucleotides in DNA-co-acrylamide responsive hydrogels are replaced by Morpholino oligonucleotides. The uncharged backbone of this nucleic acid analogue makes it less susceptible to possible enzymatic degradation. In this work we address fundamental issues related to key processes in the hydrogel response; such as partitioning of the free oligonucleotides or the strand displacement process. The hydrogels were prepared at the end of optical fibers for interferometric size monitoring and imaged using confocal laser scanning microscopy of the fluorescently labeled free oligonucleotides to observe their apparent diffusion and accumulation within the hydrogels. Morpholino-based hydrogels' response to Morpholino targets was compared to DNA hydrogels' response to DNA targets of the same base-pair sequence. Morpholino hydrogels were observed to have larger partition coefficients for non-binding targets than DNA hydrogels, due to their electroneutrality, resulting in faster kinetics for Morpholinos. The electroneutrality, however, also led to the total swelling response of the Morpholino hydrogels being smaller than that of DNA, since their lack of charges eliminates swelling resulting from the influx of counter-ions upon oligonucleotide binding. We have shown that employing nucleic acid analogues instead of DNA in hydrogels has a profound effect on the hydrogel response.

Keywords: Oligo-morpholino-co-Aam hydrogels; responsive hydrogel; interferometric readout;

1. Introduction

DNA-based responsive hydrogels are a promising group of materials capable of adapting their properties to the presence of various molecular targets in their environment, ranging from DNA [1–3] and other organic molecules [4–6], through ions [7–10] to viruses [11] and cells [12,13]. The mechanism of recognition relies on the ability to synthetize a custom DNA base sequence, which controls the structure of the DNA molecule down to nanolevel; and on the Watson-Crick complementarity rules that govern the base pairing and through it interactions with other DNA or non-DNA (via aptamer interactions) molecules. DNA thus offers remarkable sensitivity and specificity in its interactions and the hydrogel provides a means to amplify the molecular signal to a microscopic length scale. The possible applications are in sensing [4,10,14,15], targeted drug delivery [16–18], as well as in tissue engineering and as soft devices [1,19–21].

One of the DNA hydrogel designs for sensing applications was introduced in 1996 by Nagahara and Matsuda [22] and further investigated in our group [23,24]. The hydrogels in question consist of a dual crosslinked polyacrylamide network (**Figure 1**), in which the covalently crosslinked polyacrylamide carries oligonucleotide-based physical crosslinks that can be opened in a process of toehold-mediated strand displacement [25]. In short, the oligonucleotide crosslinks are formed by

two 5′acrydite-functionalized oligonucleotides that have a complementary region at their 3′ ends. The strands form a partially hybridized duplex and the acrydite allows them to be incorporated through covalent bonds into the hydrogel network as an additional crosslink. This crosslink can be disrupted by the binding of a target oligonucleotide *T*, which is complementary to one of the crosslinks strands – sensing strand *S*. Nearly the whole complementarity region between *S* and *T* is blocked by the other crosslink strand – the blocking strand *B*. The bases that are complementary to *T*, but not blocked by *B*, form the toehold – a domain available for the initial binding of the target. The binding is then followed by a migration of the junction point along the length of the *S* strand, until the strand *B* is entirely displaced.

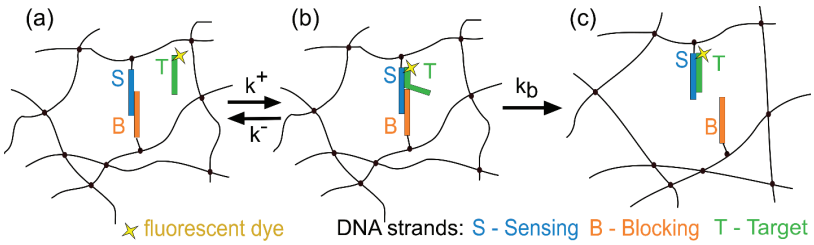

Figure 1 Dual-crosslinked polyacrylamide and nucleic acid (analogue) based hydrogel. In **(a)** the initial state of the crosslink composed of sensing and blocking strand, along with the free fluorescently labelled target. The target can bind **(b)** or dissociate from the crosslink with binding and dissociation rate constants k^+ and k^-. Ultimately, **(c)** the blocking strand is entirely displaced after branch migration (k_b).

In recent years, synthetic nucleic acids have been explored in preparation of responsive hydrogels [26], in order to overcome some of the drawbacks of native DNA molecules, such as its high charge and subsequent salt dependence or susceptibility to degradation by enzymes. Morpholino oligonucleotides (MOs) are particularly promising due to their uncharged backbone, but high solubility. The solubility can be attribute to their well stacked nucleobases. In fact, the stacking is better than that of DNA [27], yielding very good solubility (as an example, 263 mg of a Morpholino 22-mer was dissolved in 1 mL of water without reaching saturation [28]). They are also resistant to nucleases and stiffer than DNA, minimizing self-hybridization. Their melting temperature is slightly higher than that of DNA strands of corresponding sequence.

Employing MOs instead of DNA in the above described hydrogels provides the advantage of electroneutrality, thus eliminating the electrostatic interactions between the hydrogel and the target. Electrostatic interactions contribute to the partitioning of solutes in gels and thus affect their transport. The partition coefficient is defined as a ratio of the solute's concentration inside the gel c_{gel} and in the immersing solution c_{sol} at equilibrium:

$$\mathrm{K} = \frac{C_{gel}}{C_{sol}}. \quad 1$$

It depends on the size and conformation of the solute and the hydrogel and on their various interactions. If these interactions are considered independent, they can be separated into individual contributions [29]:

$$ln\mathrm{K} = lnK_{el} + lnK_{hphob} + lnK_{biosp} + lnK_{size} + lnK_{conf} + lnK_o \quad 2$$

where *el*, *hphob*, *biosp*, *size*, *conf* and *o* denote, respectively, interactions of electrostatic, hydrophobic, biospecific affinity, size-related and conformational nature, and other interactions.

The size and conformation addition to the partition coefficient has been derived by Ogston [30], based purely on hard sphere interactions (i.e. without electrostatic, hydrophobic and biospecific

interactions). The model is derived by placing spheres of radius a (solute) in a matrix of long cylindrical fibers of radius a_f, with a total volume fraction φ:

$$K_{size,conf} = e^{-\phi\left(1+\frac{a}{a_f}\right)^2}. \quad (3)$$

In the present study, we extend from the previous investigations employing dsDNA oligonucleotides to MOs as physical crosslinks alongside the covalent ones in the responsive hydrogels. The overall aim is to determine the mutual influence between the various processes, namely target diffusion and binding, physical crosslink disruption and swelling. A notable difference between the physical crosslinks in MO- and DNA-based hydrogels are the uncharged MOs as compared to the highly charged DNA, implying that one can expect significant differences in the electrostatic contribution to the partition coefficient. The polyanion character of DNA contributes to exclusion of the target from the DNA hydrogel and as a result its slower uptake. Thanks to the electrically neutral backbone of MOs, an increased partitioning is expected, improving the kinetics of the target transport. The MO-polyacrylamide hydrogels are investigated as fabricated on an optical fiber supporting high resolution monitoring of net change in the optical length. This realization also indicates that MO-polyacrylamide hydrogels possess potential as sensing and transducing materials, and although only mRNA sensing proof-of-concept so far has been reported [26], such applications also take advantage of the improved stability of MOs towards enzymatic degradation.

Interferometry and confocal laser scanning microscopy were used to monitor the swelling of the Morpholino hydrogels as well as the uptake of the target within. The swelling was also compared to that of DNA hydrogels of identical nucleotide sequences.

2. Materials and Methods

2.1. Materials

Acrylamide ≥ 99% (Aam), N, N'-methylenebisacrylamide ≥ 99.5% (Bis), squalane oil, dimethyl sulfoxide (DMSO), 3-(trimethoxysilyl) propyl methacrylate 98% (linker), 1-hydroxycyclohexyl phenyl ketone 99% (HCPK) and 2-amino-2-hydroxymethyl-propane-1,3-diol (Tris) were purchased from Sigma-Aldrich; ethylenediaminetetraacetcic acid (EDTA) and sodium chloride (NaCl) were obtained from VWR. Single-stranded Morpholino oligonucleotides and DNA oligonucleotides with custom specified base pair sequence (Table 1) (some functionalized with an acrydite group, some fluorescently labelled at specific base) were obtained from Gene Tools (Philomath, USA) and Integrated DNA Technologies (IDT, Coralville, USA) respectively. All materials were used without further purification. De-ionized water with resistivity 18.2 MΩ cm (Millipore Milli-Q) was used throughout.

Table 1 Oligonucleotide sequences of the sensing, blocking and target strands, with the position of acrydite groups (Acr) shown and the nucleobases complementary with sensing strand highlighted. Each sequence was realized both as MO and DNA oligonucleotides.

Name	*Sequence*	*# bases*
S	3′ C GTA AGT AAC TAT CGA CTT CAG TCG TCA- Acr 5′	28
B	5′ Acr - TTC AGT CGT CAG CAT TCA TTG ATA GGA C 3′	28
T2	5′ G CAT TCA TTG ATA GCT AAT GAC ATA 3′	25
T10	5′ G CAT TCA TTG ATA GCT GAA GTC AGA 3′	25
T0	5′ TAT CGT AGC AGG CTA CAG GAC TCA A 3′	25

2.2. Pregel and target solutions

An aqueous buffer prepared from 10 mM Tris, 1 mM EDTA and 150 mM NaCl, adjusted to pH 7.5 was used for preparation of pregel and solutions containing target Morpholinos or DNA oligonucleotides.

Pregel solutions consisted of 10 wt% Aam, 0.6 mol% Bis, 0.13 mol% HCKP and 0.4 mol% ds DNA or dsMO (duplex SB), dissolved in buffer. HCPK was dissolved in DMSO to the concentrations of 0.1 M prior to its addition to the pregel solution. Two different types of hydrogels were prepared MO hydrogels and DNA hydrogels, differing solely by whether the oligonucleotides incorporated were Morpholinos or DNA.

Stock solutions of target ssDNA and ssMO were prepared by dissolving strands *T0*, *T2*, or *T10* in buffer to a concentration of 30 μM. The target stock solutions were prepared from 90% unlabeled and 10% labelled target oligonucleotides (labelled with Carboxyfluorescein for MOs, Fluorescein for DNA, or for some DNA hydrogels with Alexa Fluor 647).

2.3. Gel preparation

Quasi-hemispherical hydrogels were prepared at the end face of optical fibers (SMF-28-J9 from ThorLabs, diameter without coating 125 μm) that have been stripped of the coating. The end of the fiber was cut (cutter: Fitel model S323, Furukawa Electric Co. Ltd.), cleaned with ethanol and functionalized with methacrylate groups by silanization. The silanization procedure consisted of treating the fiber with 0.1 M HCl solution for 20 minutes and then immersing in a 2 vol% solution of linker in degassed MiliQ water adjusted to pH 3.5. Fibers were again cleaned with ethanol and dust was removed from the end face using duct tape.

The end of the optical fiber was then immersed in a squalane oil droplet saturated with 2.6 mg/mL of HCPK. A pipette was used to deposit a small amount of the pregel solution (~0.3 nL) at the end face of the fiber. The pregel was polymerized via a free radical polymerization initiated by exposure to UV light for 5 minutes (Fiber coupled LED UV source M340F3, nominal wavelength 340 nm, ThorLabs).

2.4. Interferometry

An interferometric readout method described in detail elsewhere[31] was used to monitor the optical length of the hydrogels. In short, a light wave (1530-1560 nm) is sent through the hydrogel which constitutes a Fabry-Perot cavity and the interference of the waves reflected at the fiber-hydrogel and hydrogel-solution interfaces is used to determine the optical length of the hydrogel L as well as the change in its optical length ΔL. Relative swelling $L\%$ can be calculated as a change in optical length relative to the initial optical length L_0 (optical length immediately prior to the addition of the target): $L\% = \Delta L / L_0$.

2.5. Confocal Laser Scanning Microscopy

Confocal laser scanning microscopy was used for monitoring of the spatiotemporal distribution of the target within the hydrogel. For this purpose, the fiber with the hydrogel at its end face was pinched of with tweezers and glued to a bottom of a Glass Bottom Microwell Dish (P35G-1.5-10-C) from MatTek. The hydrogel was then left to equilibrate in 100 μL of the buffer solution before 200 μL of 30 μM target stock solution was added immediately before the imaging was started to a final target concentration of 20 μM.

The imaging was performed using a Confocal Laser Scanning Microscope (Zeiss LSM800) with a 40x, NA=1.2 water immersion objective (optical slice thickness of 0.9 μm) at 22°C. A micrograph was acquired in a horizontal plane passing through the middle of the hydrogel (depth ~62 μm) every minute, starting 10-20 seconds after the addition of the target. Excitation wavelength of 480 nm was used for Fluorescein with a detection bandpass filter of 500-700 nm. For Alexa Fluor 647, excitation wavelength was 640 nm and the detected fluorescence was filtered by a bandpass filter of 650-700 nm.

2.6. Acquiring relative concentration profiles from CLSM micrographs

Fluorescence intensity profiles were extracted from the CLSM micrographs using custom Matlab R2017a (Mathworks) scripts. Intensity profiles were acquired over several lines from a circular sector spanning 20° around the long axis of the fiber with a 0.5° step. These profiles were then averaged to obtain a smoother fluorescence intensity profile representative of the fluorescence intensity along the axis of the fiber.

The profile was then smoothed using a Savitzky-Golay filter and normalized so that the intensity of the immersing solution was 1 (for *T2* and *T10*), or so that the maximum intensity within the hydrogel was 1 (for *T0*). These fluorescence intensity profiles are referred to as I_{TX}, where *TX* is one of the targets *T0*, *T2* or *T10*.

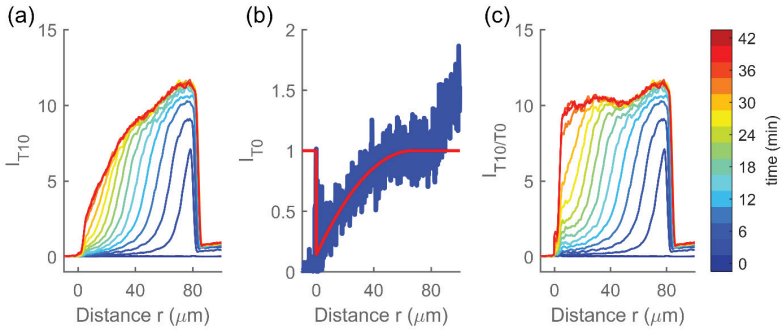

Figure 2 (a) An example of fluorescence profiles I_{T10} recorded by CLSM after addition of target *MO-T10* to a MO hydrogel (angle-averaged, smoothed and normalized to immersing solution being 1). **(b)** The fluorescence intensity I_{T0} of the same hydrogel immersed in a nonbinding target *MO-T0* in blue and a reference profiled obtained by a second-degree polynomial fit to I_{T0} shown in red. **(c)** Fluorescence intensity profiles I_{T10} from (a) divided by the reference profiles form (b), to obtain the relative intensity profiles corrected for the effect of the presence of the fiber, i.e. relative concentration $I_{T10/T0}$. Fiber end face is located at $r = 0$.

The close proximity of the glass fiber to the hydrogel affects the detected fluorescence intensity, i.e. the refraction of excitation and emission light through the fiber causes a decrease in the observed fluorescence that is the most pronounced at the fiber end face and reaches as far as 50 μm into the hydrogel/solution.[32] Due to this effect of the fiber, the fluorescence intensity profiles do not reflect the concentration of the target. To correct for this, an intensity profile I_{T0} in the non-binding target *T0* was obtained for each individual hydrogel and used as reference for quantifying the effect of the fiber on the fluorescence intensity (**Figure 2**). The concentration of the target inside the hydrogel relative to that in the immersing solution can then be obtained by dividing the fluorescence intensity profiles I_{T2} and I_{T10} by the reference profile I_{T0} for each individual hydrogel. The relative concentration profiles are referred to as $I_{TX/T0}$ where *TX* is one of the targets *T2* or *T10*.

Relative swelling $R\% = \Delta R/R_0$ was also calculated from the obtained relative concentration profiles $I_{TX/T0}$. The outer edge of the hydrogel was identified as the position with largest negative slope (obtained by numerical differentiation of the profile), while the inner edge at the fiber end face was identified visually.

2.7. Reaction-diffusion model

The binding of the target to the hydrogel-bound strands and the subsequent crosslink opening can be modelled as a two-step process characterized by the binding constant k^+, the dissociation constant k^- and the constant of junction point migration k_b (**Figure 1**). The total molar concentration of available binding sites, i.e. *SB* duplexes available to bind the target is m_t. The concentrations of free binding sites m_f, 3-strand complexes m_c and open crosslinks m_o add up to the total concentration m_t. Apart from the

reaction between the duplex and the target, the target is undergoing diffusion into and through the hydrogel.

The following partial differential equations for diffusion-reaction in a sphere describe the evolution of the concentration of the free target c, as well as the concentrations of binding sites m_c and m_o at a given relative radial position $\hat{r} = r/R$ (where r is the radial position and R the radius of the sphere) at time t [33]. The concentration of target at the boundary is $c_{out} = K\, c_{sol}$ and $\alpha = \frac{D}{R^2} > 0$.

$$\frac{\partial c}{\partial t} = \frac{\alpha}{\hat{r}^2}\frac{\partial}{\partial \hat{r}}\left(\hat{r}^2 \frac{\partial c}{\partial \hat{r}}\right) - k^+ c m_t + k^+ c m_c + k^+ c m_o + k^- m_c \quad (4)$$

$$B.C.: \frac{\partial c(0,t)}{\partial \hat{r}} = 0, \quad t \geq 0 \quad (5)$$

$$c(1,t) = c_{out} \quad (6)$$

$$I.C.: c(\hat{r},0) = \begin{cases} 0, & 0 \leq \hat{r} < 1 \\ c_{out}, & \hat{r} = 1 \end{cases} \quad (7)$$

$$\frac{\partial m_c}{\partial t} = k^+ c m_t - k^+ c m_c - k^+ c m_o - k^- m_c - k_b m_c \quad (8)$$

$$B.C.: \frac{\partial m_c(0,t)}{\partial t} = 0 \quad (9)$$

$$m_c(1,t) = 0 \quad (10)$$

$$I.C.: m_c(\hat{r},0) = 0, \quad 0 \leq \hat{r} \leq 1 \quad (11)$$

$$\frac{\partial m_o}{\partial t} = k_b m_c \quad (12)$$

$$B.C.: \frac{\partial m_o(0,t)}{\partial t} = 0 \quad (13)$$

$$m_o(1,t) = 0 \quad (14)$$

$$I.C.: m_o(\hat{r},0) = 0, \quad 0 \leq \hat{r} \leq 1 \quad (15)$$

This system of partial differential equations can be numerically solved by applying the method of lines and discretizing the spatial dimension to reduce the problem to a system of ordinary differential equations [34].

The mathematical diffusion-reaction model was then fitted to experimental data, with parameters α, k^+, k^-, k_b, m_t being determined in the fitting. Another parameter, t_{delay}, was also determined in the fitting and accounts for the time delay between the addition of the target solution to the hydrogel's immersing solution and the start of the scanning. The swelling was not considered in the model fitting and the experimental size of the hydrogel has been approximated by its initial radius R_o.

3. Results and discussion

3.1. Swelling rate and equilibrium depends on the toehold length and differs between DNA and MO

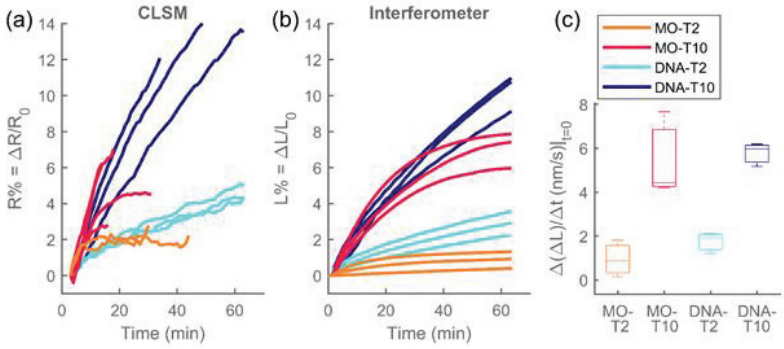

Figure 3 Relative swelling kinetics of Morpholino and DNA hydrogels after exposure to Morpholino and DNA targets *T2* or *T10* respectively at $t = 0$. In **(a)**, relative swelling as calculated from CLSM micrographs, reflecting changes in the hydrogel's physical length. In **(b)**, relative swelling obtained by interferometry, reflecting the optical length changes. In **(c)**, box plots of initial swelling calculated from the interferometer curves.

The swelling was monitored both via interferometry and via confocal laser scanning microscopy. The interferometer measures the optical length L of the hydrogel with high precision [31], while the physical length R is directly determined from CLSM micrographs with lower precision, (as can also be seen by the CLSM data showing more noise in **Figure 3**a, compared to smooth interferometer data in **Figure 3**b). In **Figure 3** relative swelling curves for several parallel hydrogel preparations are shown as measured by the interferometer or the CLSM. The initial swelling rate at time $t = 0$ was calculated from the interferometer data and shown in **Figure 3**c.

Similar trends can be observed between interferometric and CLSM data, but the optical length change (interferometer) seems to be smaller than the change in the physical length (CLSM) which could be attributed to the changes in refractive index, brought on by swelling, but it could also be due to a measurement error, since the edge of the fiber in the micrographs was identified visually and thus introduced a human error and bias.

MOs are consistently seen to reach their equilibrium swelling state within or shortly after 60 minutes, while DNA hydrogels are swelling for several (2-4) hours. The equilibrium swelling is also much larger for DNA hydrogels than for the MO hydrogels, while their initial swelling rates differ much less (**Figure 3**c). While the absolute swelling rates as depicted in **Figure 3** are similar for Morpholinos and DNA, the fact that DNA hydrogels reach their equilibrium much later means that their relative swelling rate is slower. The limited swelling of MO hydrogels compared to those with DNA can be attributed to the lack of electrostatic interactions, meaning that no influx of counterions (and solvent) accompanies the binding of the MO to the hydrogel.

There is a significant difference in the swelling rate and the equilibrium swelling volume depending on the length of the toehold, both in the case of Morpholino oligonucleotides and DNA oligonucleotides. The target *T10* leads to a faster and more pronounced swelling than *T2*.

3.2. The effect of charges and fluorescent dyes on partitioning

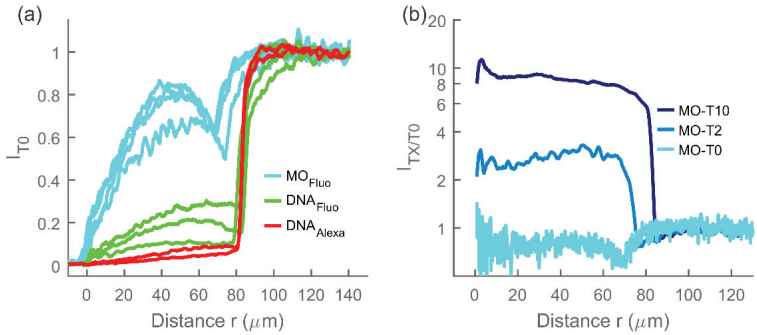

Figure 4 (a) Normalized fluorescence intensity profiles I_{T0} of non-binding target *T0* (either MO-*T0* or DNA-*T0*) in MO hydrogels and DNA hydrogels respectively. MOs were functionalized with Carboxyfluorescein dye and DNA oligonucleotides were functionalized either with Fluorescein or Alexa 647. **(b)** Relative concentration profile $I_{T0/T0}$ of non-binding target *T0*, compared to equilibrium (or near-equilibrium) relative concentration profiles of binding targets *T2* and *T10* ($I_{T2/T0}$ and $I_{T10/T0}$). The individually prepared hydrogels for these data extent up to r =66 μm, 72 μm and 82 μm for the nonbinding T0 and T2 and T10 binding targets, respectively.

Fluorescence intensity profiles I_{T0}, uncorrected for the presence of the fiber, are shown in Figure 4a for non-binding target *T0* (either Morpholino or DNA) in corresponding (Morpholino or DNA) hydrogel. In case of DNA, two different fluorescent dyes, attached at the same location in the nucleotide sequence, were tested: 3′-Alexa Fluor 647 and 3′-Fluorescein. Morpholinos were only labelled using 3'-Carboxyfluorescein.

The partition coefficient, calculated as the ratio of maximum fluorescence intensity inside the hydrogel relative to the immersing solution, has been calculated for each experiment and averaged for the same targets. The obtained values were $K = 0.77, 0.22,$ and 0.06 for Carboxyfluorescein labeled MOs, Fluorescein-labelled DNA, and Alexa Fluor 647-labelled DNA oligonucleotides, respectively.

The size contribution to the partition coefficient K_{size} can be approximated by the Ogston formula (Equation (3)). The parameter a can be approximated by the radius of gyration of a single stranded DNA of 25 base pairs to a = 3 nm [35] (this value would be somewhat larger for MOs, claimed by others to be stiffer than DNA [26]) and using experimentally determined volume fraction $\phi = 0.06$, and fiber radius $a_f = 0.8$ nm from Williams at al [36] for polyacrylamide, we would expect the size contribution to the partitioning coefficient to be $K_{size} = 0.26$ for DNA and slightly lower for Morpholinos.

Since Morpholino oligonucleotides have an electrically neutral backbone, the electric potential contribution to the partition coefficient is eliminated as compared to corresponding DNA hydrogels in which the electrostatic repulsion is leading to greater exclusion of the target from the hydrogels. The MOs however appear to have other interactions with the hydrogel, since their partition coefficient is larger than the estimate of the size contribution alone, suggesting a reaction favoring the uptake of MOs. This could be attributed to hydrophobic interactions, as Morpholinos have been reported to exhibit interactions with hydrophobic molecules most likely due to their own hydrophobic nature [37,38].

We can also observe a difference in partitioning for the DNA strands labelled with different fluorescent dyes, namely Fluorescein-labeled DNA exhibiting a larger partition coefficient than Alexa Fluor 647-labeled DNA (Figure 4a). Such an effect on partitioning could be a result of hydrophobic

or electrostatic interactions as well as due to the dye's effect on the size and conformation of the DNA-dye complex.

3.3. Toehold effect on target spatiotemporal distribution in the MO hydrogels

In Figure 4b the relative concentration profile of the non-binding MO-*T0* in MO hydrogels is compared to the equilibrium (or near-equilibrium for MO-*T2*) relative concentration profiles of binding targets MO-*T2* and MO-T*10* in MO hydrogels. While the non-binding target's concentration in the hydrogel is below that of the immersing solution, the binding targets MO-*T2* and MO-*T10* are accumulating to approximately 3 and 9 times, respectively, their concentrations in the immersing solution. This difference between binding and non-binding targets reflects the biospecific interaction between the target and hydrogel-bound oligonucleotides with which they were designed and which supports their possible applications. The targets with longer toeholds (MO-*T10*) are showing more accumulation at equilibrium than those with shorter toeholds (MO-*T2*), a difference that was also reflected in their equilibrium swelling volumes (Figure 3).

Figure 5 shows the spatiotemporal evolution of the MO target in several parallel MO hydrogel preparations as measured by CLSM. Both targets are seen to quickly (within 3 minutes) accumulate inside the hydrogels to levels higher than those in the immersing solution. MO hydrogels exposed to *T10* have reached saturation at 8 – 12 times the concentration of the immersing solution, while MO hydrogels immersed in *T2* solution have not reached an equilibrium yet in the duration of the experiment and have reached a maximum concentration of 3-4 times that of the immersing solution. However, from the swelling measurements (**Figure 3**), a swelling equilibrium was reached by this time, especially for *T2* targets.

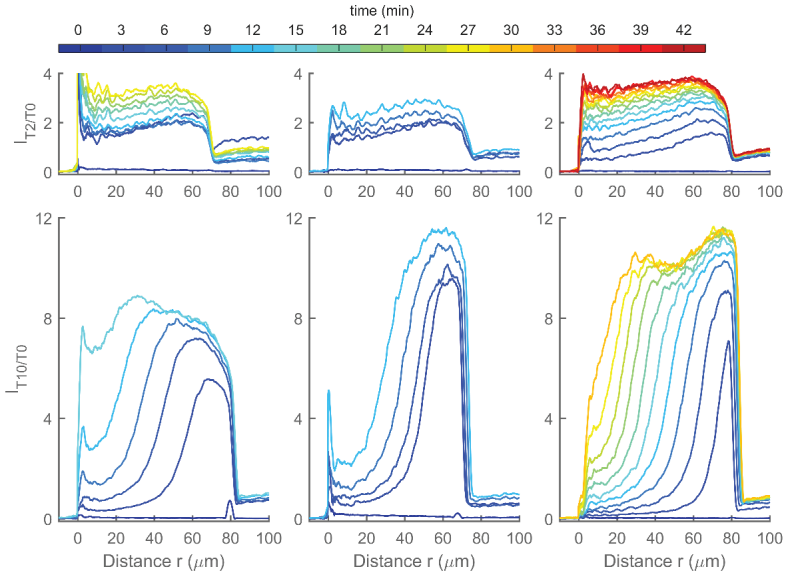

Figure 5 Spatiotemporal evolution of relative target (Carboxyfluorescein-labelled MO-*T2* or MO-*T10*) concentrations $I_{T2/T0}$ and $I_{T10/T0}$ after exposure of MO hydrogels to the target solution at approximately $t = 0$. A profile is plotted for every 3rd minute. Individual plots show parallel hydrogel preparations, with hydrogel response to *T2* on the left and *T10* on the right.

A difference in the spatiotemporal distribution pattern can be seen for the two different toehold lengths of the targets. While target *T2* is filling up the hydrogel almost uniformly throughout its volume, target *T10* first saturates the outermost layer of the hydrogel, leading to a sharp concentration change in the hydrogel and this boundary then shifts further towards the center of the hydrogel as each new layer becomes saturated with the *T10* target. This difference suggests that similarly to toehold-mediated strand displacement of DNA [25], the dissociation constant strongly depends on the length of the toehold also for MOs, with the dissociation constant of *T2* being larger than that of *T10*. *T10* binds strongly to the SB duplex and does not readily dissociate, which prevents the targets from penetrating far into the hydrogel before all the available binding sites are occupied. On the other hand, *T2* which dissociates much more easily is quickly released after binding and free to diffuse further into the hydrogel before another binding occurs.

DNA hydrogels were also exposed to DNA targets (DNA-*T2* and DNA-*T10*) and imaged using CLSM (**Figure 6**). Compared to MOs, DNA hydrogels are swelling slower and exhibit a steeper concentration gradient moving inside the hydrogels, both in case of T2 and T10 targets. Unexpectedly, the concentration is seen to be increasing in the part right of the moving wavefront also for DNA-*T10*, instead of quickly reaching a plateau, as was observed in the case of MOs. This behavior cannot be explained by the association, dissociation and crosslink opening processes as described in the reaction-diffusion model and suggests another phenomenon taking place in these hydrogels. Additional experiments mapping effects of toehold molecular parameters are also reported elsewhere [24, Paper III]. However, an explicit comparison between the various sets of data is challenging due to differences in concentrations of immobilized dsDNA crosslinks and possible differences brought on by the presence of various fluoroprobe labels.

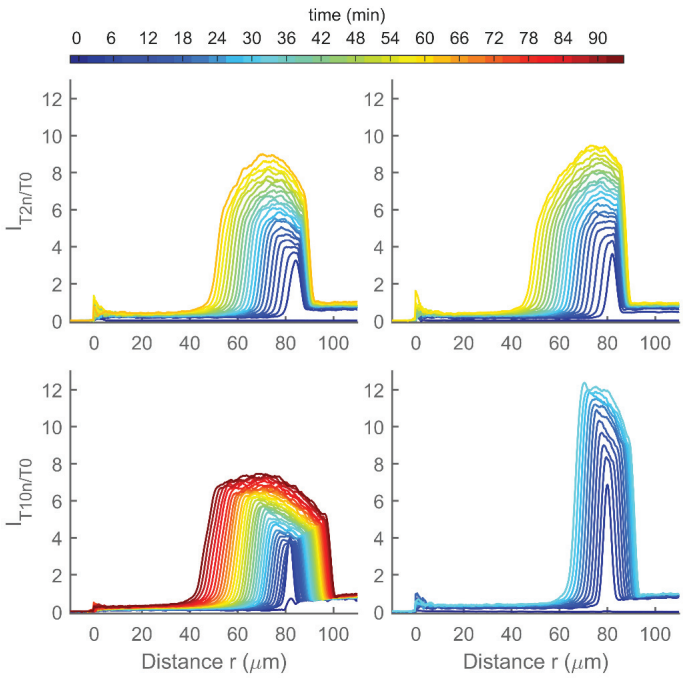

Figure 6 Spatiotemporal evolution of relative target (Fluorescein labeled DNA-*T2* or DNA-*T10*) concentrations $I_{T2/T0}$ and $I_{T10/T0}$ after exposure of DNA hydrogels to the target solution at approximately $t = 0$. A profile is plotted for every 3rd minute. Individual plots show parallel hydrogel preparations, with hydrogel response to *T2* on the left and *T10* on the right. Note: The time scale is different than that in Figure 5.

3.4. Estimating target T10 and hydrogel properties from diffusion-reaction modelling

We have fitted the obtained relative concentration profiles for MO-*T10* targets in MO hydrogels ($I_{T10/T0}$) to the reaction-diffusion model described in Methods. Since the hydrogels exposed to MO-*T2* did not reach a maximum concentration within the hydrogel, the fitting was less reliable, and the optimization yielded local minima depending on the starting conditions and these results are not included.

An example of the model fitted to the experimental data is shown in **Figure 7**. Fitting was repeated for all the MO hydrogels shown in **Figure 5**b and the obtained fitting parameters were averaged to estimate the characteristic properties of the MO-*T10* target and MO hydrogels (**Table 2**). The table also contains the theoretical values of association and dissociation rate constants as modelled by Zhang and Winfree for DNA in solution [25]. The theoretical value for diffusion coefficient is also estimated for a DNA oligonucleotide: DNA of 25 bases has a diffusion coefficient in solution of approximately 130 μm²/s [39], which is expected to be reduced to approximately to 16% of its value when in a hydrogel [40], giving value of approximately 21 μm²/s. The theoretical concentration of the binding sites is estimated from the concentration of SB duplexes in the pregel solution, which is 5.64 mM, but due to the initial swelling of the polymerized hydrogels, this is reduced to approximately 4 mM at the beginning of the experiment.

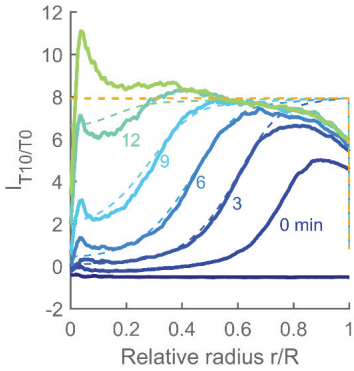

Figure 7 Spatiotemporal evolution of relative target (Carboxyfluorescein-labelled MO-*T10*) concentration $I_{T10/T0}$ after exposure of an MO hydrogel to the target solution at approximately $t = 0$ (Same hydrogels as pictured in first row of **Figure 5**). A profile is plotted for every 3rd minute. In dotted lines, the profiles obtained by fitting the numerical reaction-diffusion model to the experimental data.

Morpholino hydrogels are showing a smaller diffusion coefficient than estimated for DNA of the same length in a hydrogel of this composition. This could be accounted for by the reported higher stiffness of Morpholinos, but it could also suggest that the attached fluorescent dye affects the diffusion [41]. Concerning the apparent concentration of the binding sites, the hydrogels showing saturation at 0.18 mM suggests that only a small fraction (≈ 5%) of the duplexes is available for binding the target.

As seen in **Table 2**, the rate constants also differ significantly from those for DNA in solution, suggesting that the kinetics of toehold exchange is affected by the changes to the backbone and that data estimated for DNA cannot be directly applied to Morpholinos, despite having the same base sequence.

Table 2 Parameters obtained by fitting the reaction-diffusion model to the CLSM data for MO-*T10* spatiotemporal distribution in MO hydrogels.

Parameter	*Average value (of 3) ± standard deviation*	*Theoretical values*
Diffusion coefficient D (μm²/s)	10 ± 2	21 ([a])
Association rate constant k^+ ($M^{-1}s^{-1}$)	$10^{3.2\pm0.2}$	3×10^6 ([b])
Dissociation rate constant k^- (s^{-1})	0.947 ± 0.06	6×10^{-6} ([b])
Branch migration constant k_b (s^{-1})	3.1 ± 0.4	2 ([b])
Available binding site concentration m_t (mM)	0.18 ± 0.03	4 ([c])

a) Estimate for DNA of same length in polyacrylamide hydrogels [39,40]

b) Zhang and Winfree for DNA in solution [25]

c) Concentration of SB duplexes estimated from initial concentration in the pregel.

5. Conclusions

Nucleic acid analogues, such as Morpholino oligomers, provide opportunities to exploit the specificity and sensitivity of DNA interactions within hydrogels, while altering other properties of the molecule. Here we have employed Morpholino oligonucleotides as physical crosslinks within polyacrylamide hydrogels and compared their response to target MOs with the response of DNA hydrogels to corresponding DNA targets. Due to the uncharged backbone of MOs, we observed a higher partitioning coefficient of non-binding targets and improved kinetics for binding targets, as well as a less pronounce total swelling response. The dependence of the kinetics on the length of the toehold, known from DNA, was also observed for MOs. Lastly, by fitting the data to a reaction-diffusion model, we estimated the diffusion coefficient and the association, dissociation and branch migration rate constant for MO-*T10* and found that they differ significantly from those predicted for DNA.

Author Contributions: EPJ and BTS designed the experiments. EPJ performed the experiments, the data analysis and wrote the manuscript. Both authors revised the manuscript and approved the final version.

Acknowledgments: The authors gratefully acknowledge the skilled technical assistance of engineer Astrid Bjørkøy.

Conflicts of Interest: Authors declare no conflict of interest. The funders had no role in the design of the study; in the collection, analyses, or interpretation of data; in the writing of the manuscript, or in the decision to publish the results.

References

1. Lu, C.H.; Guo, W.; Hu, Y.; Qi, X.J.; Willner, I. Multitriggered Shape-Memory Acrylamide-DNA Hydrogels. *J. Am. Chem. Soc.* **2015**, *137*, 15723–15731.
2. Fern, J.; Schulman, R. Modular DNA strand-displacement controllers for directing material expansion. *Nat. Commun.* **2018**, *9*, 1–8.
3. Sicilia, G.; Grainger-Boultby, C.; Francini, N.; Magnusson, J.P.; Saeed, A.O.; Fernández-Trillo, F.; Spain, S.G.; Alexander, C.; Fernandez-Trillo, F.; Spain, S.G.; et al. Programmable polymer-DNA hydrogels with dual input and multiscale responses. *Biomater. Sci.* **2014**, *2*, 203–211.
4. Ma, Y.; Mao, Y.; An, Y.; Tian, T.; Zhang, H.; Yan, J.; Zhu, Z.; Yang, C.J. Target-responsive DNA hydrogel for non-enzymatic and visual detection of glucose. *Analyst* **2018**, *143*, 1679–1684.
5. Wang, X.; Wang, X. Aptamer-functionalized hydrogel diffraction gratings for the human thrombin detection. *Chem. Commun.* **2013**, *49*, 5957–5959.
6. Yang, H.; Liu, H.; Kang, H.; Tan, W. Engineering Target-Responsive Hydrogels Based on Aptamer--

Target Interactions. *J. Am. Chem. Soc.* **2008**, *130*, 6320–6321.

7. Cai, W.; Xie, S.; Zhang, J.; Tang, D.; Tang, Y. An electrochemical impedance biosensor for Hg2+ detection based on DNA hydrogel by coupling with DNAzyme-assisted target recycling and hybridization chain reaction. *Biosens. Bioelectron.* **2017**, *98*, 466–472.
8. Joseph, K.A.; Dave, N.; Liu, J. Electrostatically Directed Visual Fluorescence Response of DNA-Functionalized Monolithic Hydrogels for Highly Sensitive Hg2+ Detection. *ACS Appl. Mater. Interfaces* **2011**, *3*, 733–739.
9. Dave, N.; Chan, M.Y.; Huang, P.-J.J.; Smith, B.D.; Liu, J. Regenerable DNA-Functionalized Hydrogels for Ultrasensitive, Instrument-Free Mercury(II) Detection and Removal in Water. *J. Am. Chem. Soc.* **2010**, *132*, 12668–12673.
10. Ye, B.-F.; Zhao, Y.-J.; Cheng, Y.; Li, T.-T.; Xie, Z.-Y.; Zhao, X.-W.; Gu, Z.-Z. Colorimetric photonic hydrogel aptasensor for the screening of heavy metal ions. *Nanoscale* **2012**, *4*, 5998–6003.
11. Bai, W.; Spivak, D.A. A Double-Imprinted Diffraction-Grating Sensor Based on a Virus-Responsive Super-Aptamer Hydrogel Derived from an Impure Extract. *Angew. Chemie Int. Ed.* **2014**, *53*, 2095–2098.
12. Song, P.; Ye, D.; Zuo, X.; Li, J.; Wang, J.; Liu, H.; Hwang, M.T.; Chao, J.; Su, S.; Wang, L.L.; et al. DNA Hydrogel with Aptamer-Toehold-Based Recognition, Cloaking, and Decloaking of Circulating Tumor Cells for Live Cell Analysis. *Nano Lett.* **2017**, *17*, 5193–5198.
13. Li, S.H.; Chen, N.A.C.; Gaddes, E.R.; Zhang, X.L.; Dong, C.; Wang, Y. A Drosera-bioinspired hydrogel for catching and killing cancer cells. *Sci. Rep.* **2015**, *5*, 1–12.
14. Wei, X.; Tian, T.; Jia, S.; Zhu, Z.; Ma, Y.; Sun, J.; Lin, Z.; Yang, C.J. Target-responsive DNA hydrogel mediated stop-flow microfluidic paper-based analytic device for rapid, portable and visual detection of multiple targets. *Anal. Chem.* **2015**, *87*, 4275–4282.
15. Liu, S.; Su, W.; Li, Y.; Zhang, L.; Ding, X. Manufacturing of an electrochemical biosensing platform based on hybrid DNA hydrogel: Taking lung cancer-specific miR-21 as an example. *Biosens. Bioelectron.* **2018**, *103*, 1–5.
16. Chen, W.H.; Liao, W.C.; Sohn, Y.S.; Fadeev, M.; Cecconello, A.; Nechushtai, R.; Willner, I. Stimuli-Responsive Nucleic Acid-Based Polyacrylamide Hydrogel-Coated Metal–Organic Framework Nanoparticles for Controlled Drug Release. *Adv. Funct. Mater.* **2018**, *28*, 1705137.1-1705137.9.
17. Lai, J.; Li, S.; Shi, X.; Coyne, J.; Zhao, N.; Dong, F.; Mao, Y.; Wang, Y. Displacement and hybridization reactions in aptamer-functionalized hydrogels for biomimetic protein release and signal transduction. *Chem. Sci.* **2017**, *8*, 7306–7311.
18. Wang, Z.; Xia, J.; Cai, F.; Zhang, F.; Yang, M.; Bi, S.; Gui, R.; Li, Y.; Xia, Y. Aptamer-functionalized hydrogel as effective anti-cancer drugs delivery agents. *Colloids Surfaces B Biointerfaces* **2015**, *134*, 40–46.
19. Fern, J.; Scalise, D.; Cangialosi, A.; Howie, D.; Potters, L.; Schulman, R. DNA Strand-Displacement Timer Circuits. *ACS Synth. Biol.* **2017**, *6*, 190–193.
20. Liu, X.; Lu, C.-H.H.; Willner, I. Switchable Reconfiguration of Nucleic Acid Nanostructures by Stimuli-Responsive DNA Machines. *Acc. Chem. Res.* **2014**, *47*, 1673–1680.
21. Yin, B.-C.; Ye, B.-C.; Wang, H.; Zhu, Z.; Tan, W. Colorimetric logic gates based on aptamer-crosslinked hydrogels. *Chem. Commun.* **2012**, *48*, 1248–1250.
22. Nagahara, S.; Matsuda, T. Hydrogel formation via hybridization of oligonucleotides derivatized in water-soluble vinyl polymers. *Polym. Gels Networks* **1996**, *4*, 111–127.
23. Tierney, S.; Stokke, B.T. Development of an Oligonucleotide Functionalized Hydrogel Integrated on a High Resolution Interferometric Readout Platform as a Label-Free Macromolecule Sensing Device.

Biomacromolecules **2009**, *10*, 1619–1626.

24. Gao, M.; Gawel, K.; Stokke, B.T. Toehold of dsDNA exchange affects the hydrogel swelling kinetics of a polymer-dsDNA hybrid hydrogel. *Soft Matter* **2011**, *7*, 1741–1746.
25. Zhang, D.Y.; Winfree, E. Control of DNA Strand Displacement Kinetics Using Toehold Exchange. *J. Am. Chem. Soc.* **2009**, *131*, 17303–17314.
26. Langford, G.J.; Raeburn, J.; Ferrier, D.C.; Hands, P.J.W.; Shaver, M.P. Morpholino Oligonucleotide Cross-Linked Hydrogels as Portable Optical Oligonucleotide Biosensors. *ACS Sensors* **2019**, *4*, 185–191.
27. Kang, H.; Chou, P.-J.; Johnson, W.C.; Weller, D.; Huang, S.-B.; Summerton, J.E. Stacking interactions of ApA analogues with modified backbones. *Biopolymers* **1992**, *32*, 1351–1363.
28. Summerton, J.; Weller, D. Morpholino antisense oligomers: Design, preparation, and properties. *Antisense Nucleic Acid Drug Dev.* **1997**, *7*, 187–195.
29. Gehrke, S.H.; Fisher, J.P.; Palasis, M.; Lund, M.E. Factors Determining Hydrogel Permeability. *Ann. N. Y. Acad. Sci.* **2006**, *831*, 179–184.
30. Ogston, A.G. The spaces in a uniform random suspension of fibres. *Trans. Faraday Soc.* **1958**, *54*, 1754–1757.
31. Tierney, S.; Hjelme, D.R.; Stokke, B.T.B.T. Determination of Swelling of Responsive Gels with Nanometer Resolution. Fiber-Optic Based Platform for Hydrogels as Signal Transducers. *Anal. Chem.* **2008**, *80*, 5086–5093.
32. Jonášová, E.P.; Bjørkøy, A.; Stokke, B.T. Recovering fluorophore concentration profiles from confocal images near lateral refractive index step changes. *J. Biomed. Opt.* **2016**, *21*, 126014.
33. Ford Versypt, A.N.; Arendt, P.D.; Pack, D.W.; Braatz, R.D. Derivation of an analytical solution to a reaction-diffusion model for autocatalytic degradation and erosion in polymer microspheres. *PLoS One* **2015**, *10*, e0135506.1-e0135506.14.
34. Crank, J. The Mathematics of Diffusion. In *Clarendon Press*; Oxford University Press: Oxford, 1975; pp. 148–149 ISBN 0198533446.
35. Sim, A.Y.L.; Lipfert, J.; Herschlag, D.; Doniach, S. Salt dependence of the radius of gyration and flexibility of single-stranded DNA in solution probed by small-angle x-ray scattering. *Phys. Rev. E* **2012**, *86*, 021901.1-021901.5.
36. Williams Jr, J.C.; Mark, L.A.; Eichholtz, S.; Williams, J.C.; Mark, L.A.; Eichholtz, S. Partition and Permeation of Dextran in Polyacrylamide Gel. *Biophys. J.* **1998**, *75*, 493–502.
37. Wang, M.; Wu, B.; Tucker, J.D.; Lu, P.; Lu, Q. Cationic polyelectrolyte-mediated delivery of antisense morpholino oligonucleotides for exon-skipping in vitro and in mdx mice. *Int. J. Nanomedicine* **2015**, *10*, 5635–5646.
38. Wang, M.; Wu, B.; Shah, S.N.; Lu, P.; Lu, Q. Saponins as Natural Adjuvant for Antisense Morpholino Oligonucleotides Delivery In Vitro and in mdx Mice. *Mol. Ther. - Nucleic Acids* **2018**, *11*, 192–202.
39. Stellwagen, E.; Lu, Y.; Stellwagen, N.C. Unified Description of Electrophoresis and Diffusion for DNA and Other Polyions. *Biochemistry* **2003**, *42*, 11745–11750.
40. Park, I.H.; Johnson, C.S.J.; Gabriel, D.A. Probe Diffusion in Polyacrylamide Gels As Observed by Means of Holographic Relaxation Methods: Search for a Universal Equation. *Macromolecules* **1990**, *21*, 1548–1553.
41. Gajraj, A.; Ofoli, R.Y. Effect of extrinsic fluorescent labels on diffusion and adsorption kinetics of proteins at the liquid-liquid interface. *Langmuir* **2000**, *16*, 8085–8094.

519